Investigation and Correction for the Partial Volume Spill in Effects in Positron Emission Tomography

Mercy Iyabode Akerele

University of Leeds

Biomedical Imaging Science Department

Submitted in accordance with the requirements for the degree of
Doctor of Philosophy

November 15, 2019

Intellectual Property and Publications

The candidate confirms that the work submitted is her own, except where work which has formed part of jointly authored publications has been included. The contribution of the candidate and the other authors to this work has been explicitly indicated in the next page. The candidate confirms that appropriate credit has been given within the thesis where reference has been made to the work of others.

Dedication

This PhD is dedicated to God Almighty: the giver of life, my helper and the lifter of my head; and also to my late dad, Mr Obafemi Alfred Oloniyo. You earnestly looked forward to me having a PhD, but you died even before I started the PhD journey. Continue to rest in peace!

Acknowledgements

I am grateful to Schlumberger Foundation Faculty for the Future for sponsoring my PhD programme. Without you, this dream might not be actualised. I wish to express my profound gratitude to my supervisors, Drs Charalampos Tsoumpas and Steven Sourbron, for their support, intellectual mentoring, constructive criticism and encouragement throughout the entire duration of my PhD. Sincerely, it has been a moment of career grooming for me, and I can boldly say that I am better off for it. Thank you!

Many thanks to my tutors: Prof David Buckley and Dr Neil Turner. I indeed appreciate you. I also wish to thank Drs Marc R. Dweck and Rachael O. Forsythe; and their team at the University of Edinburgh, UK for supporting my PhD work and providing the patient datasets used for my research. Thanks to Dr Nicolas Karakatsanis for the time spent in converting the patient datasets into sinograms for reconstruction, and also for his suggestions and constructive feedbacks.

I appreciate everyone that has crossed my part at the University of Leeds and in particular the Leeds Institute of Cardiovascular and Metabolic Medicine (LICAMM) for providing an enabling environment for me to do my research, learn and develop. Thanks to my group members and colleagues, Dr Daniel Deidda, Palak Wadhwa, Richa Gandhi, Lisa Duff, Harry Tunniclife, Susmita Basak, Kanishka Sharma, Sirisha Tadimalla, Nikolaos Kallistis for being the best group I could ever ask for. Many thanks to my christian family at the Deeper Life Bible Church, Shannon Street, Leeds for your all-round support. Thanks to my pastors: Prof Kayode Adedayo, Dr Victor Ebenuwa, and Dr Richard Ajah, Mr Celestine Aigbologa and Mr Ibukun Agbaje for always asking after my well-being and praying for me. Thanks to my friends Dupe Ajayi, Janet Oluwi, Israel and Opeyemi Adekolurejo, Chiedza Ikpe, Queen Owoeye, and all their family members. A special thanks to the Dosunmu and Adegbite's family. You are simply amazing!

Finally, I want to thank my family, Mrs Alice Oloniyo (Mum), Jumoke Fayomi, Oluwaseun Iraoya and Bukola Olorunsola (my siblings), for supporting me in everything I do, there are no words to express how lucky I am to have you. Thanks to Olumide, Oyeyemi, Oyenike, Demilade, Ifeoluwa, Taiwo and Kehinde, Emmanuel, and all my family and friends for being there for me. My deepest

appreciation goes to my king, Oluwasegun Akerele, and my cute prince, Trophy Akerele; thanks for supporting me in this adventure, for believing in me and for your unconditional love and sacrifice. My PhD journey could have been overwhelming and frustrating without having you all around me.

Abstract

Positron emission tomography (PET) imaging has a wide applicability in oncology, cardiology and neurology. However, a major drawback when imaging very active regions such as the bladder and the bone is the spill in effect, leading to inaccurate quantification and obscured visualisation of nearby lesions. Therefore, this thesis aims at investigating and correcting for the spill in effect from high activity regions to the surroundings, as a function of activity in the hot region, lesion size and location, system resolution as well as application of post-filtering, using the background correction technique. This thesis involved analytical simulations for the digital XCAT2 phantom, and validation acquiring data from NEMA phantoms and patient datasets with the GE Signa PET/MR and Siemens Biograph mMR/mCT scanners. Reconstructions were done using the ordered subset expectation maximisation (OSEM) algorithm. Dedicated point spread function (OSEM+PSF) and the background correction (OSEM+PSF+BC) were incorporated into the reconstruction for spill in correction. For region of interest (ROI) analysis, a semi-automated ellipsoidal ROIs were drawn on the exact location of the lesions, and these were used to extract the standardized uptake value (SUV). The bias, recovery coefficient (RC), coefficient of variation (CoV) and contrast-to-noise ratio (CNR) were computed from the SUVs, and these were used as figures of merit to compare the performances of all the reconstruction algorithms. The thesis revealed that: (i) lesions within 15-20 mm from the hot region are predominantly affected by the spill in effect, leading to an increased bias and impaired lesion visualisation within the region; (ii) the spill in effect is further influenced by the ROI selection, increasing activity in the hot region, reduced resolution and application of post-filter; (iii) the spill in effect is more evident for the SUV_{max} than the SUV_{mean}; (iv) for proximal lesions (within 2 voxels around the hot region), PSF has no major improvement over OSEM because of the spill in effect, coupled with the Gibbs effect; (v) with OSEM+PSF+BC, the

spill in contribution from the hot region was removed in all cases (irrespective of ROI-selection, proximity of lesion to hot source, or application of post-filter), thereby facilitating stability in quantification and enhancing the contrast in lesions with low uptake. This thesis therefore concludes that the BC technique is effective in correcting for the spill in effect from hot regions to surrounding regions of interest. It is also robust to ROI-induced errors and post-filtering.

Contents

List of Figures

List of Tables

Acronyms

[^{18}F]-NaF	[^{18}F] Sodium Fluoride. xii, xix, xxi, xxiv, 2, 100, 103, 107, 108, 119, 124, 133, 134, 136–140, 145, 146, 149, 157
2D	two-dimensional. xv, xvi, xxiv, 30, 33, 69
3D	three-dimensional. xxiv, 39, 40, 67, 70–72
AAA	abdominal aortic aneurysm. xix, xxiv, 2, 100, 103, 107, 108, 124, 130, 134, 145, 147, 149
AC	Attenuation correction. xxiv, 38, 46, 47
ACF	attenuation correction factors. xxiv, 46, 67, 70, 103, 106
APDs	avalanche photodiodes. xxiv, 44
BC	background correction. xxiv, 2, 48, 53, 61, 97, 99, 100, 156, 157
CNR	contrast-to-noise ratio. vii, xvi, xxiv, 66, 70, 105
CoV	coefficient of variation. vii, xxiv, 110, 120, 127
CT	computed tomography. xvi, xxiv, 4, 13, 14, 16, 39, 43, 51, 74, 96, 101
CTAC	CT attenuation correction. xix, xxiv, 39, 108, 134
E step	Expectation step. xxiv, 34–36, 52

EM	expectation maximisation. xxiv, 58
FDG	fluorodeoxyglucose. xxiv, 2, 63, 66, 70, 103, 106, 146
FoV	field of view. xxiv, 40, 50, 65, 106
FWHM	full width at half maximum. xxiv, 28, 41, 42, 49, 67, 72, 103, 106, 108, 111, 135
GE	General Electric. xxiv, 71, 72, 155
GTM	geometric transfer matrix. xxiv, 48
HKEM	hybrid kernelised expectation maximisation. xxiv, 57, 58, 102
LOR	line of response. xxiv, 28, 29, 39
LP	local projection. xxiv, 48, 55, 102
M step	Maximisation step. xxiv, 35
MLE	maximum likelihood estimate. xxiv, 33
MLEM	Maximum likelihood expectation maximisation. xxiv, 33, 34, 36, 52
MR	magnetic resonance. xvi, xxiv, 4, 19, 70, 74, 96, 101, 106
MRAC	magnetic resonance attenuation correction. xviii, xix, xxiv, 70, 73, 84, 86, 102, 106, 107
MRI	magnetic resonance imaging. xxiv, 13, 14, 19, 20, 43, 51
NMR	nuclear magnetic resonance. xxiv, 19
OSEM	ordered subsets expectation maximisation. xxiv, 36, 49, 71–73, 103, 106, 108, 135

PET	positron emission tomography. xix, xxiv, 1, 2, 4, 13–15, 26, 28, 31, 33, 37–41, 43, 48–51, 58, 62, 70, 96, 100, 102, 103, 106–108, 118, 119, 149
PMTs	photomultiplier tubes. xxiv, 44
PSF	point spread function. xxiv, 48–51, 67, 72, 73, 106, 108, 135, 155, 156
PSMA	prostate specific membrane antigen. xxiv, 96
PVC	Partial volume correction. xxiv, 48, 49, 61
PVE	Partial volume effect. xxiv, 42, 48, 51, 99, 106
RC	recovery coefficient. vii, xxiv, 50, 105
ROI	region of interest. vii, xxiv, 37, 48, 55, 68, 70, 99, 102, 104, 105, 107, 108, 135
SiPMs	silicon photomultipliers. xxiv, 44
SNR	signal to noise ratio. xxiv, 29
SPECT	single photon emission computed tomography. xxiv, 14, 15, 26
SSS	single scatter simulation. xxiv, 40, 67, 103, 106
STIR	software for tomographic image reconstruction. xxiv, 39, 40, 42, 67, 70, 71, 103, 104, 106, 135, 155
SUV	standardized uptake value. vii, xxiv, 2, 26, 37, 62–64, 66–68, 74, 75, 135
TOF	time of flight. xxiv, 68, 155
VIBE	volumetric interpolated breath-hold examination. xxiv, 26, 106
VOI	volume of interest. xxiv, 55, 56, 102

Chapter 1

Introduction

1.1 Context and Motivation

Despite the wide applicability of positron emission tomography (PET) in oncology, cardiology and neurology (Capirci et al. [2007], Hoh [2007], Ben-Haim and Ell [2009]) for quantification, diagnosis, and post-therapeutic response prediction (Nahmias and Wahl [2008]), accurate clinical assessment is often affected by the partial volume effect (PVE) leading to overestimation (spill in) or underestimation (spill out) of activity in various small regions (Liu [2012], Gaertner et al. [2013], Afshar-Oromieh et al. [2014]). The spill in effect, in particular, can be very challenging when the target region is close to a hot background region such as the brain (Soret et al. [2007]), urinary bladder (Liu [2012]), myocardium (Du et al. [2013]) and spine (Forsythe et al. [2018]). Concerns have been raised on the effectiveness of some common tracers in imaging areas with high radiotracer uptake (hot regions), and these concerns stem from the observation that activity from the hot regions may interfere with PET quantification and visualisation of

nearby lesions, tumours and abnormalities. As a result, nearby lesions have their standardized uptake value (SUV) overestimated, and in some cases, lesions can be totally missed (Liu [2012]). Various techniques are being employed to correct for the spill in effect but none has been shown as an effective correction technique when the tumour of interest is within $10 - 50\ mm$ distance from the hot region (Liu [2012], Akerele et al. [2018]). In fact, past studies have shown that in such situations, the SUV is often substantially overestimated and therefore invalid (Liu [2012]). This effect can therefore pose great limitations to PET imaging in certain clinical investigations such as [^{18}F]- fluorodeoxyglucose (FDG) PET examination of the pelvic areas for infection, metastases and cancer (Bouchelouche and Oehr [2008], Heuber et al. [2017]); and [^{18}F] Sodium Fluoride ([^{18}F]-NaF) PET imaging of the abdominal aortic aneurysm (AAA) where extensive spill in effect from the bone into the aneurysm can be observed (Forsythe et al. [2018]). Common image analysis techniques to mitigate the spill in contamination include masking out the highly radioactive region in the image space, or simply excluding areas of spill in from regions of interest around the tissue of interest (Forsythe et al. [2018]). The challenge in this practice is the high dependence of the measurements on clinician expertise. In addition, a certain degree of potentially important physiological information might be lost from the excluded regions. This therefore suggests a clear need for more practical methods to correct for the spill in effects. This thesis focuses on investigating the spill in effect in lesions close to a hot background region, and also validating the background correction (BC) method (proposed by Silva-Rodriguez et al. [2016]) in mitigating this effect.

1.2 Purpose of the Thesis

The main goal of this thesis is to investigate spill in effects in regions close to a highly radioactive region, and to correct this using the background correction technique. This is an iterative reconstruction technique where the contribution from the active background region is estimated (through prior segmentation), forward projected and then included as part of the additive term in the reconstruction algorithm. This thesis presents the validation of the background correction technique with simulated and real data including phantoms and patients. It also shows the performance comparison of the background correction technique with other recent techniques in terms of their convergence, contrast, and noise properties, as well as their spill in correction capabilities.

1.3 Key Contributions of the Thesis

The specific achievements of this thesis are listed as follows:

1) The spill in effect from hot regions to surrounding colder regions of interest was thoroughly investigated. The contributing factors to the spill in effect were also investigated and discussed.

2) The performance of the background correction technique in mitigating quantification errors arising from the spill in effect was examined and validated with simulated and real data. The potential limitations of the background correction technique were also explored and discussed.

3) The spill in correction ability of the background correction technique was

also compared with other algorithms. This comparison was done on the basis of the convergence, contrast and noise properties of the algorithms.

4) The background correction technique was applied to several sets of clinical data which showed that spill in correction is feasible, and that it enhances PET quantification, lesion contrast and better patient management.

1.4 Thesis Overview

The thesis is divided into six main chapters, which are interconnected through the theme of spill in effects, correction and quantification. The overview of the thesis is presented as follows:

Chapter 2: Background

This chapter introduces the basic concept of medical imaging and the imaging techniques which are applicable to this thesis. A detailed description of the physical processes involved in PET acquisition, computed tomography (CT) and magnetic resonance (MR), and introduction to multi-modal imaging techniques is provided. The theoretical background and mathematical formulation of the algorithms and correction techniques used in this thesis is also provided.

Chapter 3: Validation of the Background Correction Method for the Suppression of Spill in Effects Near Highly Radioactive Regions in PET

This chapter investigates the effect of the spill in contamination on quantification of regions in proximity of a hot region. It also explores the factors which contribute to the spill in effect. Finally, the feasibility of the background correction technique described in Chapter 2 in correcting for the spill in effect is investigated and validated using simulated and real datasets. This chapter consists of work previously published in *IEEE Conference Proceedings* and *European Journal of Nuclear Medicine and Molecular Imaging Physics*. These are referenced in Akerele et al. [2017, 2018].

Chapter 4: Comparison of Correction Techniques for Spill in Effects

The systematic evaluation of the background correction technique in comparison with two novel correction techniques is performed in this chapter. This is done using both simulated and experimental PET/MR phantom data as well as abdominal aortic aneurysm PET/CT human patient data. The performance is compared using the convergence, contrast and noise properties of the techniques. Part of the work in this Chapter has been presented as oral presentation at the *2018 IEEE NSS MIC conference* and as a poster presentation at the *2019 EMIM meeting*. The work has also been submitted to *IEEE TRPMS* in 2019, and this has been provisionally accepted pending major correction.

Chapter 5: Clinical Application of the Background Correction Technique

In this chapter, the background correction technique is applied to 65 sets of abdominal aortic aneurysm PET/CT human patient data. The intention is to investigate the spill in contamination emanating from the bone into the aneurysm, and its effect on quantification and patient management. The performance of the background technique in correcting for this effect is also explored. The work in this Chapter has been submitted to *Journal of Nuclear Cardiology* in 2019 and this has been accepted pending minor correction.

Chapter 6: General Conclusion and Future Work

The general summary of the thesis are discussed in this chapter, together with the current limitations and potential future applications.

1.5 Dissemination

Work from the following jointly authored publications, which is listed as Akerele et al. [2017, 2018] in the References, is included in this thesis:

1.5.1 Journal Articles

Mercy I. Akerele, Palak Wadhwa, Jesus Silva-Rodriguez, William Hallet and Charalampos Tsoumpas. Validation of a Novel Image Reconstruction Method for the Suppression of spill in Effect in Positron Emission Tomography. In *European Journal of Nuclear Medicine and Molecular Imaging Physics, 5:34.*

The candidate designed the study and validated the background correction method with digital simulations, as well as experimental and patient dataset. She also performed all the simulations, image reconstructions, image analysis and manuscript writing as well as many other aspects. The organisation of the manuscript and writing corrections were jointly performed with co-authors. The acquisition experiment was performed by the co-authors.

Mercy I. Akerele, Nicolas Karakatsanis, Rachael O. Forsythe, Marc R. Dweck, Maaz Syed, Robert G. Aykroyd, Steven Sourbron, David E. Newby and Charalampos Tsoumpas. Iterative Reconstruction Incorporating Background Correction Improves Quantification in [^{18}F]-NaF PET Imaging of patients with Abdominal Aortic Aneurysm. In *Journal of Nuclear Cardiology;* ***In press****, 2019.*

The candidate designed the study, performed all the image segmentation, image reconstructions, image analysis, statistical analysis and manuscript writing as well as many other aspects. The organisation of the manuscript as well as writing corrections were jointly performed with co-authors. The acquisition of the patient data, and conversion to sinograms were performed by the co-authors.

Mercy I. Akerele, Nicolas Karakatsanis, Daniel Deidda, Jacobo Cal-Gonzalez, Rachael O. Forsythe, Marc R. Dweck, Robert G. Aykroyd, Steven Sourbron, and Charalampos Tsoumpas. Comparison of Correction Techniques for the spill in Effect in Emission Tomography. In *IEEE Transactions on Radiation and Plasma Medical Sciences;* ***Provisionally accepted, pending major corrections, 2019****.*

The candidate designed the study, performed all the image reconstructions, image analysis and paper writing as well as many other aspects. The organisation of the manuscript as well as writing corrections were jointly performed with co-authors. The acquisition of experimental phantom and patient data were performed by the co-authors.

1.5.2 Conference Papers

Mercy I. Akerele, Palak Wadhwa, Jesus Silva-Rodriguez, William Hallet and Charalampos Tsoumpas. Comparison of partial volume correction techniques for lesions near high activity regions. In *Nuclear Science Symposium and Medical Imaging Conference Record*, pages 1–7. IEEE, 2017.

The candidate performed all image reconstructions, image analysis and paper writing as well as many other aspects. The organisation of the manuscript as well as writing corrections were jointly performed with co-authors. The acquisition experiment was performed by the co-authors.

Mercy I. Akerele, Nicolas Karakatsanis, Daniel Deidda, Jacobo Cal-Gonzalez, Rachael O. Forsythe, Marc R. Dweck, Robert G. Aykroyd, Steven Sourbron, and Charalampos Tsoumpas. Improved Correction Techniques for Partial Volume and spill in Effects' Compensation in PET. In *Nuclear Science Symposium and Medical Imaging Conference Record*. IEEE, pages 1–5. IEEE, 2017.

The candidate designed the study and performed all the simulations. She performed all image reconstructions, image analysis, paper writing as well as many other aspects. The organisation of the manuscript and writing corrections were jointly performed with co-authors.

1.5.3 Conference Abstracts

Mercy I. Oloniyo, Nikos Efthimiou, Palak Wadwha, Jesus Silva-Rodriguez, and Charalampos Tsoumpas. Impact and correction of bladder uptake on tumour quantification. In *Nuclear Science Symposium-Medical Imaging Conference*. IEEE, 2016, Strasbourg, France (Poster presentation).

Mercy I. Oloniyo, Nikos Efthimiou, Palak Wadwha, Jesus Silva-Rodriguez, and Charalampos Tsoumpas. Investigation and correction of partial volume effect in lesions near high activity regions. In *University of Leeds Science Day*. 2017, Leeds, UK (Oral presentation).

Mercy I. Akerele, Palak Wadhwa, Jesus Silva-Rodriguez, William Hallet and Charalampos Tsoumpas. Comparison of partial volume correction techniques for lesions near high activity regions. In *Nuclear Science Symposium-Medical Imaging Conference*. IEEE, 2017, Atlanta, GA, USA (Poster presentation).

Mercy I. Akerele, Nicolas Karakatsanis, Daniel Deidda, Jacobo Cal-Gonzalez, Rachael O. Forsythe, Marc R. Dweck, Robert G. Aykroyd, Steven Sourbron, and Charalampos Tsoumpas. Improved Correction Techniques for Partial Volume and spill in Effects' Compensation in PET. In *Nuclear Science Symposium and Medical Imaging Conference Record*. IEEE, 2018, Sydney, Australia (November 2018, Oral presentation).

Mercy I. Akerele, Nicolas Karakatsanis, Daniel Deidda, Jacobo Cal-Gonzalez, Rachael O. Forsythe, Marc R. Dweck, Robert G. Aykroyd, Steven Sourbron,

and Charalampos Tsoumpas. Spill in Effect in Positron Emission Tomography (PET) Imaging of Abdominal Aortic Aneurysm (AAA). In *14th European Molecular Imaging Meeting*. EMIM, 2019, Glasgow, UK (March 2019, Poster presentation).

Daniel Deidda, **Mercy I. Akerele**, Rachael O. Forsythe, Marc R. Dweck, Maaz Syed, David Newby, Robert G. Aykroyd, and Charalampos Tsoumpas. Performance Evaluation of the Kernelised Expectation Maximisation Algorithm on [18F]-NaF PET/CT Data of Patients with Abdominal Aortic Aneurysm. In *Synergistic Image Reconstruction Framework*. SIRF Symposium, 2019, Chester, UK (November 2019, Poster presentation).

1.6 Grants and Awards

- Schlumberger Faculty for the Future Scholarship
  - PhD Award ($170,000 for 4 years (2015-2019))
  - Conference Support ($3000 per year, for 4 years (2015-2019))
- 2018 NSS/MIC/RTSD Trainee Grant: Conference Award to attend and present at the 2018 NSS/MIC conference in Sydney, Australia ($650AUD)
- 2017 NSS/MIC/RTSD Trainee Grant: Conference Award to attend and present at the 2017 NSS/MIC conference in Atlanta GA, USA ($500)
- 2017 LICAMM Science Day Award: An award for the runner-up oral presentation (£20 gift voucher)

- 2016 NSS/MIC/RTSD Trainee Grant: Conference Award to attend and present at the 2016 NSS/MIC conference in Strasbourg, France ($500)

Chapter 2

Background

In this chapter, a brief overview of medical imaging is presented, followed by a concise description of CT, magnetic resonance imaging (MRI), PET and multimodal imaging. A detailed theory of the PET reconstruction algorithm, some PET effects and correction techniques are also discussed, particularly as it relates to this thesis.

2.1 Introduction to Medical Imaging

In ancient times, people's health are being managed with the use of various traditional herbal treatments (Shi et al. [2010]). However, this comes with a lot of complications resulting from overdosage (since there is no prescription), infections (due to poor drug preparation) which subsequently leads to death (Yuan et al. [2016]). Civilisation and modernisation come with the introduction of modern medicine which is far more effective and life-saving (Wang et al. [2016]).

Nevertheless, modern medicine has its limitations. One of these is that it often treats symptoms, whereas most illnesses have complicating symptoms making

it difficult to diagnose and treat the main disease. Also, some sicknesses are chronic, the symptoms show up so late and this may lead to death before proper treatment is given (Singh [2010], Pizzorno [2016]).

Advances in medicine comes with the introduction of some diagnostic tools such as X-ray imaging and X-ray CT, medical ultrasonography and MRI which allow earlier and more precise diagnosis of diseases, help in the localisation of tumour, suggest the most appropriate treatment protocols, and subsequently increase the chances for survival (Hawkes [2019]). Although these medical imaging modalities could provide excellent anatomical images, their limitation in providing biological information suggest the need for complementary imaging modality.

Nuclear medicine offers a promising future for imaging in that it is possible to obtain images of biochemical processes which give valuable information about any type of disease ([US], Mettler Jr and Guiberteau [2012]). It could also identify ailments earlier than some other imaging modalities. For example, Alzheimer disease as well as reduced blood supply to the heart can be diagnosed far before any symptoms ensues (Johnson et al. [2013]). Also, nuclear medicine offers an ample opportunity for whole-body imaging. This is particularly useful in cases where lesions spread all over the body (Cherry et al. [2018], Rahmim et al. [2018]).

There are two major imaging modalities in nuclear medicine which are: single photon emission computed tomography (SPECT) and PET. The former involves emission of a single photon, while for the latter, a positron is emitted which annihilates with an electron to form two annihilation photons. Imaging is done by injecting trace amounts of radioactive compounds, known as radiotracers, into the body. These compounds are majorly gamma or positron-emitters upon decay. The energy of the photons emitted are high enough so that a significant

amount can penetrate through the body and be detected by an external camera. The distributions of the emitted photons within the body are used to form images which provide diagnostic information for wide range of diseases and infections (Welch and Pimlott [2010]). Radiotracers used in nuclear medicine are either generated in a cyclotron or generator.

Nuclear medicine makes use of detectors which can detect trace amount of radioactivity, as well as radionuclides with high-specific activity. Therefore it is sufficient to form high quality images. This imaging technique uses different radiotracers as shown in Table 2.1, but the most widely used is ^{99m}Tc for SPECT and ^{18}F for PET.

Table 2.1: Some Common Radionuclides used in Nuclear Medicine

	Radionuclides	Symbol	Half-life ($T_{1/2}$)	Uses
SPECT	Technetium-99m	^{99m}Tc	6.01 hours	Brain, heart and kidney imaging
	Iodine-123	^{123}I	13.2 hours	Diagnosis of thyroid disorder
	Chromium-51	^{51}Cr	27.7 days	Survival studies of red blood cell
	Thallium-201	^{201}Tl	73 hours	Cardiac studies
	Gallium-67	^{67}Ga	3.26 days	Inflammation detection
PET	Carbon-11	^{11}C	20.3 mins	Protein synthesis and metabolism
	Nitrogen-13	^{13}N	9.97 mins	Blood flow marker in cardiac studies
	Oxygen-15	^{15}O	2.03 mins	Blood flow studies
	Gallium-68	^{68}Ga	67.7 mins	Cancer imaging
	Fluorine-18	^{18}F	110 mins	Glucose metabolism
	Rubidium-82	^{82}Rb	75 secs	Blood flow measurement
	Copper-64	^{64}Cu	12.7 hours	Small animal imaging

The opportunity for wide selection of radionuclide compounds combined with the high sensitivity obtained make nuclear medicine a thriving imaging technique. PET is however preferred to SPECT due to its characteristic high resolution and sensitivity (Rahmim and Zaidi [2008]).

2.2 Computed Tomography (CT)

In 1895, X-rays were discovered by Wilhelm Conrad Rontgen, a German physicist who later won a Physics Nobel Prize in 1901. In 1971, Godfrey Newbold Hounsfield (1979 Nobel Prize winner for Physiology and Medicine) implemented the first X-ray CT system. Since the discovery of X-rays, CT has been referred to as the most important invention in radiological diagnosis (Kalender [2006]). Although the initially implemented CT was limited to imaging of the brain, this has now developed into a versatile 3D whole body imaging modality for a wide range applications. CT can be used for screening, diagnosis, radiotherapy treatment planning and patient follow-up.

2.2.1 Basic Principles

CT acquisitions are made by measuring the X-ray transmission through an object for a large number of projections, hence the name computed tomography. As the X-rays pass through the object, they are either absorbed, scattered, or transmitted. The scattered and absorbed X-rays result in X-ray intensity reduction, and the process is called attenuation. The X-rays transmitted through the object at the different angles are collected on the detector, and visualised on computer, thereby creating a complete reconstructed image of the object. The 3D data structure of the image represents the electron density distribution in the object (Bartscher et al. [2007]).

A CT image consists of a matrix of pixels, and a value is assigned to each pixel which is proportional to the average linear attenuation coefficient, μ (m^{-1}) of the tissue present in that pixel. The linear attenuation coefficient is dependent

on the composition, density and photon energy of the material as given by Beer's law:

$$I(T) = I_o e^{-\mu T} \tag{2.1}$$

where $I(T)$ and I_o are the intensities of the attenuated and non-attenuated X-ray beams respectively; and T is the material thickness.

Since the human body is made up of different tissues with their associated linear attenuation coefficients, the intensity of an X-ray beam transmitted through a distance, d, in the patient body can be expressed as:

$$I(d) = I_o e^{-\int_0^d \mu(T) dT} \tag{2.2}$$

The matrix of the reconstructed linear attenuation coefficients, $\mu_{material}$, is transformed into a corresponding Hounsfield units, $HU_{material}$ where the HU scale is expressed relative to the linear attenuation coefficient of water at room temperature as:

$$HU_{material} = \frac{\mu_{material} - \mu_{water}}{\mu_{water}} \times 1000 \tag{2.3}$$

HU ranges from -1000 for air (as $\mu_{material}$=0) to +1000 for bone. In essence, HU depends on the material composition, the tube voltage, and the temperature. A minimum of 12 bit depths can be assigned to the HU, thereby enabling the creation of an Hounsfield scale from -1024 to +3071 which covers most clinically relevant tissues.

2.2.2 Image Acquisition and Reconstruction

CT is used in medical imaging to produce 3D representations of a patient by taking many X-ray projections around a rotation axis and then reconstructing a 3D model using many reconstruction algorithms. This reconstruction challenge was solved by Cormack [1963] and Hounsfield [1973], who later received a joint Nobel prize in 1979. Over the years, five generations of CT scanners have been developed, and the efficiency of data acquisition has increased with each generation. Currently, most scanners are helical, multi detector row CT scanners. A typical CT imaging system consists of the CT gantry, patient table and computer. The gantry contains the X-ray tube, detector, high voltage generator, air or water cooling, data acquisition system, collimator and the beam shaping filters, which are required to record the transmission data of the patient. The gantry is mounted on a rotating support so that the transmission data can be recorded at different rotating angles. The recorded projection data are then transmitted from the gantry to the computer for image reconstruction.

Several reconstruction algorithms have been developed to reconstruct the 3D acquired projections based on the principle of Radon transform, the statistical knowledge of the data acquisition process and the geometry of the imaging system (Herman [2009]). In general, we have the analytical (cone-beam and multi-slice helical) reconstructions and the iterative reconstruction. In the analytical reconstruction algorithms, each projection sample is weighted, filtered and back-projected to formulate an image. However in the iterative method, the image is estimated iteratively until an initially set cost function is minimised. This cost function measures how well the estimated image fits the acquired projection

data according to a model of the imaging system. Although the iterative method is complex and time consuming, they are routinely used in nuclear medicine because of their benefits over analytical methods. Iterative methods have better performance in low-dose CT acquisitions, and can remove streak artefacts in images, especially when fewer projection angles are used.

2.3 Magnetic Resonance Imaging (MRI)

MRI is a non-invasive and non-ionising medical imaging technique which is based upon the principle of nuclear magnetic resonance (NMR). Unlike other imaging modalities which use X-rays or radioactive isotopes, MRI does not use ionising radiation. It also has a good soft tissue contrast which gives it an edge over other modalities and it can be particularly used to diagnose problems with joints, cartilage, ligaments and tendons.

In the mid 1940s, Felix Bloch and Edward Purcell independently discovered the principle of MR from the excitation of protons immersed in a static magnetic by a radio frequency field at the resonance frequency (McRobbie et al. [2017]). Later in 1971, Raymond Damadian discovered that tumours and normal tissues excited at the same frequency have different relaxation times. These form the basis for MRI as a diagnostic and treatment monitoring tool.

2.3.1 MRI Theory

MRI operates on the principle of NMR which occurs when nuclei interact with a strong magnetic field. For this to happen, such nuclei must possess an intrinsic magnetic moment and spin angular momentum (i.e. they must possess a non-

zero spin) (Lipton [2008]). This property makes it possible for a nucleus placed in a magnetic field to be excited by radio waves, and consequently emit a detectable radio frequency signal. The hydrogen nucleus has this property, and since the human body is made up of approximately 70% water (containing the hydrogen nucleus), the MRI operates on hydrogen-based resonance. The hydrogen nucleus has a fixed spin (and charge) and the resultant magnetic moment points in a random direction in the absence of an external magnetic field, as illustrated in Figure 2.1. But in the presence of a uniform magnetic field B_o, the spins will precess around B_o in a trajectory manner describing a cone because of the spin angular momentum. This is described in Figure 2.2.

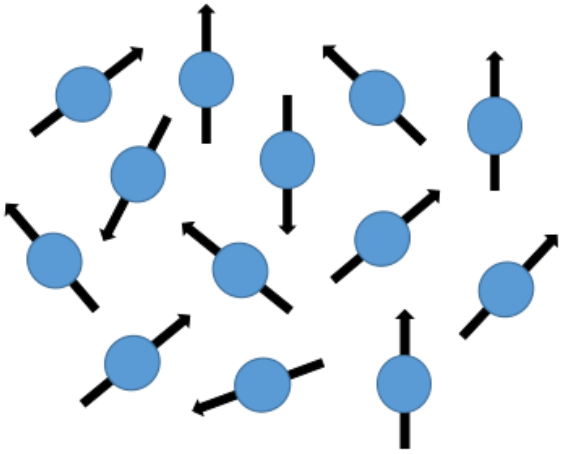

Figure 2.1: Randomly oriented hydrogen spins outside a magnetic field

The angular frequency, ω_o, of the precession is given by the Lamor's equation in Equation 2.4, and the precession is described by the Bloch equation in Equation 2.5:

$$\omega_o = \gamma \left| B_o \right| \tag{2.4}$$

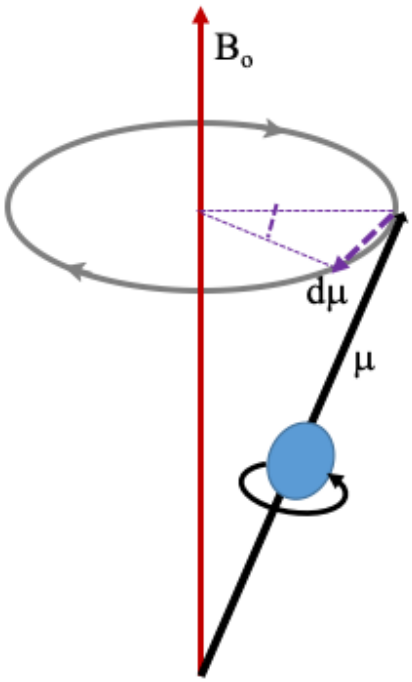

Figure 2.2: Schematic representation of precession of an isolated spin of magnetic moment μ in a static magnetic field B_o

$$\frac{d\mu}{dt} = \omega_o \times \mu \tag{2.5}$$

where γ is the gyromagnetic constant (42.58 MHz/T for hydrogen), $|B_o|$ is the magnetic field strength and μ is the magnetic moment.

The finite temperature of the human body leads to an anisotropic spin precession, which means the magnetic moments are likely to orientate with low magnetic energy parallel to B_o than high magnetic energy anti-parallel to B_o. This effect leads to a net magnetisation, M, and this is zero when no external field is applied (McRobbie et al. [2017]).

Without an RF pulse, the initial net magnetisation, M_o, is aligned with the magnetic field B_o. But when an RF pulse, B_1, is applied at the Larmor

frequency, it results in a resonance and the M_o tilts away from B_o. The M_o has two components: (1) the transverse component, M_{xy}, which rotates on the xy axis, and (2) the longitudinal component, M_z, along the z-axis. This is described in Figure 2.3. The rotation of M_{xy} about the z-axis generates an electromagnetic field which is capable of inducing a current though the receiver coil. The signal generated can be detected when amplified, and this is referred to as MR signal or free-induction decay.

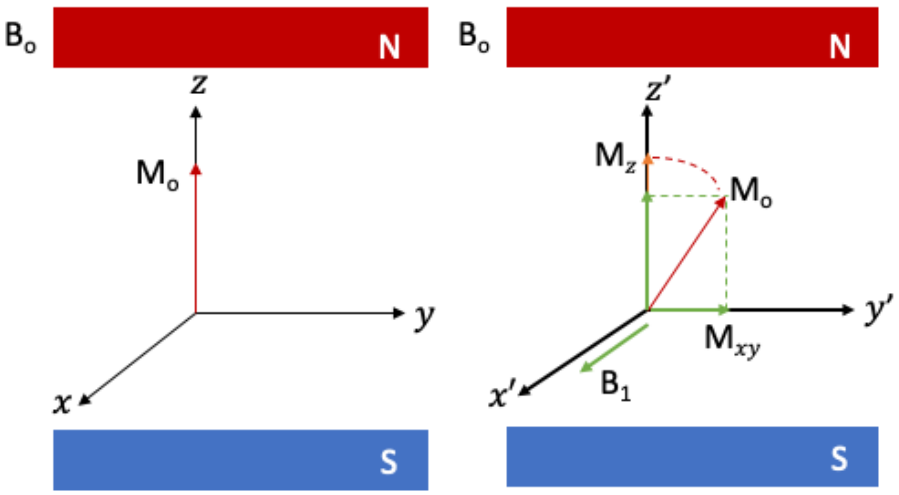

Figure 2.3: The net magnetisation in (a) the equilibrium state, and (b) when an RF pulse B_1 is applied. B_1 tips the spin towards the xy-plane, hence producing two magnetisation components M_z and M_{xy}

2.3.2 Relaxation Mechanism

When an RF pulse is applied, the spin system remains in their excited states, but when the RF pulse is stopped, there is loss of energy, and the spin returns to its equilibrium state. This process is referred to as relaxation, and the time it

takes is the relaxation time (T_1 and T_2). There are two mechanisms of relaxation, namely: spin-lattice and spin-spin relaxation. The spin-lattice relaxation is the longitudinal relaxation of the M_z component. This is characterised by the time constant T_1, which is the rate at which energy is transferred from the nuclear spin system to the neighbouring molecules, known as the lattice. The standard method of measuring T_1 is known as the inversion-recovery, and this is given by the Bloch equation (Bloch [1946]):

$$M_z = M_o \left(1 - e^{-t/T_1}\right) \tag{2.6}$$

The spin-spin relaxation is the transverse relaxation of the M_{xy} component. This is represented by the time constant T_2 and can be expressed as:

$$M_{xy} = M_o e^{-t/T_2} \tag{2.7}$$

After a 90^o pulse, the spins precess coherently in one direction, but this coherence is gradually lost due to field inhomogeneity and direct interaction between spins. However, this type of relaxation does not involve any transfer of energy to the lattice. The dephasing due to the combined impact of T_2 decay and field inhomogeneity is expressed as T_2^*, and it is shorter than T_2 (McRobbie et al. [2017]).

It is worth noting that there is a relation between the spin-spin and spin-lattice relaxation, because an increase in z-magnetization is not possible without a corresponding decrease in xy-magnetization. So, $T_2 \leq T_1$ ($T_2 \approx T_1$ in liquids, but $T_2 \ll T_1$ in solids).

2.3.3 Image Acquisition

During acquisition, the raw data is spatially organised to locate a signal in a matrix using a spatial encoding technique that is based on the magnetic field gradient. The first step is selecting a slice to be imaged. When the gradient is turned on, the magnetic field strength varies along a specific direction. The Lamor frequency will also change along this direction, hence, each slice can be excited by applying different RF pulses, and so resonance occurs. Depending on sequence, slice selection can be made using X, Y or Z gradients which correspond to sagittal, coronal and axial slices respectively (Weishaupt et al. [2008]). The slice thickness however depends on combination of two factors: (1) the strength or steepness of the gradient, and (2) the frequency range or bandwidth in the RF pulse (Sprawls [2000]). A shallow gradient generates a thicker slice while a steep gradient generates a thinner slice as demonstrated in Figure 2.4.

Having selected the position and the thickness of the slices, the spatial position of the MR signal is then identified using spatial encoding, comprising of phase and frequency encoding. In phase encoding, the gradient in one orthogonal direction (say, y) is switched on and this changes the frequencies of the spins with respect to their location along the gradient. As a result, the excited spins at a higher position experience a stronger magnetic energy and gain phase compared to spins at lower position. This results in a phase shift of the spins, and each slice can then be identified by its unique phase. For frequency encoding, the gradient is applied in the third direction (i.e. x) and this generates a magnetic field whose strength increases from right to left. The resulting change in frequencies causes the left side spins to precess slower than the right side spins. Having obtained

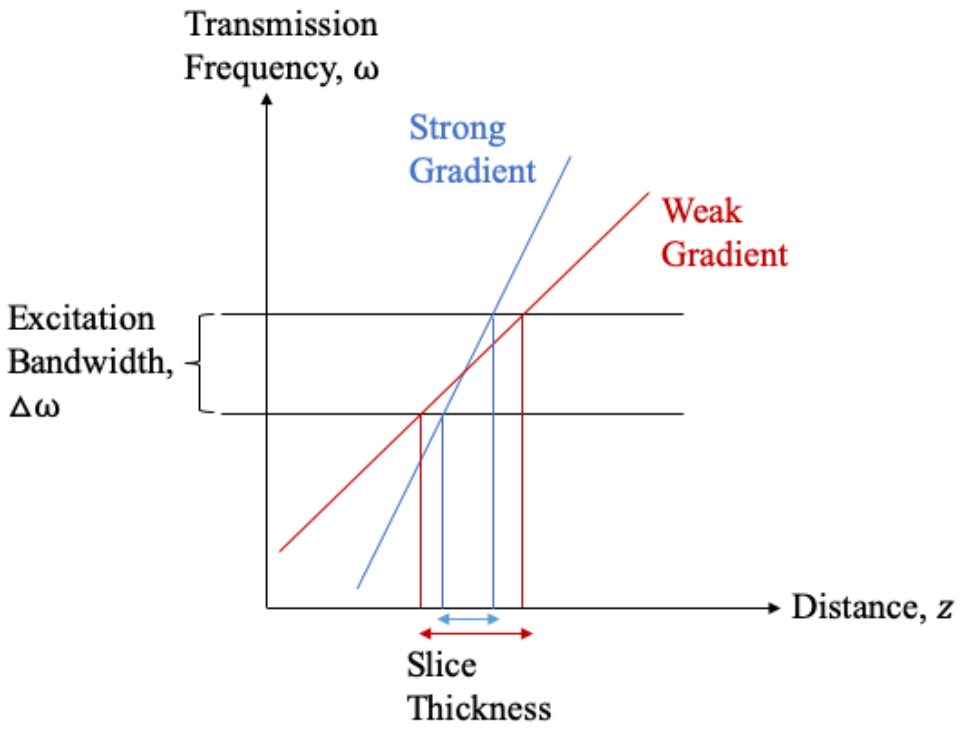

Figure 2.4: Demonstration of MR slice selection with corresponding slice thickness

a wide range of frequency spectrum, each slice can then be characterised by its specific frequency. Combination of both phase and frequency results helps to spatially identify each volume element (voxels) uniquely. The encoding process is repeated several times at different gradient strengths, and the information containing the MR signal is stored into K-space. The number of phase encoding steps determines the number of pixels in the image. More phase encoding steps improve resolution and image quality, but also prolongs the total scan time (Liney [2007], Weishaupt et al. [2008]). A Fourier transform is then applied to all the raw k-space values, which then generate the final MR image.

Although the application of MRI to image hard tissues is challenging due to the low water contents in such tissues, MRI techniques that are able to image

tissues with low water content and ultrashort T_2 are being developed. The most promising techniques include ultrashort echo time (UTE) imaging, zero echo time (ZTE) imaging, and sweep imaging with Fourier transformation (SWIFT). The ZTE imaging sequence is used for GE Signa PET/MR scanner attenuation estimation (Delso et al. [2018]). For this sequence, the encoding gradient is switched on before the RF pulse excitation, hence resulting in zero TE (Mastrogiacomo et al. [2019]). For Siemens mMR scanner, the attenuation image is obtained using volumetric interpolated breath-hold examination (VIBE) sequence with two segmented tissue classes: air and water (Karakatsanis et al. [2016]).

2.4 Positron Emission Tomography (PET)

PET is a non-invasive imaging technique with established applications in oncology, cardiology and neurology (Capirci et al. [2007], Hoh [2007], Ben-Haim and Ell [2009]) using SUV for quantification, diagnosis, and post-therapeutic response prediction (Nahmias and Wahl [2008], Suttie et al. [2009]). It visualises distribution of molecules in the body and provides functional and molecular information of tissues such as blood flow, receptor density and glucose metabolism. PET is preferred in clinical routine because it has a relatively higher sensitivity and quantitative accuracy than SPECT (Frey et al. [2012]).

2.4.1 Basic PET Principles

PET examination is carried out by injecting positron emitting radiotracers from photon-rich elements into the body. A radiotracer consists of a biologically active molecule which is radiolabelled with an unstable isotope. The most common

isotopes used in PET imaging are [^{11}C], [^{13}N], [^{15}O], [^{18}F] and [^{68}Ga]. These radioisotopes are bound to a molecule targeting specific functions in the body (as shown in Table 2.1). PET radiotracers have relatively short half-lives, and this implies that high count-rate image acquisitions with low patient-radiation dose can be achieved.

An injected radiotracer decays by emitting a positron and a neutrino. The positron travels a short distance (known as the mean positron range) and interacts with a free electron in the body as demonstrated in Figure 2.5. The positron range varies from isotope to isotope, and it is the main source of image blurring and resolution degradation in PET imaging.

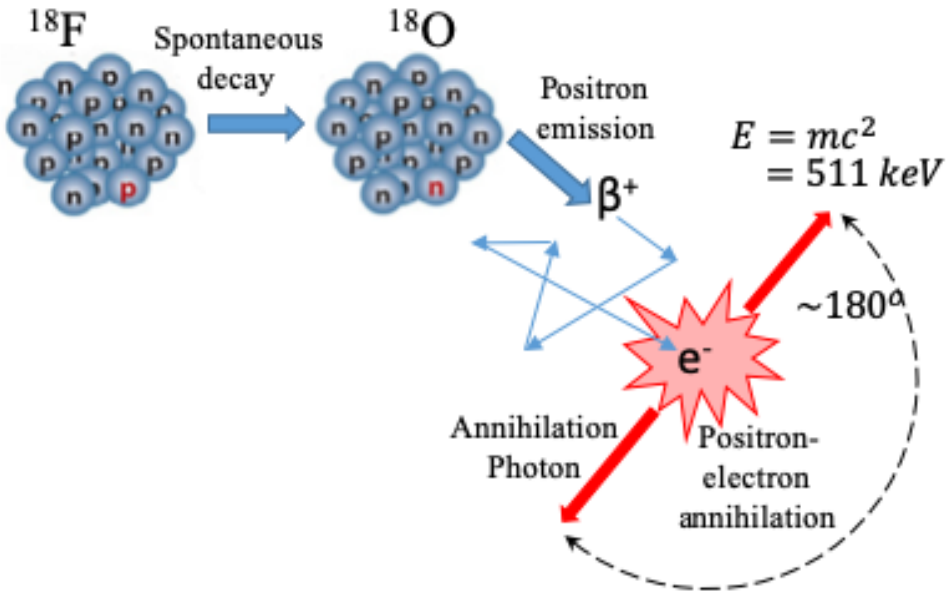

Figure 2.5: Illustration of photon formation and detection in PET imaging

Both positron and electron are annihilated, resulting in the production of two high energy photons. For conservation of mass and momentum, these two photons are required to travel in opposite direction with the same mass and

energy (511 keV) which determine the line of response (LOR). Ideally, the angle between the two photons should be 180^o, but in reality, the positron has non-zero kinetic energy and so, the photons are typically emitted with an angle of $180^o \pm 0.25^o$. This uncertainty in specifying the LOR (known as acolinearity) causes an additional image blurring and resolution degradation in PET that is proportional to the radius of the detector ring, R. The magnitude of this blurring (in mm FWHM) is given by 0.0044R. So, in essence, the same level of acolinearity leads to a bigger degradation with a larger ring diameter.

PET resolution is given by the full width at half maximum (FWHM) of the PET system, and this is affected by factors such as the detector size, positron range and acolinearity, as expressed in Equation 2.8:

$$FWHM_{total} = \sqrt{FWHM_{det}^2 + FWHM_{range}^2 + FWHM_{acol}^2} \tag{2.8}$$

where $FWHM_{det}$, $FWHM_{range}$ and $FWHM_{acol}$ are the blurring caused by the detector size, positron range and acolinearity respectively.

The contribution to resolution degradation due to positron range can be summarised in Table 2.2. The implication is that resolution degradation can be kept at minimum by using a radiotracer with relatively low positron range. For example, imaging with [^{68}Ga] will give lower resolution than using [^{18}F] tracer. Other factors such as the detectors effects and depth of interaction can also limit the resolution, but these can be compensated for in detector design.

The annihilated photons are detected by a pair of detectors in the detector ring in a process called coincidence detection. In order for the two photons to be recorded as a coincident event, they must reach the detector pair within a

Table 2.2: Contribution to resolution blurring due to positron range of common PET radiotracers (Derenzo et al. [1982], Jødal et al. [2012]).

Isotope	E_{max} (MeV)	R_{max} (mm)	FWHM (mm)
^{18}F	0.64	2.4	0.54
^{11}C	0.97	4.1	0.92
^{13}N	1.22	5.1	1.49
^{15}O	1.72	7.3	2.48
^{68}Ga	1.90	8.2	2.83

specific time and energy window. There are basically three types of coincidence detection, as shown in Figure 2.6. True coincidence is when the photons measured are related to the same annihilation event. Scatter coincidence occurs when one or both annihilated photons undergo Compton scattering, potentially leading to a wrongly recorded LOR. Random coincidence occurs when the two photons originating from different annihilation events are mistakenly recorded as a single annihilation event. Scatter and random events degrade image resolution by contributing a background signal, thereby decreasing the signal to noise ratio (SNR). The performance of an imaging system in terms of SNR is measured using the noise equivalent count rate (NECR):

$$NECR = \frac{True^2}{True + Random + Scatter} \tag{2.9}$$

The distance between the detector pair is the LOR along which the annihilation process takes place. The LOR is characterised by the angle and the shortest distance between the centre of the detector ring and the LOR. Figure 2.8 shows four coincident detections and their respective angles plotted as a function of distance from the centre. A graph of all possible LORs at different points in the image forms a sine wave, and therefore it is called "sinogram".

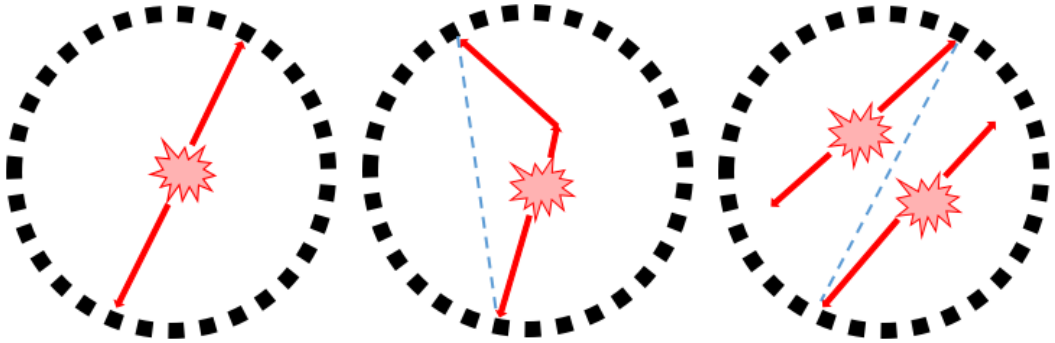

(a) (b) (c)

Figure 2.6: Illustration of (a) true, (b) scatter and (c) random coincident events. In true coincidence, the event detected by the detector pair actually took place along the LOR, but in scatter and random coincidences, the LORs are wrongly determined.

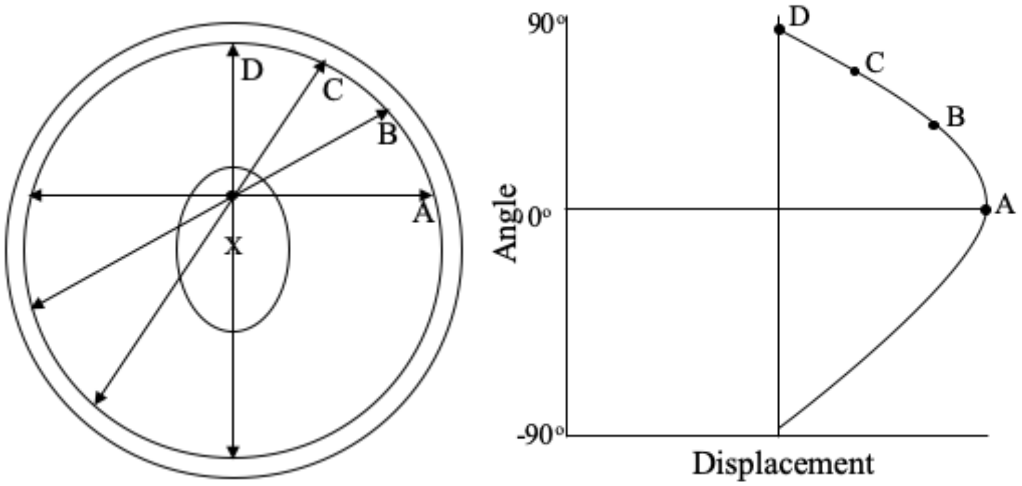

(a) (b)

Figure 2.7: An example of sinogram formation in 2D PET imaging. (a) shows an ellipsoidal ROI situated at the centre of the ring (marked X), with four LORs (A, B, C and D) passing through it; and (b) shows the plots of the LORs with the angular orientation on y-axis, and the displacement from the centre on x-axis (Adapted from Fahey [2002]).

A sinogram is a set of bins corresponding to 1 segment and 1 axial position. When there is no axial compression, the sinogram corresponds to the LORs in a detector ring (direct sinogram) or between two detector rings (oblique sinogram). Therefore, for a scanner having n detector rings, there are n direct sinograms and $n * n - n$ oblique sinograms. This results in a total of $n * n$ sinograms. Two rings associated to a sinogram is separated by a distance called the ring difference, while the segment is the set of sinograms having a common ring difference. However, axial compression is often used to reduce the number of sinograms at different ring difference. This is often referred to as the span, which shows how much axial compression has been used. A schematic representation of the axial compression is shown in Figure 2.8.

Several sinograms are collected, and these are back-projected into the image space using image reconstruction algorithms.

2.4.2 Image Reconstruction

After patients are injected with a radiotracer, PET scanners are able to collect the data of the *in vivo* radiotracer distribution as described in section 2.4.1. In order to obtain functional information of the images, these data need to be reconstructed using tomographic image reconstruction.

Reconstruction is an inverse problem in that it uses the information stored in form of a sinogram to obtain the radiotracer distribution.

If a forward problem is represented by:

$$y = Hf \tag{2.10}$$

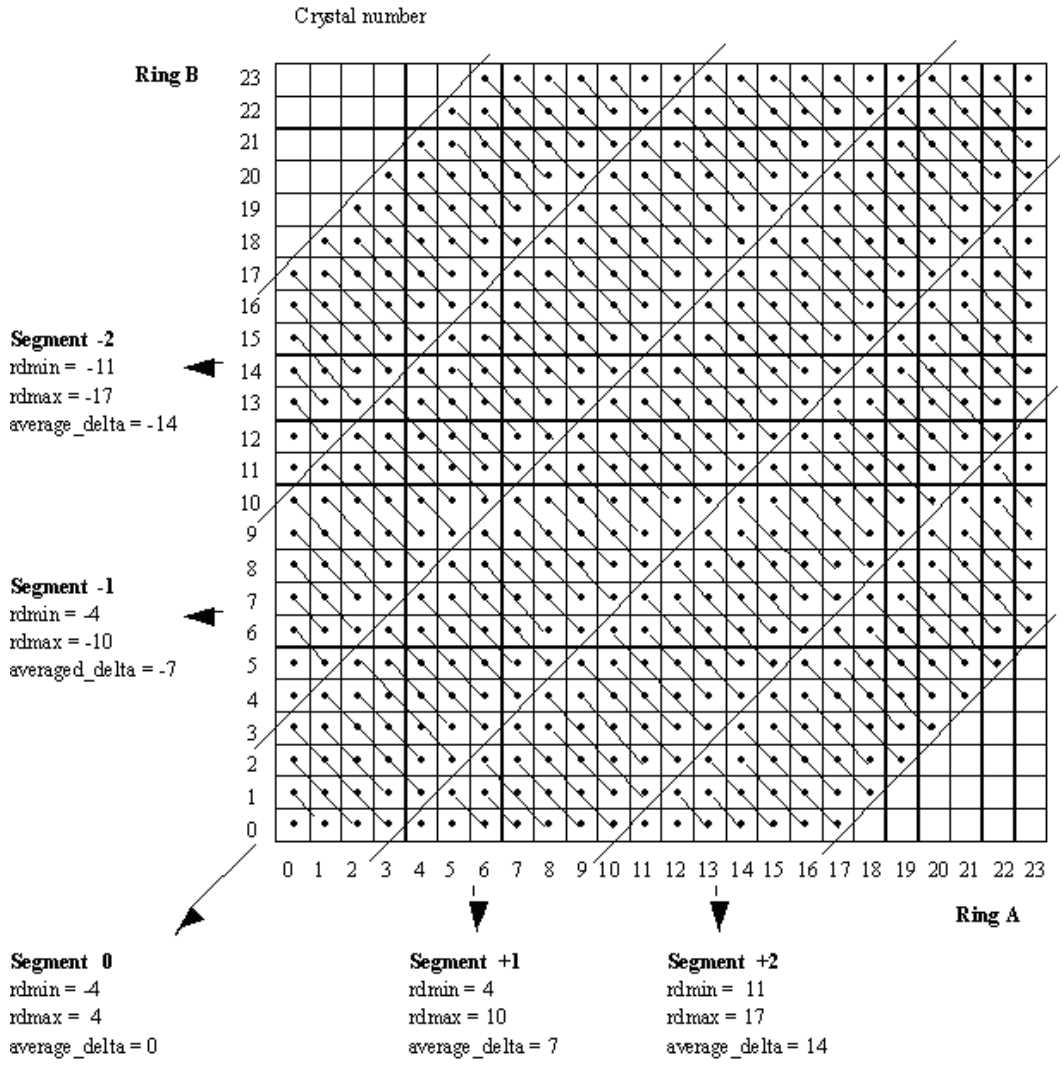

Figure 2.8: A Michelogram of data with a maximum ring difference of 17 and a span of 7. rdmin, rdmax and average_delta represent the minimum, maximum and averaged ring difference respectively (From STIR glossary (Labbe et al. [2012])).

where y is the measured sinogram, H is the projection matrix and f is the image to be obtained, f is obtained using the inverse method $f = H^{+}y$, where H^{+} is the pseudo-inverse of H. The solution to the inverse problem can be achieved through image reconstruction algorithms, which is capable of incorporating the

Poisson nature of the photon measurement, accounting for the noise and other relevant physical features (Lange and Carson [1984]). There are basically two image reconstruction methods, namely: analytical and iterative reconstruction methods.

Analytical reconstruction methods are commonly used in 2D reconstruction and the most common method is the filtered backprojection (FBP). This works by estimating the Fourier transforms of the projection data, and multiplying it with a frequency filter. The resulting inverse transform is then estimated and back-projected to form an image. The implementation introduces a lot of noise and star artefacts in the resultant image especially when limited number of projections are used (Lyra and Ploussi [2011]). Other factors such as scanner geometry and spatial variance make the use of analytical reconstruction techniques complicated.

Iterative reconstruction method involves the use of an iterative approach to reconstruct images. In most cases, it gives better and more accurate estimate than the analytical approach because it makes use of a detailed and more realistic system model (Nuyts et al. [2013]). However, this is done at the expense of increased complexity and computational time. Maximum likelihood expectation maximisation (MLEM), introduced in 1982 by Shepp and Vardi [1982], is an iterative reconstruction technique which forms the basis for most statistical reconstruction methods. It is commonly used in PET image reconstruction and it helps in the determination of maximum likelihood estimate (MLE) using numerical methods.

MLEM algorithm is employed to estimate the likelihood of the emission based on the assumption that measurement follows a Poisson distribution. Given the

mean value of the emission data as y_i and the expectation value as $\sum_j H_{ij} f_j$, The probability of measuring f given y ($p(f, y)$) is a difficult inverse problem, but this can approximated from the probability of measuring y given f ($p(y, f)$) which is a rather 'easy' forward problem. These two probabilities are linked by the Bayes' theorem:

$$p(f, y) \sim \frac{p(y, f)\ p(f)}{p(y)} \tag{2.11}$$

For maximum likelihood, we assume:

$$p(f, y) \sim p(y, f) = \prod_i \left[\frac{e^{-(H_{ij} \cdot f_j)} (H_{ij} . f_j)^{y_i}}{y_i!} \right] \tag{2.12}$$

There is need to choose the most likely image which maximises the probability of producing the data. This is best done by maximising the log-likelihood of the distribution. So,we take the logarithm of the density function, $P(y, f) = ln\,(p(y, f))$, also called the objective function:

$$P(y, f) = ln\,(p(y, f)) = \sum_{i \in N} \left[y_i ln \left(\sum_{j \in I_i} H_{ij} f_j \right) - \sum_{j \in I_i} H_{ij} f_j - \ln(y_i!) \right] \tag{2.13}$$

where I_i is the set of voxel contributing to projection i; N is the total number of projections in the data; H_{ij} is the probability that an event occurring in voxel j produces a coincidence in the i^{th} pair of detectors, taking into account the attenuation and normalisation corrections; f_j is the intensity of pixel j of the emission image; and y_i represents the emission sinogram data.

MLEM algorithm is usually generated using two steps:

- Expectation step (E step): This step estimates the expectation value of

$P(y, f)$, (i.e $E(P(y, f)|y, f^{(n)})$, using a uniform image $f^{(n)}$ for the initial iteration.

$$E(P(y,f)|y,f^{(n)}) = E\left[\sum_{i\in N}\left(y_i ln\left(\sum_{j\in I_i} H_{ij}f_j\right) - \sum_{j\in I_i} H_{ij}f_j - \ln(y_i!)\right)|y, f^{(n)}\right] \tag{2.14}$$

Due to linearity of expectation, Equation 2.14 can be rewritten as:

$$E(P(y,f)|y,f^{(n)}) = \sum_{i\in N}\left[E[y_i|y,f^{(n)}] ln\left(\sum_{j\in I_i} H_{ij}f_j\right) - \sum_{j\in I_i} H_{ij}f_j - \ln(y_i!|y, f^{(n)}]\right] \tag{2.15}$$

This yields Equation 2.16 by applying the probability theory

$$E(P(X,f) \mid Y, f^{(n)}) = \sum_{i,j}\left[\frac{H_{ij}f_j^{(n)}y_i}{\sum_{k\in I_i} H_{ik}f_k^{(n)}} ln(H_{ij}f_j) - (H_{ij}f_j)\right] \tag{2.16}$$

where X is the number of pairs of photons emitted from voxel j and detected in projection i, and it is related to y_i by:

$$y_i = \sum_{j\in I_i} X_{ij} \tag{2.17}$$

- Maximisation step (M step): This step then finds the image which best maximises the log-likelihood of the previous E step computation. This is done by obtaining the partial derivatives as shown in equation 2.18:

$$\left.\frac{\partial E(P(X,f) \mid Y, f^{(n)})}{\partial f_j}\right|_{f=f^{(n)}} = \sum_{i\in J_j}\left[\frac{H_{ij}f_j^{(n)}y_i}{\sum_k H_{ik}f_k^{(n)}} f_j^{-1} - H_{ij}\right] = 0 \tag{2.18}$$

where J_j is the set of projections to which voxel j contributes.

The resulting formula (equation 2.19) is the MLEM algorithm:

$$f_j^{(n+1)} = \frac{f_j^{(n)}}{\sum_{i \in J_j} H_{ij}} \sum_{i \in J_j} H_{ij} \frac{y_i}{\sum_{k \in I_i} H_{ik} f_k^{(n)}} \tag{2.19}$$

The resulting image estimate $f_j^{(n+1)}$ will be put back into the E step and the iteration will continue until convergence is attained.

However, there are two major limitations of this algorithm: (1) it is computationally demanding, and (2) the rate of convergence is slow. This has led to the introduction of the ordered subsets expectation maximisation (OSEM) algorithm which gives a huge improvement over MLEM in terms of less computational time and faster convergence.

OSEM involves the iterative use of ordered subset scheme for convergence acceleration and data update (Hudson and Larkin [1994]). In OSEM, the projection data is organised into ordered subsets and the MLEM algorithm is then applied to each subset in turn. The image obtained after each subset now becomes the starting point for the next subset. Each step is referred to as sub-iteration, and so every full iteration passes through all the subsets.

The OSEM algorithm is derived from the MLEM algorithm by substituting the sum over i with the sum over $i \in S_b$ in Equation 2.19. S_b is the subset of the detector pairs, and $b = 1, ..., B$, where B is the subset number:

$$f_j^{n+1} = \frac{f_j^{(n)}}{\sum_{i \in S_b} H_{ij}} \sum_{i \in S_b} H_{ij} \frac{y_i}{\sum_k H_{ik} f_k^{(n)}} \tag{2.20}$$

The faster convergence in OSEM comes at the expense of increased image noise, which becomes magnified after each iterations. Therefore, in clinical prac-

tice, the noise magnification is often addressed by stopping the reconstruction at about 2-3 iteration (Ahn et al. [2015]) or by applying a Gaussian post-filter to the reconstructed images (Hamill and Bruckbauer [2002]).

2.4.3 Image Quantification

PET involves visual inspection of images for traditional evaluation. However, its potential lies majorly in its ability to provide quantitative evaluation. This is often measured by a semi-quantitative parameter referred to as SUV (Naqa et al. [2007]) and expressed as:

$$SUV = \frac{Activity\ Concentration\ in\ a\ Pixel\ (MBq/mL)}{Injected\ Radioactivity\ (MBq)/Body\ Weight\ (g)} \tag{2.21}$$

Using this equation, the unit of SUV would be g/mL. However, SUV is often measured as a dimensionless unit with the assumption that 1 mL of tissue weighs 1 g (Kinahan and Fletcher [2010]).

SUV provides relatively objective tumour characterisation, reliable differential diagnosis and earlier treatment response evaluation and monitoring (Boellaard [2009], Adams et al. [2010]). SUVs can be reported as the maximum value of all voxels, SUV_{max}, or the mean value over all voxels, SUV_{mean}, within the defined region of interest (ROI). A decrease in SUV can often be used as an indicator for therapy response, however, there is currently no established protocols with regards to this (Shankar et al. [2006], Tani et al. [2016]). This is because SUV depends on other parameters beyond the user's control. These parameters could be biological factors such as body size and blood glucose level (Hoekstra et al. [2000], Weber [2006], Westerterp et al. [2007]), or inter-observer issues such

as defining regions of interest and reconstruction methods (Hoekstra et al. [2002], Westerterp et al. [2007], Adams et al. [2010]).

2.4.4 Factors Affecting Quantification of PET Images

PET is being regarded as a quantitative imaging tool due to its ability to map the radiotracer concentration in the human body with accuracy and precision. However, there are some factors which greatly affect the accuracy and precision of PET measurements. This informs the need for proper correction of acquired PET data to enhance better quantification. The mode of correction is dependent on the scanner, but a general sequence of correction is presented in this thesis.

2.4.4.1 Attenuation

Attenuation is the reduction in photon intensity as it transverses through matter. The bigger or more dense the matter is, the more the photons are attenuated. Attenuation is expressed as:

$$I = I_o e^{-\mu T} \tag{2.22}$$

where μ is the linear attenuation coefficient and T is the thickness. μ at 511 keV is approximately 0.028 cm^{-1} for lung, 0.096 cm^{-1} for soft tissue, and 0.14 cm^{-1} for bone.

If image reconstruction is carried out without correcting for attenuation, less dense organs like the lungs appear to have higher uptake than denser areas, resulting in artefacts. This has negative impact on tumour visualisation and quantification (Bromiley et al. [2001]).

Attenuation correction (AC) is done in a hybrid PET/CT scanner using the

CT image to correct for attenuation of PET emission data. This technique is more advantageous than the earlier method of acquiring PET transmission scan using ^{68}Ga or ^{68}Ge sources in that the acquired image is less noisy, insensitive to emission contamination and can be acquired within shorter time (Kinahan et al. [2003]). However, since the CT data are acquired as a weighted average of photon energies (from 30-140 keV), they need to be converted into the corresponding estimate of PET photon energies (511 keV) (Kinahan et al. [2003], Ay et al. [2011]). The converted CT image is referred to as CT attenuation correction (CTAC) image which now has a resolution similar to the PET image. CTAC can be generated using three approaches: dual-kVp CT scans, segmentation, and scaling. Of all three, the scaling method is the simplest and widely used approach as it closely approximates the electron density as a function of CT number in most tissues (Schneider et al. [2000], Abella et al. [2012]).

In the software for tomographic image reconstruction (STIR) library, attenuation is estimated by forward projecting the attenuation coefficient image obtained from the scanner.

2.4.4.2 Scatter

Positron annihilation does not always occur along a straight LOR. There is a probability that one or more photons might have been scattered through Compton scattering, thereby losing part of its energy (as shown in Figure 2.6b). In most PET systems, energy window is typically set between 450 and 650 keV. So, it is not easy to discriminate scattered coincidences from true coincidences and this results in poor resolution and loss of contrast.

Typical scatter correction employed in three-dimensional (3D) PET imaging

works on the principle of single scatter simulation (SSS) algorithm (Watson et al. [1996]) as estimated in STIR (Tsoumpas et al. [2004]). This estimates scatter contributions with emission and transmission images. Scatter points are randomly selected in the attenuation image using a threshold. For each point, the probability for a photon to be scattered and detected are evaluated using Klein-Nishina formula (Klein and Nishina [1994]). The scatter probabilities are then summed for each point in a transmission image and detector pair to estimate the distribution, and then scaled using a tail-fit method, a fit to match the tails of the measured data at each projection. The tail-fitting is done to account for multiple scatter and events outside the field of view (FoV) (Thielemans et al. [2007]). The scattered event estimate is subtracted from the random-corrected prompts (Polycarpou et al. [2011]) and the new estimate is used in the next iteration.

2.4.4.3 Random

Random coincidences arise from the infinite width of the time window used for true coincidence detection. This gives allowance for two uncorrelated single events to be mistakenly detected as true coincidence, as shown in Figure 2.6c. Random coincidences are significant in PET imaging, specifically for very high activity and for 3D acquisition. The fractions of randoms in regions of high attenuation are often large, and these could lead to great errors if uncorrected (Bailey et al. [2005]).

Randoms can be reduced by making the coincidence window smaller. However, caution must be taken not to make this too small, else, true coincidences may be lost due to different arrival time. This implies that coincidence window

selection is a trade-off between random minimisation and loss of sensitivity. Consequently, the coincidence window is often set to about 3-4 times the FWHM timing resolution.

Random coincidences are generally corrected by tail fitting (for distribution in sinogram or projection space) (Karp et al. [1990]); estimation from singles rates as employed for GE Signa PET/MR scanner (Michel et al. [1998], Stearns and Lonn [2011], Grant et al. [2016]); or from delayed coincidence channel estimation as commonly used in Siemens mMR scanners (Delso et al. [2011]).

2.4.4.4 Normalisation

There is often non-uniformity in PET acquired data resulting from instrumentation errors, variation in detector's efficiency, or geometry effect. Knowledge of the extent of this variation is important in reconstruction so as to remove artefacts in PET images, and the method for correcting this is called normalisation.

Normalisation is often done by exposing the whole detector to a uniform radiation while estimating the number of counts recorded by each detector pair. Ideally, all detector pairs should record the same counts but this is not so in practice due to efficiency variation. So a normalisation factor, $Norm_{i,j}$, is needed for each detector pair, and this is given as:

$$Norm_{i,j} = \frac{N_{i,j}}{< N >} \tag{2.23}$$

$< N >$ is the average value of $N_{i,j}$ for all detector pairs. The corrected count $C_{Norm_{i,j}}$ is then obtained for the recorded counts in each detector pair $C_{i,j}$ using:

$$C_{Norm_{i,j}} = \frac{C_{i,j}}{Norm_{i,j}} \tag{2.24}$$

Normalisation data are often stored in the PET raw data, and they can be extracted using some software utilities like STIR. The different normalisation components such as crystal efficiency and geometry factors, as well as time window misalignment between blocks are estimated using the maximum likelihood approach (Hogg et al. [2001]).

2.4.4.5 Partial Volume Effect

Partial volume effect (PVE) is primarily caused by the poor spatial resolution of PET images, as well as the discrete image sampling (Aston et al. [2002]). However, motion (patient, respiratory and cardiac), and errors in activity distribution (due to tracer uptake and washout) can introduce additional PVE (Frey et al. [2012]).

PVE has been linked to a significant false-positive and false-negative results in lesion quantification, and in some cases, lesions could be totally missed. PVE is more pronounced in smaller objects whose spatial dimension is less than 2 to 3 times the FWHM resolution of the scanner (Ptacek et al. [2014]). Larger objects might also experience intensity reduction around the edges, resulting in blurring, but the activity at the center will still be preserved.

This effect is also known as spill in effect because there is a cross-contamination of activity from hot regions to cold regions, leading to underestimation and overestimation in image quantification (Rousset et al. [2007]). Spill in effect from hot region such as the bladder has been identified in many studies as spill in effect (Bai et al. [2013], Silva-Rodriguez et al. [2016]), shine-through effect (Liu

[2012]), halo-artifact (Heuber et al. [2017]), or broadly as partial volume effect (Soret et al. [2007]). Many believe this effect arises from no or inaccurate attenuation and scatter correction (Heuber et al. [2017], Afshar-Oromieh et al. [2014]), while others believe it depends on choice of radiotracers, imaging modality and clinical practice (Bouchelouche and Oehr [2008], Chondrogiannis et al. [2014]). However, there is currently no established evidence to these allusions (Heuber et al. [2017]).

2.5 Multi-modal Imaging

In recent years, attention is being shifted to multi-modal imaging techniques which could combine anatomical information from CT and MRI with the functional information obtained from PET (or SPECT). PET scanners integrated with CT (PET/CT) or MRI (PET/MR) are being developed and are finding their ways as effective and efficient imaging modalities for clinical and commercial interest (Beyer et al. [2002], Ell and von Schulthess [2002]). Combining anatomical with functional information is aimed at improving the throughput for clinical (and preclinical) studies, and also providing additional information that would be rather difficult to obtain using different scanners (Cherry [2009]).

2.5.1 PET/CT Imaging

PET/CT is the most developed multi-modality technique in medical imaging. Its high performance and spatial resolution is largely due to the combination of precise molecular image fusion from PET with the high-quality anatomical images from CT. These combined anato-molecular images can be generated with

the help of high performance computer software. PET/CT is primarily used in oncology (Beyer et al. [2002]), but it also has applications in clinical and research cardiology (Carli and Dorbala [2007]), as well as identification of brown fat which has implication for diabetes-related metabolic disorders (Cohade et al. [2003]). Another importance of PET/CT imaging is that the CT image can be used to correct for attenuation and scatter, while reducing the total imaging time (Kinahan et al. [2003]) as previously discussed.

2.5.2 PET/MR Imaging

Following the implementation of combined PET/CT scanners in clinical practice, efforts are being made towards the development of PET/MR scanners (Townsend [2008]), although this is a bit slower due to the inherent technical challenges from combining both modalities (Vaquero and Kinahan [2015]). This is because conventional PET systems use photomultiplier tubes (PMTs) which are highly sensitive to magnetic fields. One possible approach to overcome this issue is the use of active PMTs shield to spatially separate the PET and the MR systems. This was implemented in the first whole-body PET/MR, the Philips Ingenuity TF PET/MR system (Zaidi et al. [2011]). Alternative approach is the use of solid state photo-detectors like avalanche photodiodes (APDs) and silicon photomultipliers (SiPMs). This is the approach used for the Siemens Biograph mMR (Delso et al. [2011]) and the GE Signa PET/MR (Grant et al. [2016]).

The potential value of combined PET/MR imaging lies in its better soft tissue contrast produced by MR compared with CT. This would allow a more accurate localisation of the high uptake PET region, while avoiding the additional CT radiation dose (Disselhorst et al. [2014], Musafargani et al. [2018]). Also,

PET/MR imaging is capable of achieving truly simultaneous imaging, thereby reducing the effect of motion-induced blurring. At the moment, emphasis is being placed on comparing the diagnostic value of PET/MR imaging with PET/CT, and recent studies have demonstrated that this is not significantly different (Al-Nabhani et al. [2014]).

2.5.3 Challenges in Multi-modal Imaging

The advantage of multi-modal imaging system over stand-alone systems comes with a trade-off between improved imaging performance and cost. It also comes with increased complexity which requires expertise across both, or all, of the combined modalities. However, the afore-mentioned challenges are mild compared to the more severe ones highlighted below:

2.5.3.1 Image Registration

For quantitative accuracy of multi-modality imaging, PET functional images and anatomical images from CT or MR need to be accurately aligned, and this is referred to as image registration. Due to respiratory motion, there is often a misalignment between PET and CT images especially at the level of the diaphragm. This affects the assignment of attenuation coefficients to structures around the diaphragm, leading to misalignment artefacts. Although this does not often cause major diagnostic problems (Osman et al. [2003]) but there are situations in which accurate registration of PET and CT images is necessary, like in the treatment planning of basal lung cancer (Hicks et al. [2007]). In such cases, there may be need for respiratory gating of PET and CT images, which is complex and time consuming (Nehmeh et al. [2004]). Various software are being

developed for accurate registration of different body tissues and organs.

2.5.3.2 Motion Correction

Although in PET/CT imaging, the PET and CT images are acquired nearly simultaneously, there is a short time delay between the first acquired CT image and the PET image. There is therefore a possibility of motion between CT and PET acquisitions, which could potentially lead to some errors in the diagnosis or staging (Vaquero and Kinahan [2015]). For PET/CT imaging, the most significant form of motion is the respiratory motion which could significantly affect the imaging of the lung and abdomen. This type of motion causes blurring, hence leading to shape distortion and loss of signal (Liu et al. [2009]). It could also lead to a mismatch between PET and CT, leading to errors in AC. Several approaches are being used to compensate for motion effect, with the most direct approach being the use of respiratory gated CT and PET images (Kinahan et al. [2006], Nehmeh and Erdi [2008]).

The respiratory motion effect is not so pronounced in PET/MR imaging. In fact, simultaneous PET/MR imaging provides accurate respiratory-gating signals, which can be used for motion correction (Chun et al. [2012]).

2.5.3.3 Attenuation Correction

A major challenge in PET/MR imaging is attenuation correction (AC). In PET/CT imaging, the attenuation correction factors (ACF)s can be derived from the CT image because photon scattering is affected by the same processes in PET and CT. However for PET/MR imaging, image values are representative of weighted average of the hydrogen proton density, as well as T_1 and T_2 relaxation times

which are not related to photon attenuation. These values are further influenced by the environment, thereby causing a mismatch between PET and MR (Liang and Lauterbur [1999]). In essence, no simple scaling method can be sufficiently used to convert the MR image to CT-equivalent attenuation map. Several approaches are being used for AC but the most common approach is the use of image segmentation. Tissue classes are segmented from the MR image into air, lungs, fat and soft tissues; and a uniform attenuation coefficient is then assigned to each class. Bone are not classified in this approach because MR does not show signal in the bone due to its short relaxation time. This can lead to a significant error in estimating PET uptake in bony structures such as the spine. However, the segmentation approach is currently the most robust method for lung imaging (Martinez-Moller et al. [2009]). Other approaches are also being used for AC which include population-based methods where several patient data are used to create an atlas (Hofmann et al. [2011]) or a training sample for machine learning (Liu et al. [2017]); and the data-driven methods which use information from PET data to create an attenuation map (Mehranian and Zaidi [2015]).

Although AC is not a challenge in PET/CT imaging, if there are errors or artefacts in the CT image maybe due to the use of contrast medium or the presence of metallic implants, these artefacts could potentially be transferred to the PET image through the AC process, thereby affecting accurate quantification (Boas and Fleischmann [2012], Hsieh [2015]).

2.5.3.4 PET Calibration

In PET/CT, PET calibration and quality control are often carried out using water-filled phantoms. But this is challenging in PET/MR imaging because the

water phantoms show artifacts and inhomogeneities when imaged at the 3T field strength of current PET/MR systems (Quick [2014]). Oil would have been a better alternative, but this is challenging because FDG does not dissolve well in oils (Ziegler et al. [2013]). Development is however underway for phantom fluids which could effectively be used for calibration and quantification procedures in PET/MR imaging (Vaquero and Kinahan [2015]). Also, with the emerging field of 3D printing technology, there is a potential indication that a single 3D printed phantom can be used for imaging or dosimetry measurements in different imaging acquisitions and modalities (Filippou and Tsoumpas [2018]).

2.6 Partial Volume Correction Techniques

Partial volume correction (PVC) is essential in PET imaging for enhanced quantitative accuracy and better lesion detection (Hofheinz et al. [2012], Thomas et al. [2016], Cysouw et al. [2017], Munk et al. [2017]). Various techniques are being employed for PVE correction and these can be implemented at voxel level (e.g. point spread function (PSF)-based reconstruction, multi-resolution and partition methods) or at ROI level (e.g. recovery coefficient correction, geometric transfer matrix (GTM) and deconvolution method) (Geworski et al. [2000], Frouin et al. [2002], Cal-Gonzalez et al. [2018]). They can be classified broadly into two categories, namely: (a) post-reconstruction methods (e.g. recovery coefficient correction, GTM), local projection (LP) technique and (b) within-reconstruction methods (e.g. PSF-based reconstruction, BC technique and Bayesian approaches) (Rousset et al. [2007], Soret et al. [2007], Moore et al. [2012]). Some correction techniques require a priori information about the lesion shape and size, hence

increasing the possibility of erroneous estimation when this information is not precisely known. They might also be computationally demanding (Cal-Gonzalez et al. [2018]). Given the added advantage of multi-modal imaging as previously discussed, some PVC techniques can be further classified as data-driven (when they rely only on PET data) or anatomical-based (when additional information is provided by the anatomical components).

A detailed description of the correction approaches used in this thesis is presented below:

2.6.1 PSF Reconstruction

PVC is mostly implemented using a homogeneous, Gaussian-shaped PSF of the scanner which is specified by its FWHM in every direction. Implementation of PSF is referred to as resolution recovery technique and it is specific for each scanner.

PVC can be done by incorporating the system PSF into the OSEM reconstruction in both forward and backward projections (Alessio et al. [2010], Rapisarda et al. [2010], Rogasch et al. [2014]) as illustrated in Equation (2.25).

$$H_{ij} = \sum_{k} H_{kj} PSF_{ik} \tag{2.25}$$

where H_{kj} represents the system matrix, and H_{ij} is the system matrix convolved with the system PSF in both forward and back projections.

The PSF can either be modelled as a spatially-variant or spatially-invariant model. With spatially-invariant, it is assumed that the PSF is the same everywhere in the imaging space, while for spatially-variant, the PSF changes depend-

ing on the object location in the FoV.

Spatially-variant PSF model is the most accurate and mostly implemented in medical imaging. This needs a careful modelling of the system matrix and an accurate description of the PSF model which is not always straightforward. Monte carlo simulations are often accurate but they are computationally demanding. So alternatively, an empirical measurement of the PSF can be done. Although this is a lot easier, but it becomes cumbersome to acquire a point source which can cover the entire FoV of the PET scanner (González et al. [2011]). Also, in order to obtain a significant activity recovery of the PET image, the iteration needs to run fully until convergence. However, this increases the image noise, and also introduce Gibbs (edge) artifacts to the PSF-based reconstructed images (Thielemans et al. [2010]).

Due to the complexities and computational demands associated with the use of a spatially-variant model, a spatially-invariant model of the PSF was used in this thesis. Although this choice might limit the performance of the PSF algorithm in correcting for the spill in effect, but previous works have reported similar behaviour between the two models in terms of resolution, contrast and noise metrics (Teo et al. [2007], Alessio et al. [2010]).

2.6.2 Other Correction Techniques

Apart from PSF reconstruction, other PVC techniques are also used in the literature, but these are commonly applied to brain imaging. The first method was the use of phantoms to generate correction factor (also called recovery coefficient (RC)). This was expressed as the ratio of the reconstructed count density and the true count density in small regions. RCs are normally 1 for larger objects,

these values are then applied to small structures to correct for PVE. However, this approach is very tedious. Moreso, the sizes of the in vivo structures are not precisely known, so this technique might not be accurate for these structures.

A pixel-by-pixel correction method was then proposed by (Videen et al. [1988]) using anatomical images from high resolution CT to segment the brain. Convolution was done on the segmented images using a Gaussian PSF of the scanner to create corrected tissue image. The original PET image is then divided by the corrected tissue image on a pixel-by-pixel basis to yield a corrected PET image.

This technique was extended to three-dimension (3D) by (Meltzer et al. [1990]) using standard MRI T_2 weighted pulse sequences which provide greater accuracy. However, these techniques could only correct for spill out counts, and not spill in assuming no background activity. So the method was further developed by (Muller-Gartner et al. [1992]) to account for spill in effects.

Despite the efficiency of this above method, it cannot be directly applied in certain circumstances where parameters vary during acquisition, e.g bladder imaging where bladder volume and activity vary during acquisition. So, segmenting from CT will result in mismatch between PET and CT images since they are not acquired simultaneously. This therefore implies that PET segmentation will be particularly useful for bladder correction (Heiba et al. [2009], Silva-Rodriguez et al. [2016]). Also, instead of just dividing the original image with the corrected tissue image, it would be better to incorporate the correction into the reconstruction algorithm.

Based on these reasons, a background correction technique was proposed by (Silva-Rodriguez et al. [2016]) using the concept of PET segmentation and

reconstruction-based correction method (Tsoumpas and Thielemans [2009]).

2.6.3 Segmentation and Reconstruction-based Background Correction (BC) Technique

Correction methods have been proposed and incorporated into MLEM reconstruction algorithm since it does not take random and scatter events into account. So in order to correct the final image, the algorithm can be extended by adding an additive term which will account for random and scatter (Lange and Carson [1984]) as shown in equation 2.26:

$$y_i = \sum_{j \in I_i} X_{ij} + A_i \tag{2.26}$$

A_i has a poisson distribution with an expected value a_i. This additive term could then be included in the E step to give the result in equation 2.27:

$$f_j^{n+1} = \frac{f_j^n}{\sum_{i \in S_b} H_{ij}} \sum_{i \in S_b} H_{ij} \frac{y_i}{\sum_k H_{ik} f_k^n + A_i} \tag{2.27}$$

Also, one of the common ways of reducing partial volume effect is through soft segmentation. This approach gives allowance for uncertainties around the boundaries, thereby retaining more image information as opposed to the standard method of hard segmentation (Pham et al. [2000]). Segmentation involves the use of a characteristic function which indicates whether a pixel is inside a particular set or not.

Given a location j ε I, the characteristic function χ_k(j) of set R_k can be defined

as:

$$\chi_k(j) = \begin{cases} 1 & \text{if } j\varepsilon R_k \\ 0 & \text{otherwise} \end{cases} \tag{2.28}$$

Similar segmentation and correction techniques were used by Silva-Rodriguez et al. [2016] to correct for the spill in activity from the hot background region into the colder one, using bladder as a case study. The first step was to delineate the hot region using the soft segmentation approach where R_j is 1 in the hot region and 0 outside. The segmented hot region, B, was now obtained using equation (2.29):

$$S_j = R_j f_j^N \tag{2.29}$$

where f_j^N is the reconstructed image at iteration N, and S_j is the pixel value on the segmented mask. This will then be forward projected into the sinogram space using equation (2.30)

$$P_i = \sum_j H_{ij} S_j \tag{2.30}$$

P_i is the contribution from the hot region which is now included as a background term in the reconstruction, as expressed in equation (2.31)

$$f_j^{n+1} = \frac{f_j^n}{\sum_{i \in S_b} H_{ij}} \sum_{i \in S_b} H_{ij} \frac{y_i}{\sum_k H_{ik} f_k^n + A_i + P_i} \tag{2.31}$$

A general layout of the background correction is shown in Figure 2.9

The convergence property of the BC technique depends on the size and activity of the background region. Big and active regions tend to converge faster, but for smaller regions, a higher number of iteration might be required to ensure an

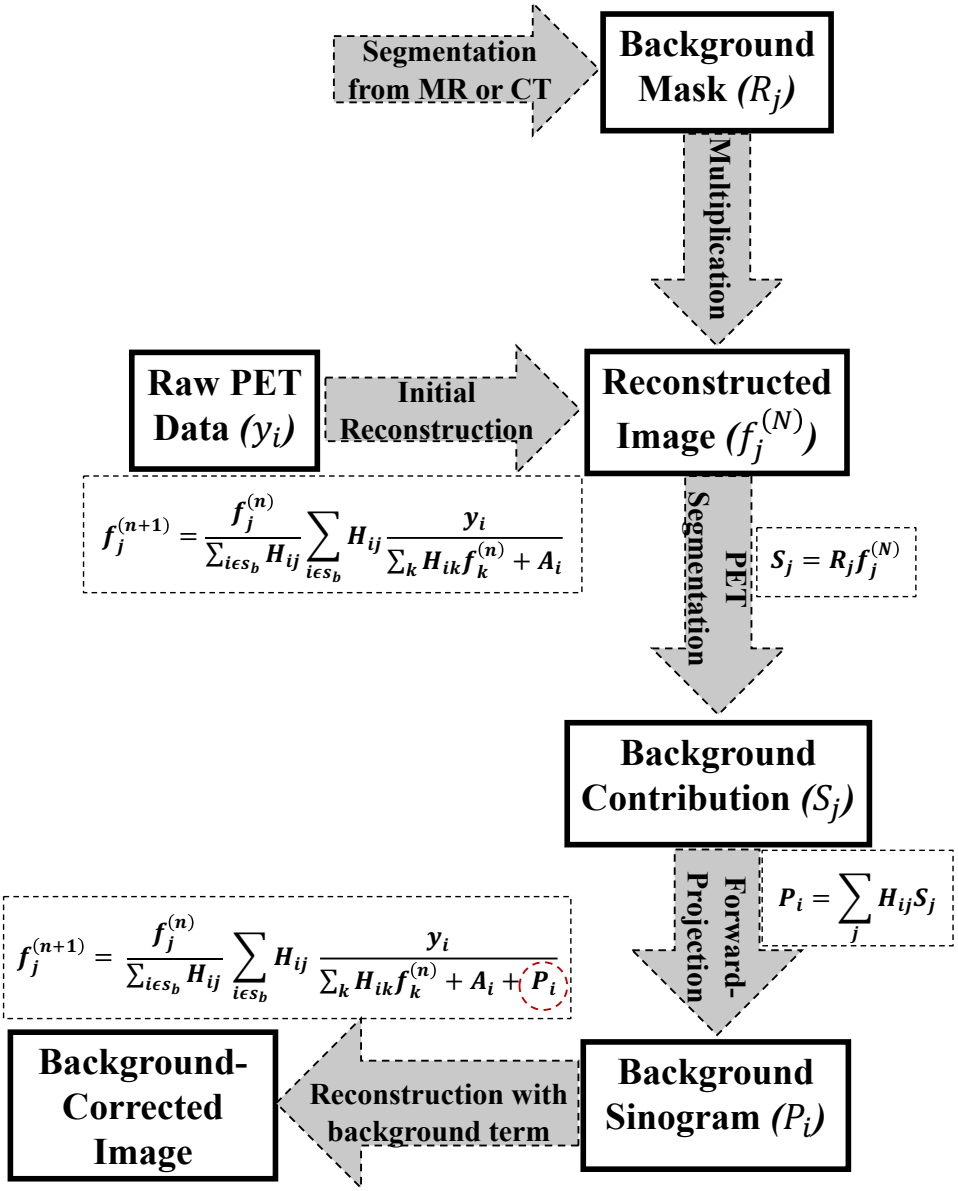

Figure 2.9: Flow sequence of the background correction technique

adequate convergence (Akerele et al. [2018]). The BC technique also depends on the segmentation accuracy of the background region. Inaccurate segmentation might affect the quantification of proximal lesions to the background region.

2.6.4 Local Projection (LP) Technique

Another recent approach to compensate for the partial volume and spill in effects is the LP technique (Moore et al. [2012], Cal-Gonzalez et al. [2018]. Consider a reconstructed image consisting of a detected lesion with high uptake. Quantification in the lesion can be improved by introducing information derived from high-resolution segmentation, and removing background activity from neighbouring tissues. This is the basic principle of the LP technique. So, the image is segmented into the target volume of interest (VOI) and a global background outside the target VOIs. The VOI consists of one or more different tissues, including the lesion of interest, and the activity concentration in the different tissues is represented by the average value inside each tissue. It could also be assumed that voxels belonging to the same tissue have a more similar activity than voxels belonging to different tissues.

In this thesis, the image to be corrected is basically made up of the target lesions, an hot region which is responsible for the spill in of activity into the target lesions, and the global background. Therefore, the image is segmented into a target VOI (consisting of the lesion and the hot region ROIs), and the global background outside the target VOI. The measured emission projection counts, y_i, can be modelled as the sum of the projection counts from the 2-tissue VOI, plus the counts originating from the global background outside the VOI, as shown in Equation 2.32:

$$y_i = \sum_{j=1}^{J} V_j C_{ij} + g_{out,i} \tag{2.32}$$

y_i are the expected counts per sinogram bin i, V_j is the activity and C_{ij} is the

system matrix for each segmented tissue in the VOI, while $g_{out,i}$ is the counts coming from the global background outside the target VOI.

Partial volume correction using the LP technique is performed as a post-reconstruction step. The system matrix values, C_{ij}, for each segmented tissue and the global background, $g_{out,i}$, are first computed. Then, the LP tissue-activities, V_j, are obtained by maximizing the log-likelihood for the expected value, y_i, as shown in Equation 2.33.

$$\sum_{j'=1}^{J} V_{j'}^{(k)} \left[\sum_i \frac{C_{ij'} C_{ij}}{y_i^{(k)}} \right] = \sum_i \frac{C_{ij} \left(n_i - g_{out,i}^{(k)} \right)}{y_i^{(k)}} \tag{2.33}$$

where n_i are the measured count per sinogram bin. This equation is solved iteratively where the values of y_i, V_j and $g_{out,i}$ are updated after each iteration (k). The resulting tissue activity is then substituted in place of the original activity in each voxel within the target VOI. The resulting image is forward-projected and the obtained sinogram is reconstructed with STIR library. The forward projector used is based on Siddon's matrix ray tracing algorithm with 10 tangential rays traced for each projection bin. A flow chart of the LP method is given in Figure 2.10.

2.6.5 Hybrid Kernelized Expectation Maximization (HKEM) Technique

Since the advent of dual/multi-modal imaging scanners, several anatomically-driven reconstruction methods have also been proposed with the intent of exploiting the dual information provided by these scanners. Most of these methods

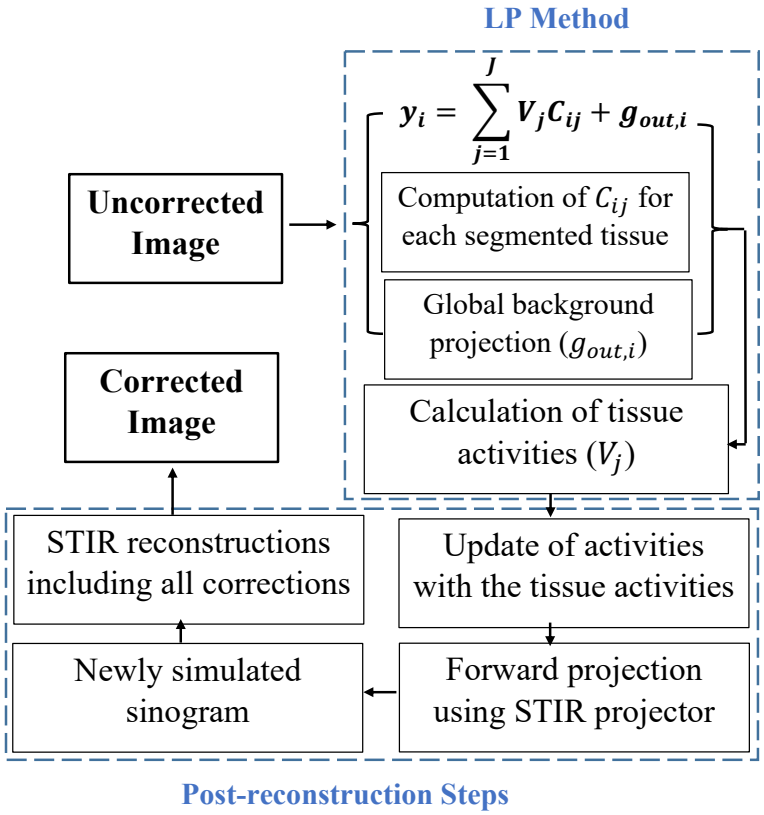

Figure 2.10: Flowchart of the LP method.

are based on the Bayesian approach which maximises the posterior density function instead of the Poisson density function. These methods have been shown to produce promising results in terms of quantification and image quality. (Vunckx et al. [2012], Ehrhardt et al. [2016], Yang et al. [2018]).

Recently, an hybrid kernelised expectation maximisation (HKEM) method was proposed (Deidda et al. [2019a,b,c]), which uses information from both PET and an anatomical image in order to compensate for partial volume effects. The advantage of the HKEM method is that it does not require segmentation and it achieves improved resolution for each individual voxel and also for the edges of a region (Bland et al. [2017, 2018]). This technique, although it is not a

dedicated partial volume correction technique, was used so as to explore the edge-preserving and noise-suppression performance in enhancing resolution recovery and reducing the spill in effect from the hot background into the colder ROIs (Belzunce et al. [2018]). The HKEM method re-parameterizes the expectation maximisation (EM) algorithm in terms of spatial basis functions (kernel matrix, K) and coefficients (α). Therefore, the image to be reconstructed, f_i, can be expressed as:

$$f_i = \sum_{m=1}^{M} \alpha_m k_{mj} \tag{2.34}$$

where k_{mj} is the mj^{th} element of the kernel matrix, and α_m is the coefficient vector to be estimated in the EM step as shown in Equation 2.35:

$$\alpha_m^{(n+1)} = \frac{\alpha_m^{(n)}}{\sum_l k_{lm}^{(n)} \sum_i H_{il}} \sum_l k_{lm}^{(n)} \sum_l H_{il} \frac{y_i}{\sum_b H_b \sum_q k_{qb}^{(n)} \alpha_q^{(n)} + A_i} \tag{2.35}$$

Since the HKEM method extracts information from both anatomical and PET images, the kernel matrix can then be expressed as:

$$k_{im}^{(n)} = k_a(\nu_m, \nu_i).k_p(z_m^{(n)}, z_l^{(n)}) \tag{2.36}$$

where k_a and k_p are the kernel components from attenuation and PET images respectively, calculated using the functions in Equations 2.37 and 2.38:

$$k_a(\nu_m, \nu_i) = \exp\left(\frac{-\left|\left|\nu_m - \nu_i\right|\right|^2}{2\sigma_a^2}\right) \exp\left(\frac{-\left|\left|x_m - x_i\right|\right|^2}{2\sigma_{da}^2}\right) \tag{2.37}$$

$$k_p(z_m^{(n)}, z_i^{(n)}) = \exp\left(\frac{-\left|\left|z_m^{(n)} - z_i^{(n)}\right|\right|^2}{2\sigma_p^2}\right) \exp\left(\frac{-\left|\left|x_m - x_i\right|\right|^2}{2\sigma_{dp}^2}\right) \tag{2.38}$$

ν_m and $z_m^{(n)}$ are the feature vectors calculated from the attenuation image and the n^{th} iteration PET image, α, respectively, while σ_a, σ_p, σ_{da} and σ_{dp} are scaling parameters for the distances in Equations 2.37 and 2.38. The choice of these parameters is important as big values for σ_{da}, which is related to the MR image, causes artefacts at the borders between different tissues (Deidda et al. [2019b,c]. Preliminary investigation (Deidda et al. [2019c]) has shown that σ_{dp}=0.5 or σ_p=0.3 is the optimum value for accurate quantification in small lesions. It is better to use a higher σ_p for a very noisy data, in order to obtain a smoother image. However, this will be at the expense of quantification accuracy (Deidda et al. [2019a,c]).

Chapter 3

Validation of the Background Correction Method for the Suppression of Spill in Effects Near Highly Radioactive Regions in PET

In the previous chapter, various PVC techniques were discussed. The BC technique was also discussed as a prospective method to correct for the spill in effects in regions near high activity regions. This section investigates the spill in effect and the performance of the BC method in mitigating this effect, using bladder as a case study of the highly radioactive region.

This chapter consists of work previously published in Akerele et al. [2017, 2018].

3.1 Introduction

Despite the wide applicability of PET, concerns are being raised on the effectiveness of some common PET tracers in imaging areas with high radiotracer uptake (hot regions) such as the brain (Soret et al. [2007]), urinary bladder (Liu [2012], myocardium (Du et al. [2013]) and spine (Forsythe et al. [2018]). These concerns stem from the observation that activity from the hot regions may interfere with PET quantification and visualisation of nearby lesions, tumours and abnormalities due to PVE (Liu [2012], Gaertner et al. [2013], Afshar-Oromieh et al. [2014]). As a result, nearby lesions have their SUVs overestimated, and in some cases, lesions can be totally missed (Liu [2012]). Several techniques are being employed to solve the quantification issues but this has not been sufficiently explored for the case of spill over activity from hot regions, such as the bladder, to adjacent lesions.

The urinary bladder is a hollow, muscular and distensible (elastic) organ, sitting on the pelvic floor, where urine produced by the kidneys is stored. Urine enters the bladder through the ureters and exits through the urethra. The bladder is constantly filling (with a volume between 600ml and 1000ml) (Hole [1981], Auday [2018]) and a region of very high activity in PET imaging because the injected radiotracers are excreted through the kidney and the urinary bladder. Bladder filling varies from patient to patient but generally, bladder fills naturally at a rate of 1-2 ml/min. Although after diuretic, stable bladder has physiological filling rates between 10-20 ml/min while fast filling is about 100 ml/min (Getliffe and Dolman [2007]).

Several researches have been conducted on the application of [^{18}F]-FDG

PET/CT for the prediction of post-therapeutic tumour response in locally advanced rectal cancer (Guillem et al. [2004], Cascini et al. [2006], Capirci et al. [2007], Ben-Haim and Ell [2009]), ovarian cancer (Avril et al. [2005]) and uterine cancer (Nishiyama et al. [2008]). In these studies, SUV variation was used to predict therapy response, discriminate responders from non-responders, as well as predict long-term outcome. Evidence of SUV reproducibility has also been established for malignant tumours when taken several days apart (Nahmias and Wahl [2008]).

However, assessment of bladder activity and its effects on surrounding organs is complicated because FDG accumulates in the bladder, and this in turn interferes with visualisation of pelvic and abdominal abnormalities. This accumulation however varies from patient to patient, being dependent on patient hydration, kidney function and blood glucose level. Research has shown that hydrated patients have higher FDG excretion than dehydrated ones (Moran et al. [1999]), and in situation of normal blood glucose level and kidney function, FDG excretion could potentially vary between 5 - 15 % of the injected dose (Bach-Gansmo et al. [2012]).

The high activity from the bladder can potentially mask findings in surrounding regions such as the prostate, falsify uptake values and subsequently influence patients' diagnosis (Heuber et al. [2017]). This can as well impair tumor visibility and staging around the pelvic region because it interferes with the ability to distinguish wall activity from luminar activity (Bouchelouche and Oehr [2008]). A recent work by Silva-Rodriguez et al. [2016] showed an overestimation in lesion uptake as high as 41.3% and 22.2% for SUV_{max} and SUV_{mean} respectively due to spill over activity from the bladder. This quantification issue was also reported

by Liu [2012] who concluded that SUV values for lesions within 40-50 mm from the hot source are often overestimated and therefore invalid.

Many attempts towards correcting this issue have been made. For example, in clinical practice, the spill in effect from the bladder to the surroundings is often addressed using techniques such as bladder voiding prior to PET examination, catheterisation, bladder irrigation and retrograde filling, and use of alternative tracers (Koyama et al. [2003]). However, none of these techniques have been proven to be effective (Kosuda et al. [1997], Moran et al. [1999], Massaro et al. [2012], Bach-Gansmo et al. [2012], Lo et al. [2014]). They are also uncomfortable and invasive for the patients (Lo et al. [2014]), whereas PET is meant to be a minimally-invasive imaging technique. Due to these challenges, alternative tracers are sometimes used because of their minimal urinary excretion (Witney et al. [2012], Beheshti et al. [2013], Rauscher et al. [2016]), but such tracers still have some limitations with regards to patient sensitivity and specificity (Steiner et al. [2009]). These issues clearly suggest the need for a more practical correction technique for the spill in of activity from hot regions to the surroundings due to its negative implication on lesion quantification, visibility and staging.

A recent novel simulation study (Silva-Rodriguez et al. [2016]) suggested a reconstruction approach to correct for the high physiological radioactive concentration in order to address these aforementioned issues and improve lesion quantification. This method involves segmentation, forward-projection and reconstruction-based correction. However, the performance of this correction method on a state-of-the-art scanner, including accurate iterative scatter correction and point-spread-function (PSF) correction inside the reconstruction remains to be studied. The previous work used the General Electric (GE) Advance NXi scanner with

a spatial resolution of 4.8 mm FWHM, whereas the present work used the GE Signa PET/MR scanner with a spatial resolution of 4.3 mm FWHM. Also, the previous work corrected for the scattered and random events before the reconstruction, whereas this current work incorporated all corrections (attenuation, normalisation, scatter and randoms) in the reconstruction, as in the state-of-the-art reconstruction algorithms.

Therefore, one of the aims of this investigation is to evaluate the partial volume effect in lesions close to a high activity region, and also to investigate how much this is dependent on spill over activity from the adjacent region, lesion-to-hot region distance, lesion size, spatial resolution, degree of post-filtering, and scatter effect. The background correction would then be implemented and its performance evaluated in terms of lesions' quantification accuracy and contrast, using both simulated and real clinical PET/MR data.

3.2 Materials and Methods

3.2.1 Datasets and PET/MR System

Two datasets were primarily used in this study: (i) simulated data from digital XCAT2 phantom (Segars et al. [2010]) and (ii) experimental data from a NEMA IQ phantom (Ziegler et al. [2015]). Additionally, a patient abdominal scan was used for further validation. These datasets are shown in Figure 3.1.

The experimental studies were acquired using the GE Signa PET/MR scanner at Invicro, with 25 cm axial FoV, 60 cm transaxial FoV, 70 cm ring diameter, 25 $\times$ 4.0 $\times$ 5.3 crystal size in mm, and energy resolution of 10.5% with an energy window 425 – 650 keV (Grant et al. [2016]). The simulation was performed using

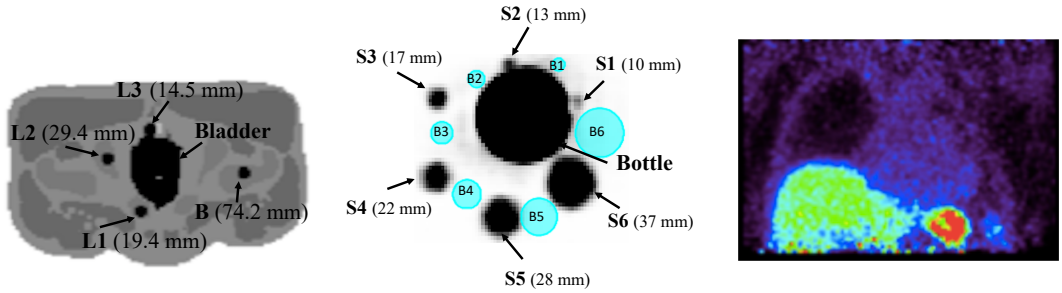

Figure 3.1: The datasets used for this study: (a) simulation from XCAT2 phantom consisting of the bladder, 3 lesions (L1 - L3) and 1 background lesion (B) placed at different distances (shown in brackets) from the bladder; (b) NEMA phantom consisting of a hot bottle at the centre, surrounded by 6 spheres (S1 - S6) with diameters shown in brackets. The blue spheres (B1 - B6) were used to estimate the background activity for the estimation of CNR; (c) patient data showing high activity in the spleen and liver.

an analytical model of the same scanner.

3.2.2 Simulations

The pelvic region was simulated using digital XCAT2 phantom with a typical [^{18}F]-FDG distribution. Hot bladder was simulated with a fixed volume (500 ml) and various activities (i.e. SUVs 8.5, 19.3, 33.8 and 55.5) allocated as obtained from the literature (Park et al. [2007], Pelosi et al. [2011]). This is to mimic the progressive increase in bladder activity due to the radiotracer accumulation during a typical PET examination. Three lesions labelled L1, L2, L3 each with diameter 10 mm and fixed activity value (SUV 8) were placed at different locations around the bladder as shown in Figure 3.1a. An increase in bladder volume and activity during a typical 90 minutes scan was also simulated using extracted values from the literature (Lee and Kim [2008], Puri et al. [2017]) at time points 1, 10, 30, 45 and 90 minutes. This was done to investigate the spill in effect

from the bladder to the surrounding lesions as a function of increasing bladder volume, bladder activity and lesion distance from the bladder. Additionally, lesion diameters ranging from 6 mm to 12 mm with a step size of 2 mm were simulated for all bladder SUVs to investigate the spill in effect as a function of lesion size. For each lesion diameter, same sized background lesion (B) was also added farther from the bladder such that the background lesion is not affected by the spill in effect from the bladder. This was done to distinguish between spill in and spill out effects as it affects lesion quantification, especially for small lesions. The emission and attenuation images were generated for each of these bladder and lesions combinations.

Fully 3D analytical simulation was done using the STIR package (Thielemans et al. [2012]), considering all sinograms with ring difference less than or equal to 44, and span 1. To approximate the blurring effect from the scanner, the simulated images were first convolved with a Gaussian filter having FWHM as that of GE PET/MR PSF (4.2 mm and 5.7 mm FWHM in transverse and axial planes respectively (Levin et al. [2016])) at the forward projection stage. The forward projector used is based on Siddon's ray tracing algorithm (Siddon [1985]), tracing 10 tangential rays for each bin. ACFs were calculated from the attenuation image and this was used to attenuate the emission sinogram. Constant normalisation and randoms sinograms were also generated, with the random counts making up to 20% of the total projection data. Scatter was estimated analytically using the SSS approach (Watson et al. [1996]) as incorporated into STIR (Tsoumpas et al. [2004]). A scaling factor was applied to make the scatter count 35% of the total simulated events. The random and scatter sinograms were used to generate the additive term, while the attenuation and normalisation sinograms were used as

multiplicative terms. time of flight (TOF) was not simulated for this study.

Poisson noise was added to the sinograms to simulate 65×106 counts (which corresponds to approximately 5 minutes of PET scanning), and 20 noise realisations were performed for statistical analysis. Spherical ROIs equal in diameter to the size of the lesions were placed in the position of each lesion in order to extract the uptake values (SUV_{mean} and SUV_{max}) for each noise realisation. The mean ($\bar{M}$), standard error of the mean (SEM), and bias (B) from all the 20 realisations (as defined in Equations 3.1) were used as figures of merit to show the differences in SUV values for both uncorrected and corrected images.

$$\bar{M} = \frac{1}{N}\sum_{i=1}^{N} f_i \tag{3.1a}$$

$$SEM = \frac{SD}{\sqrt{N}} \tag{3.1b}$$

$$where\ SD = \sqrt{\frac{1}{N-1}\sum_{i=1}^{N}(f_i - \bar{M})^2} \tag{3.1c}$$

$$B(\%) = \frac{\bar{M} - T}{T} \times 100 \tag{3.1d}$$

where f_i is the SUV from a single noise realisation, N is the total number of noise realisations (=20) and T is the SUV of the true simulated image.

The % change in lesion (l) SUV (ΔSUV_l) as the bladder SUV increases from SUV 8.5 to SUV 55.5 was also estimated using:

$$\Delta SUV_l(\%) = \frac{SUV_l\ (55.5) - SUV_l\ (8.5)}{SUV_l\ (8.5)} \times 100 \tag{3.2}$$

where SUV_l (8.5) and SUV_l (55.5) represent the lesion SUV at bladder SUVs 8.5 and 55.5, respectively.

To further investigate the spill in effect from the bladder to the surroundings, shells of different voxels (from 2 to 10 voxels with a step size of 2 voxels) was created around the bladder by performing a morphological operation on the bladder mask to obtain the edge mask:

$$edge\ mask = dilation(bladder\ mask, n) - bladder\ mask \tag{3.3}$$

where $dilation(bladder\ mask, n)$ means dilating the bladder mask by n voxels using a sphere structuring element in MATLAB.

The resulting edge mask was then used to extract the uptake values around the bladder in both true simulated and reconstructed mean images as illustrated in Figure 3.2a.

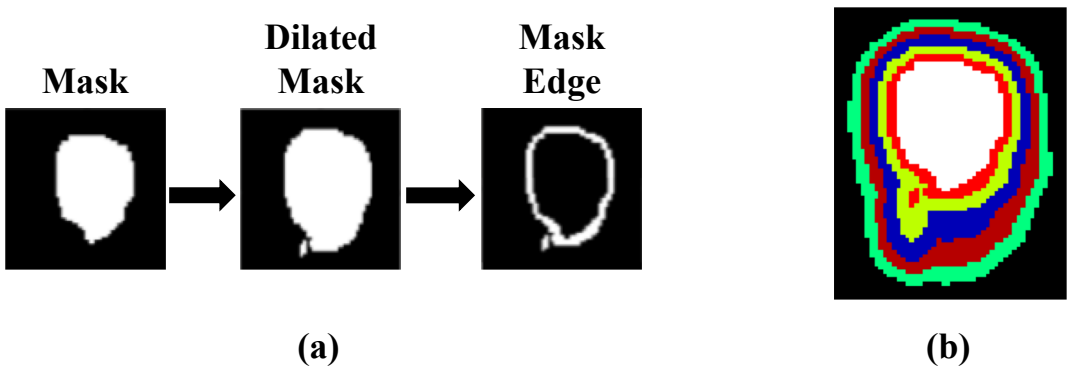

Figure 3.2: The schematic 2D representation of the technique used to extract the voxel values around the edges of the simulated bladder. (a) represents the procedure for extracting the voxel values, while (b) shows a 2D representation of all the dilated 3D regions around the bladder (i.e. the white region) from 2 voxels to 10 voxels with a step-size of 2 voxels.

3.2.3 Validation by Real Data

3.2.3.1 Experimental phantom

A phantom experiment was performed with the GE Signa PET/MR scanner at Invicro Ltd using the NEMA image quality (IQ) phantom without the wall (Figure 3.1b) (Ziegler et al. [2015]). This phantom consisted of 6 fillable spherical spheres S1 to S6 (with diameters 10, 13, 17, 22, 28 and 37 mm respectively, and filled with 5.38 MBq of [^{18}F]-FDG). A high activity 500 mL bottle (filled with 77.9 MBq of [^{18}F]-FDG), was placed at the centre of the phantom. The experimental set-up involved a simultaneous PET/MR acquisition with a 5 minutes static PET acquisition and 2-point Dixon MR 3D acquisition. List of events and singles rates for crystals were extracted from the listmode file from the scanner and these were converted to emission and random sinograms using STIR utility. The normalisation file was also extracted from the scanner and was converted to the normalisation sinogram using STIR. ACFs were obtained from the in-phase magnetic resonance attenuation correction (MRAC) image, and scatter was estimated using STIR. The CNR was used to evaluate the signal quality and noise properties of each reconstruction algorithm. This was done by estimating the mean activity and standard deviation in each sphere, as well as in pre-selected background spheres. The background spheres were represented as 6 spherical ROIs placed around the hot bottle which were exactly the same size as the spheres and located at approximately the same distance from the hot bottle (as shown in Figure 3.1b). So, the CNR was estimated for each sphere (i = 1, 2,

..., 6) using:

$$CNR_{sphere(i)} = \frac{Activity_{sphere(i)} - Activity_{background(i)}}{\sqrt{SD^2_{sphere(i)} - SD^2_{background\ (i)}}} \tag{3.4}$$

Also, the spill in activity from the bottle to the surroundings was estimated using the same morphological operation as in the simulation studies (shown in Equation 3.3).

3.2.3.2 Patient data

For further validation, patient data (Figure 3.1c) acquired with the General Electric (GE) PET/MR scanner at Invicro was used. This was acquired during a lung fibrosis examination using an [^{18}F]-based radiotracer. This data did not exhibit high activity in the bladder, but in the spleen and the liver. Thus, for demonstration purposes, the spleen was chosen as the background hot region. The patient data was reconstructed using the same settings as for the phantom experiment. The morphological dilation operation (in Equation 3.3) was also carried out on all reconstructed images so as to estimate the spill in effect around the hot region (spleen).

3.2.4 Data Reconstruction and Spill in Correction

Image reconstruction was done using the 3D iterative OSEM algorithm in STIR library. Attenuation, normalisation, random and scatter corrections were performed by including the multiplicative and additive terms in the reconstruction algorithm. For the simulation, 28 subsets and 30 full iterations were used to ensure reasonable convergence of the recently proposed correction algorithm.

Meanwhile for the real data, fully 3D reconstruction with mixed span factors according to GE's configuration (span 1 for $|RD| > 1$; and span 3 for RD = -1,0,1) was done using OSEM with 28 subsets and 20 full iterations, incorporating all corrections within the reconstruction. The reconstructed images have 256 × 256 × 89 voxels with size 2.34 × 2.34 × 2.78 mm^3, and they were post-filtered with a 4 mm isotropic 3D Gaussian filter. spill in correction was done using the two techniques as outlined below:

(a) PSF Reconstruction

This involves incorporating a spatially-invariant PSF into the OSEM reconstruction in both forward and backward projections as illustrated in Equation (3.5). This PSF was specified as a 3D Gaussian filter with 4.2 mm and 5.7 mm FWHM in transverse and axial planes respectively, according to experimental values obtained for the GE PET/MR scanner (Levin et al. [2016]).

$$H_{ij} = \sum_k H_{kj} PSF_{ik} \tag{3.5}$$

where H_{kj} represents the system matrix, and H_{ij} is the system matrix convolved with the system PSF in both forward and back projections (Rapisarda et al. [2010], Rogasch et al. [2014]). This reconstruction method is referred to as OSEM+PSF in this study.

(b) Background Correction (BC)

The background correction was implemented as discussed in Chapter 2. For the simulation, the bladder (hot region) was automatically segmented from the XCAT2 phantom to obtain the bladder mask S_j. This was then multiplied by the OSEM+PSF reconstructed image $f_j^{(N)}$ (taken at five iterations) to obtain the

bladder contribution in the image (i.e. $B_j = S_j f_j^{(N)}$, which was then forward-projected using the same projection matrix for the simulation ($P_i = \sum_j H_{ij} B_j$) and included in the reconstruction as a background term along with the additive term (as shown in Equation 3.6). For the real data, the highly radioactive bottle that accompanied the NEMA phantom, and the hot spleen of the patient were segmented from the Dixon in-phase MRAC image before forward-projecting it to obtain the background contribution.

$$f_j^{(n+1)} = \frac{f_j^{(n)}}{\sum_i H_{ij}} \sum_i H_{ij} \frac{y_i}{\sum_k H_{ik} f_k^{(n)} + A_i + P_i} \tag{3.6}$$

where $f_j^{(n)}$ is the uncorrected image, y_i is the emission sinogram, H_{ij} is the system matrix with the PSF, A_i is the additive term, P_i is the bladder background term, and $f_j^{(n+1)}$ is the final corrected image without the bladder contribution. The flow sequence is shown in Figure 3.3. Since this technique also includes OSEM+PSF, it will be referred to as OSEM+PSF+BC in this study.

It is worth noting that the BC reconstruction technique is the same as the standard OSEM reconstruction, where a uniform image is used as the initial estimate. The only difference is that in the BC technique, the additive sinogram term now consists of an extra component to account for the background contribution in addition to randoms and scatter.

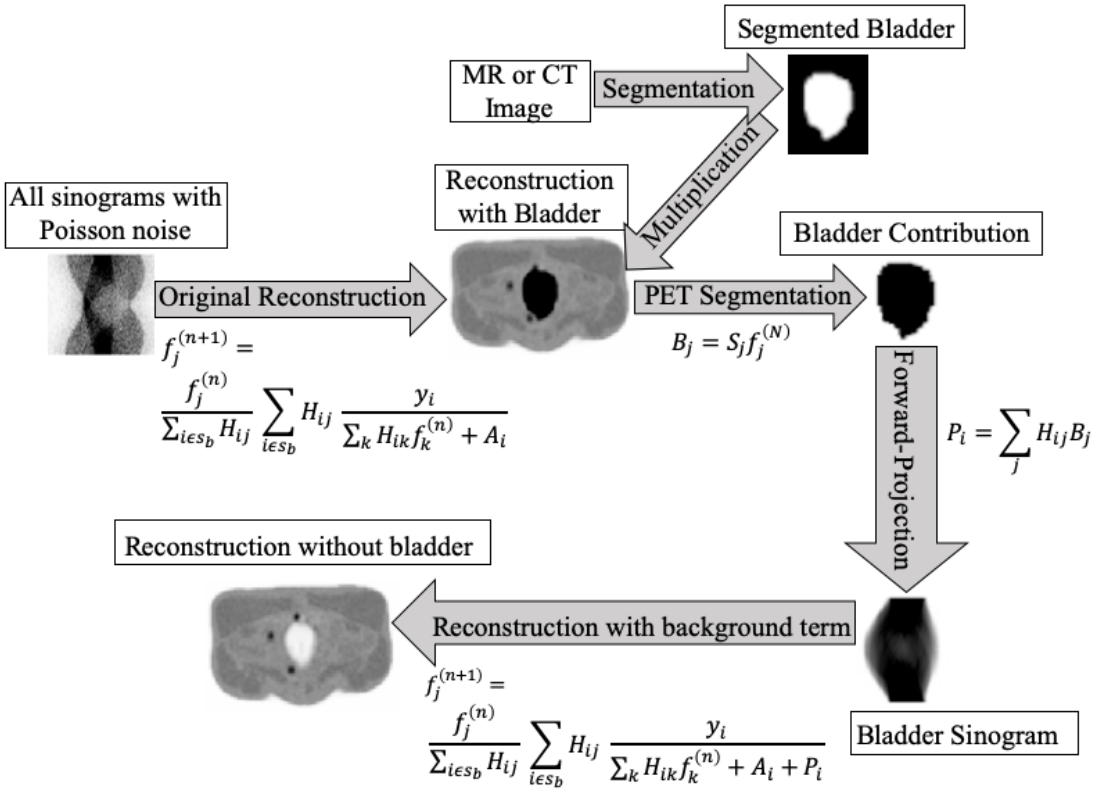

Figure 3.3: Schematic description of the background correction technique, as demonstrated for the XCAT2 phantom simulation. In this study, the bladder was automatically segmented from the XCAT2 phantom, but in principle, the hot region can be segmented from either the CT or MR image.

3.3 Results

3.3.1 Simulations

3.3.1.1 Convergence property of the reconstruction algorithms

For the convergence plot, the mean SUV_{mean} and SUV_{max} of the simulated lesions (L1, L2, L3) for bladder (SUV: 8.5 and 55.5) were estimated using the SUVs of the 20 noise realisations with 4 mm isotropic 3D Gaussian filter. The result is

shown in Figure 3.4.

Each reconstruction algorithm, as well as each simulated lesion, seems to have slightly different convergence rates. Therefore, for SUV analysis in this study, the iteration number was increased to 30 so as to ensure a reasonable convergence of all algorithms and lesions. OSEM+PSF reconstruction has a higher SUV comparative with OSEM reconstruction both for SUV_{mean} and SUV_{max}. This has been a commonly reported behaviour associated with the incorporation of PSF into the reconstruction Rapisarda et al. [2010], Rogasch et al. [2014]. For L3 at bladder SUV 55.5, OSEM and OSEM+PSF have higher SUVs at early iterations, but this reduces as the number of iteration increases. This might signify that for proximal lesions to hot regions, the spill in effect reduces with iteration. However, OSEM+PSF+BC has similar behaviour at both bladder SUV 8.5 and SUV 55.5.

3.3.1.2 Investigating the spill in effect as a function of bladder activity, lesion size and postfilter using OSEM reconstruction

Figure 3.5 shows the mean lesion SUV_{max} and SUV_{mean} for OSEM reconstruction at 30 full iterations. As the bladder SUV increases, the lesion SUV_{max} also increases for all lesions, with the highest SUV in L3. However, SUV_{mean} increases only for L3. The % bias and the % change in lesion SUV as the bladder SUV increases from SUV 8.5 to SUV 55.5 (using Equation 3.2) are presented in Table 3.1.

For lesion L3, the % bias in SUV increases as the bladder SUV increases, and this is more pronounced for SUV_{max} than SUV_{mean}. However, for lesions L1 and L2, only SUV_{max} has an increased % bias as the bladder SUV increases,

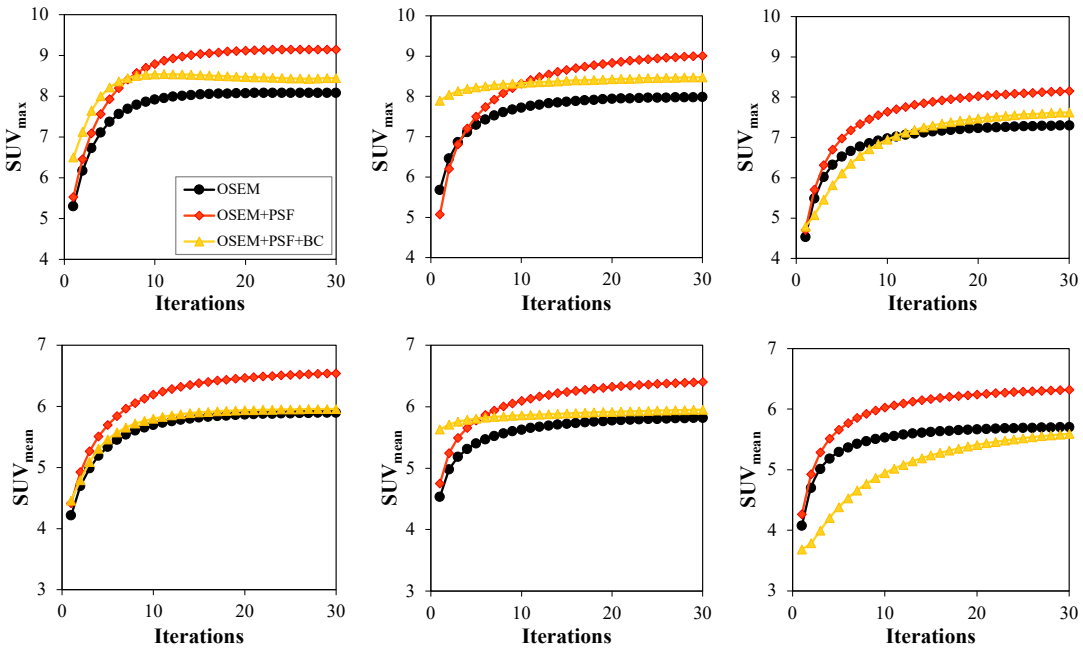

(a)

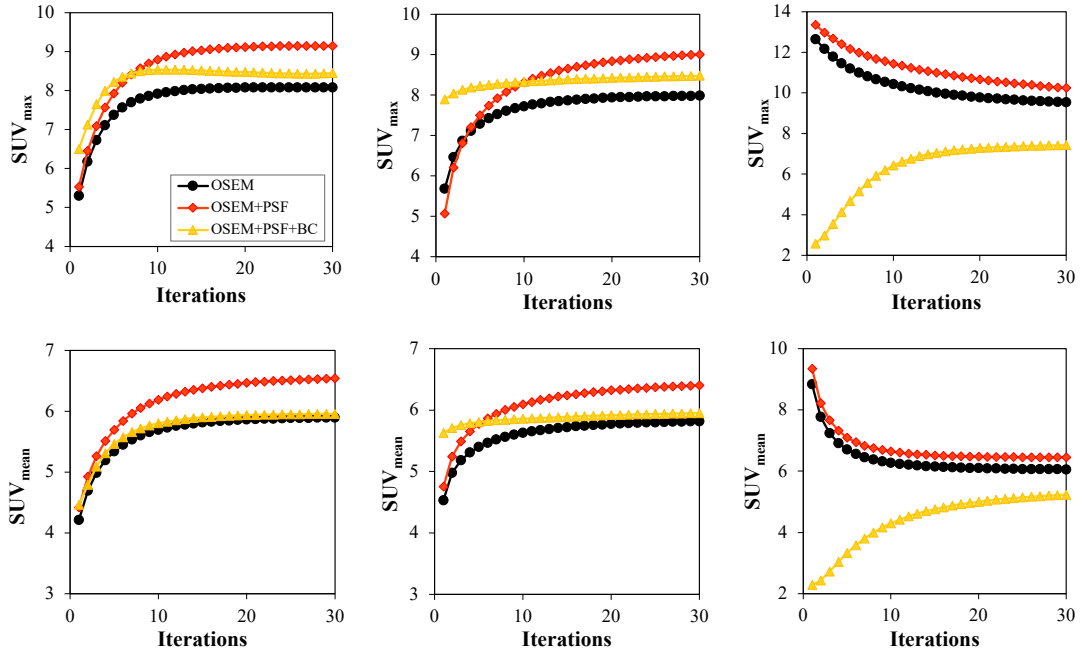

(b)

Figure 3.4: Convergence plots of all the reconstruction algorithms using lesion SUV_{max} and SUV_{mean}. This is estimated for lesion diameter 10 mm at (a) bladder SUV 8.5 and (b) bladder 55.5, and it is obtained from the mean of all 20 noise realisations with 4 mm Gaussian post-filter. First, second and third columns represent the convergence plots for lesions L1, L2 and L3 respectively (each with true SUV: 8).

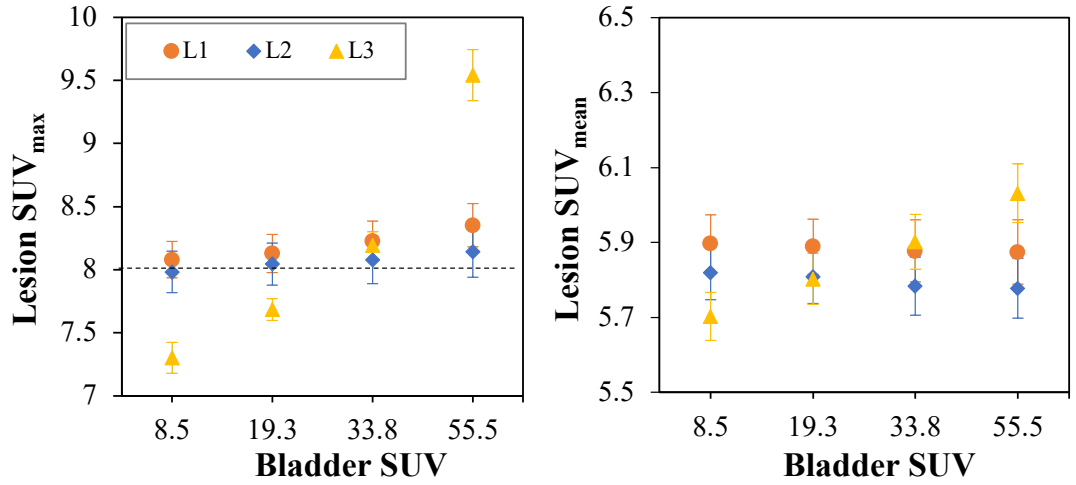

Figure 3.5: The lesion uptake as the bladder SUV increases for images reconstructed with OSEM. These are the mean SUVs from all the 20 noise realisations and for lesion diameter 10 mm at 30 full iterations. The error bars are the standard error of the mean (SEM) while the dashed horizontal line denotes the true simulated lesion SUV.

Table 3.1: The bias and relative change in lesion SUV_{max} and SUV_{mean} for all the simulated bladder SUVs and for lesion diameter 10 mm. These are estimated from the mean SUVs from all the noise realisations. (The % bias values are given in parentheses).

Bladder SUV	Simulated Lesions					
	L1		L2		L3	
	SUV_{max}	SUV_{mean}	SUV_{max}	SUV_{mean}	SUV_{max}	SUV_{mean}
SUV 8.5	8.08 (1.00)	5.90 (-26.28)	7.98 (-0.21)	5.82 (-27.27)	7.30 (-8.72)	5.70 (-28.72)
SUV 19.3	8.13 (1.61)	5.89 (-26.39)	8.05 (0.57)	5.81 (-27.39)	7.68 (-3.95)	5.80 (-27.47)
SUV 33.8	8.23 (2.82)	5.88 (-26.53)	8.08 (0.97)	5.78 (-27.71)	8.19 (2.41)	5.90 (-26.23)
SUV 55.5	8.35 (4.41)	5.87 (-26.57)	8.14 (1.78)	5.78 (-27.78)	9.54 (19.27)	6.03 (-24.61)
% Change	3.37	-0.39	1.99	-0.7	30.67	5.77

SUV_{mean} seems constant. At bladder SUV 55.5, SUV_{max} of lesion L3 (closest to the bladder) has a % bias of 19.3% while for L2 (further away), the % bias in SUV_{max} is only 1.8%. As bladder SUV increases from 8.5 to 55.5, the % SUV change for L3 is 30.67% and 5.77% for SUV_{max} and SUV_{mean} respectively, while the % change in SUV_{max} is less than 4% for lesions L1 and L2.

Figure 3.6 shows the spill in and spill out effects on lesion quantification as a function of lesion size. This is shown for lesions L1-L3 and background lesion B at bladder SUV 55.5. As expected, the spill out effect from the lesions to the colder background causes an underestimation in lesion SUV for small diameter lesions, but the SUV increases as the diameter increases. However, the lesion SUV is further influenced by spill in effect from the bladder to the lesions, and this depends on the lesion distance. Lesion L3, which is the closest lesion to the bladder, has the highest SUVs while lesion L2, which is farther away, has the least.

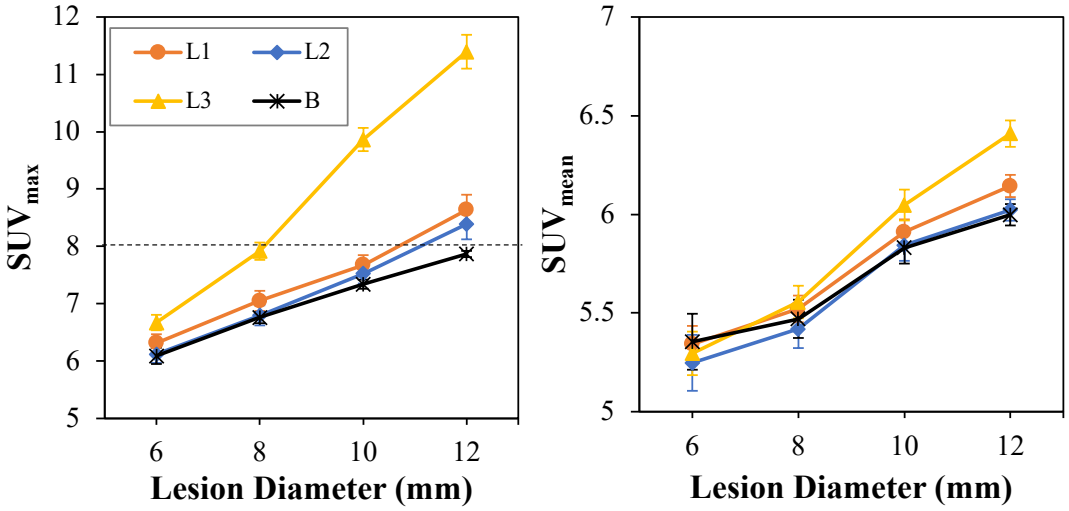

Figure 3.6: The spill in and spill out effects as a function of lesion size for lesions L1-L3 and background lesion B at bladder SUV 55.5. The SUVs were obtained from OSEM reconstructed images using the mean SUVs of all noise realisations at 30 full iterations with 4 mm Gaussian post-filter. The error bars are the standard error of the mean (SEM) while the dashed horizontal line denotes the true simulated lesion SUV. Background lesion B is the reference which shows the expected lesion SUV without spill in effect.

The relationship between the spill in effect (due to increasing bladder activity) and lesion size is further shown in Table 3.2. For a fixed diameter, the lesion

SUV increases with bladder activity, thereby increasing the bias. This is not so evident in L1 and L2.

Table 3.2: The effect of increasing bladder SUV on lesion quantification for each lesion diameter. This is expressed as the % change in lesion SUV as bladder SUV increases. The SUV values are the mean values from all noise realisations at 30 full iterations with 4 mm postfilter.

Lesion Diameter (mm)	Relative Change in Lesion SUV					
	L1		L2		L3	
	SUV_{max}	SUV_{mean}	SUV_{max}	SUV_{mean}	SUV_{max}	SUV_{mean}
6	1.67	0.31	1.89	0.51	10.94	3.90
8	3.08	0.45	1.41	0.85	15.09	4.90
10	3.37	0.39	1.99	0.70	30.67	5.77
12	4.96	0.33	2.07	0.99	53.53	8.50

The % relative change in lesion SUV is further influenced by the application of post-filter as shown in Figure 3.7. Lesion L3 showed the highest % relative change in SUV (both SUV_{mean} and SUV_{max}) as post-filter FWHM increases, and with 5 mm post-filter, this relative change was as much as 49% and 9% for SUV_{max} and SUV_{mean} respectively. L1 showed a slight relative change but L2 showed no defined relative change in SUV.

To further investigate the spill in effect as a function of the system resolution, instead of blurring the simulated PET images with the GE Signa PSF, the images were blurred with an isotropic Gaussian filter of FWHM ranging from 3 – 6 mm before forward projection. Figure 3.8 shows the estimated spill in activity around the dilated bladder shells as resolution increases (using Equation 3.3). The spill in activity is expressed as the % activity difference in the dilated shells between the simulated and OSEM reconstructed images.

FWHM of 6 mm has the highest % activity difference, and this reduces significantly as resolution improves, with FWHM of 3 mm having the least % activity

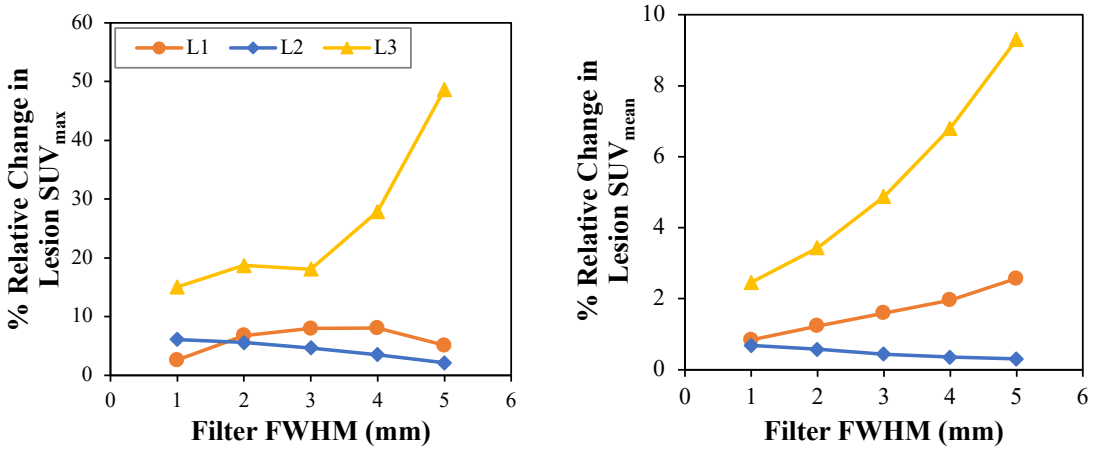

Figure 3.7: The dependence of spill in effect on post-filter. This was done with a single noise realisation at 30 iterations.

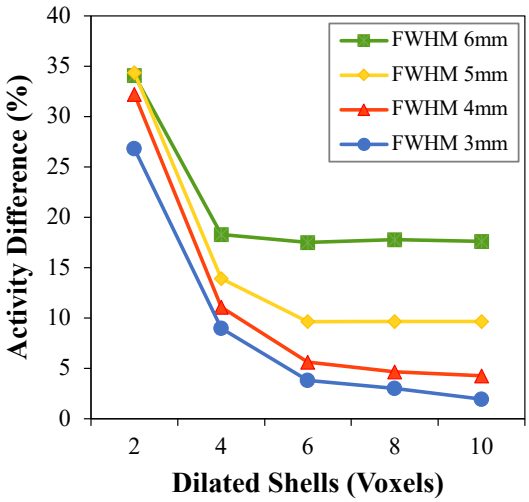

Figure 3.8: The spill in activity from the bladder to the surroundings as a function of the system resolution (in FWHM), using Equation 3.3. The activity difference is estimated from a single noise realisation of OSEM reconstruction with bladder SUV 55.5 at 30 full iteration with 4 mm post-filter.

difference. Also, as expected, the immediate shell around the bladder (2 voxels) has the highest activity difference for all resolutions, but it reduces as it moves

further away. However, for FWHM of 5 and 6 mm, the activity difference remains almost constant and considerably high even at voxels 6 to 10 away from the bladder.

3.3.1.3 Effect of correction techniques on reduction of spill in effect

Figure 3.9 shows how the lesion SUV changes iteratively for all reconstruction techniques as bladder SUV increases from SUV 8.5 to SUV 55.5. This shows that % change in lesion SUV reduces as iteration increases. At 30 iterations, the % change in lesion SUV_{max} is about 31%, 26%, and 4% for OSEM, OSEM+PSF and OSEM+PSF+BC respectively, while for lesion SUV_{mean}, it is about 6%, 1% and -6% for OSEM, OSEM+PSF and OSEM+PSF+BC respectively.

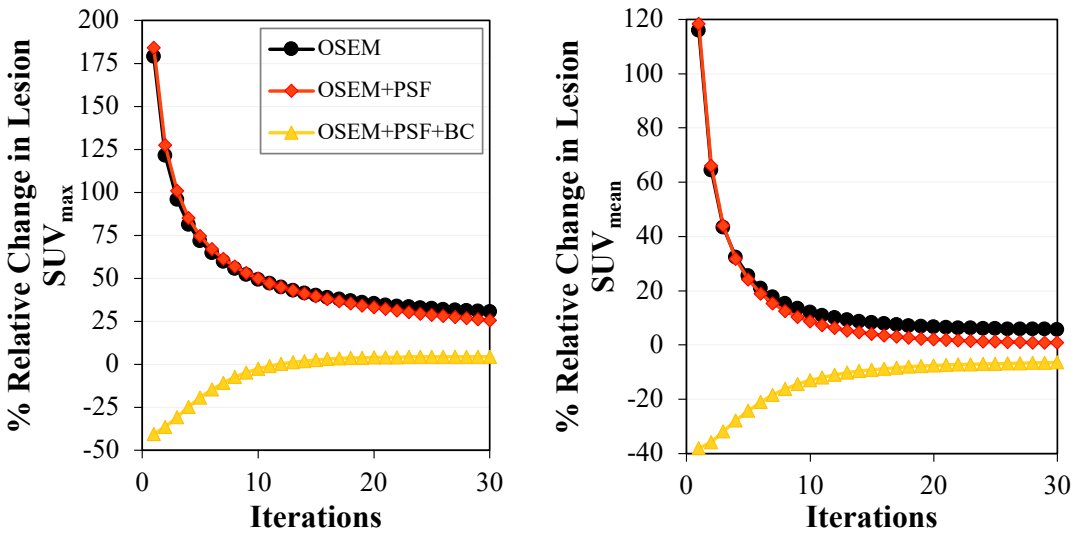

Figure 3.9: The % relative change in lesion SUV (as bladder SUV increases from SUV 8.5 to SUV 55.5) as a function of increasing iteration. This is obtained from a single noise realisation and for lesion L3 of diameter 10 mm with 4 mm Gaussian post-filter.

Table 3.3 shows the estimated spill in activity from the bladder to the surrounding regions for both uncorrected and corrected images at 30 full iterations

with and without post-filtering. This is the percentage activity difference in the dilated shells between the true simulated image and the reconstructed image.

Table 3.3: Estimation of the spill in activity from the bladder to the surrounding regions. This is estimated from both filtered and unfiltered mean images with simulated bladder SUV 55.5 at 30 iterations (the filtered results are given in parentheses). $\bar{d}$ is the difference between the mean values of the true simulated and reconstructed images for all voxels in the dilated region. LOA is the 95% Limit of Agreement of $\bar{d}$, with showing the upper and lower limits.

Dilated Regions (voxels)		OSEM	OSEM+PSF	OSEM+PSF+BC
1 – 2	% Difference (d)	31.5 (41.8)	18.7 (30.8)	3.3 (1.6)
	SD[1]	26.4 (28.4)	25.0 (30.2)	15.4 (11.7)
	LOA[2]	-20.3 to +83.3	-30.4 to +67.8	-26.9 to +33.5
		(-13.9 to +97.6)	(-28.4 to +89.9)	(-21.4 to +24.6)
3 – 4	% Difference ($\bar{d}$)	9.3 (8.5)	2.6 (2.7)	4.7 (3.9)
	SD	10.6 (9.5)	8.0 (8.9)	10.0 (8.8)
	LOA	-11.4 to +30.0	-13.1 to +18.4	-15.0 to +24.3
		(-10.1 to +27.0)	(-14.7 to +20.1)	(-13.4 to +21.2)
5 – 6	% Difference ($\bar{d}$)	5.4 (6.4)	2.4 (3.6)	1.3 (2.5)
	SD	12.9 (7.8)	8.7 (6.7)	10.9 (8.3)
	LOA	-19.9 to +30.7	-14.8 to +19.5	-20.0 to +22.7
		(-8.8 to +21.6)	(-9.5 to +16.7)	(-13.8 to +18.8)
7 – 8	% Difference ($\bar{d}$)	4.0 (4.3)	1.6 (2.0)	1.4 (1.6)
	SD	12.8 (7.9)	8.9 (7.1)	11.2 (8.3)
	LOA	-21.1 to +29.9	-16.0 to +19.1	-20.4 to +23.3
		(-11.2 to +19.8)	(-12.0 to +15.9)	(-14.6 to +17.9)
9 – 10	% Difference ($\bar{d}$)	2.8 (3.4)	0.6 (1.5)	0.5 (1.3)
	SD	11.6 (7.0)	9.1 (6.4)	10.7 (7.4)
	LOA	-19.9 to +25.5	-17.2 to +18.4	-20.4 to +21. 3
		(-10.2 to +17.1)	(-11.0 to +14.1)	(-13.1 to +15.8)

There is a large spill in activity within 2 voxels around the bladder as the % activity difference between the simulated and reconstructed images is 31.5% (41.8%) for OSEM and 18.7% (30.8%) for OSEM+PSF reconstructions without and with post-filtering respectively. This shows that filtered images show increased spill in activity of about 33% and 65% for OSEM and OSEM+PSF respectively, compared with the unfiltered images. At 4 voxels around the bladder,

[1] $SD = \sqrt{\frac{1}{n-1}\sum_k = 1^n (d_k - \bar{d})^2}$, k represents each voxel in the dilated region

[2] LOA= $\bar{d} \pm$ 1.96SD

the activity difference around the bladder dropped greatly to 9.3% (8.5%) and 2.6% (2.7%), and at 10 voxels from the bladder, the activity difference is 2.8% (3.4%) and 0.6% (1.5%) for OSEM and OSEM+PSF, respectively. However, with the correction technique, the % activity difference is within 0.5% and 4.7% with and without post-filtering. It could be observed that OSEM has the highest upper limit of agreement (LOA), compared to OSEM+PSF and OSEM+PSF+BC. Also, the upper LOA for all methods reduces as we move voxels away from the bladder.

This spill in activity can also be seen around the bladder edges in the uncorrected images (as shown in Figure 3.10). This causes a bias around the bladder edges making the bladder appear bigger, hence affecting the visibility of nearby lesions.

3.3.1.4 Dependence of the background correction method on segmentation accuracy

To demonstrate the dependence of the recently proposed background correction method on segmentation accuracy, an increase in bladder volume and activity during a 90 minutes scan typical of PET/MR scan was simulated at time points 1, 10, 30, 45 and 90 minutes. Each image was reconstructed with background correction (OSEM+PSF+BC), but the segmented bladder mask at 1min timepoint was used for the correction in all cases. The resulting background corrected images are displayed in Figure 3.11.

This result shows that bladder expands majorly at the anterior superior end towards the rectum and the prostate. The error in segmentation is pronounced after 10 mins.

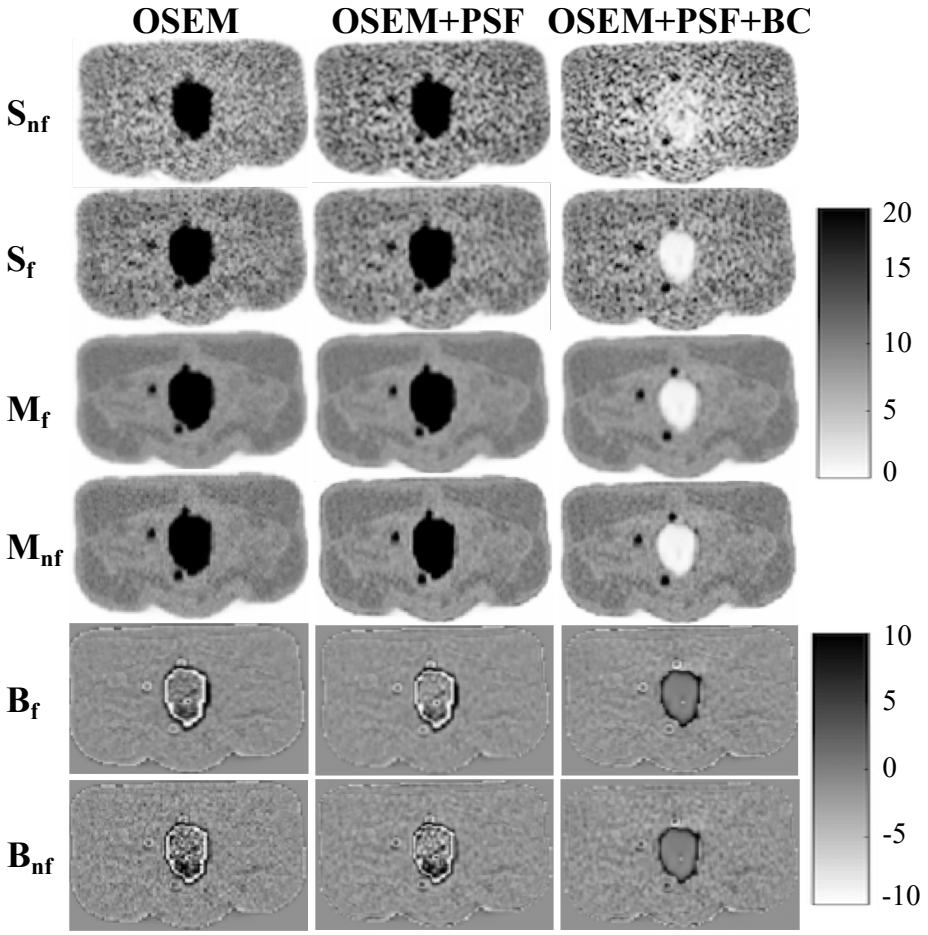

Figure 3.10: Images showing improvement in lesion detection and reduction of bias around bladder edges with the correction technique. This is shown for bladder SUV 55.5 and lesion diameter 10 mm at 30 full iterations. S_f and S_{nf} are the single noise realisation images with and without filtering respectively, while M_f and M_{nf} are the mean images from 20 noise realisations with and without filtering respectively. B_f and B_{nf} are the bias images (i.e. difference between the mean image and the true simulated image) with and without filtering respectively. The bias image in OSEM+PSF+BC was estimated by first removing the bladder from the true simulated image.

3.3.2 Validation by Phantom Experiment and Patient Data

Figure 3.12 shows the MRAC, segmented bottle and reconstructed images of the bottle phantom. OSEM+PSF+BC image shows improved visibility especially

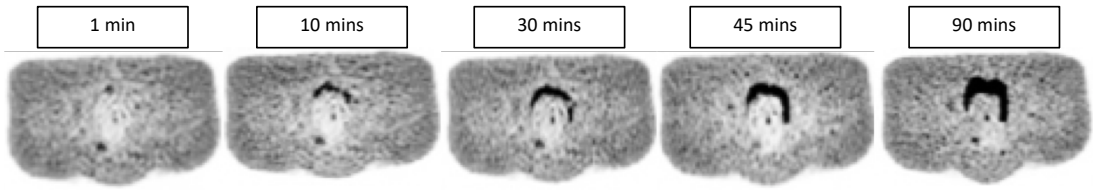

Figure 3.11: Demonstration of how inaccurate segmentation can limit the accuracy of the background correction technique. This is shown for a single noise realisation, with 4 mm postfilter. All images are displayed with the same maximum SUV threshold value 20.

for S1 and S2.

Figure 3.13 shows the CNR of all the spheres as a function of iteration. As expected, the CNR increases as the sphere diameter increases, but reduces with the number of iterations. OSEM and OSEM+PSF have almost the same CNR for all spheres, while OSEM+PSF+BC shows higher CNR than OSEM and OSEM+PSF for the two smallest spheres, and the ones closest to the bottle (S1 and S2). OSEM+PSF+BC does not show any clear improvement over OSEM and PSF for bigger spheres S3-S6.

Figure 3.14 shows the normalised mean activity in each of the dilated shells surrounding the hot NEMA bottle. Although the surrounding shells should have zero activity, the reconstructed images show a considerable amount of spill in activity from the hot bottle to the surrounding shells. Within 1 voxel around the hot region, the activity is about 75% and 90% of the activity in the sphere for OSEM; and 60% and 80% for OSEM+PSF, with and without post-filtering respectively. However, at 4 voxels, this activity is greatly reduced to just about 2% for OSEM and OSEM+PSF, either with or without post-filtering. However, for OSEM+PSF+BC, the activity is less than 3% in all cases, showing an improve-

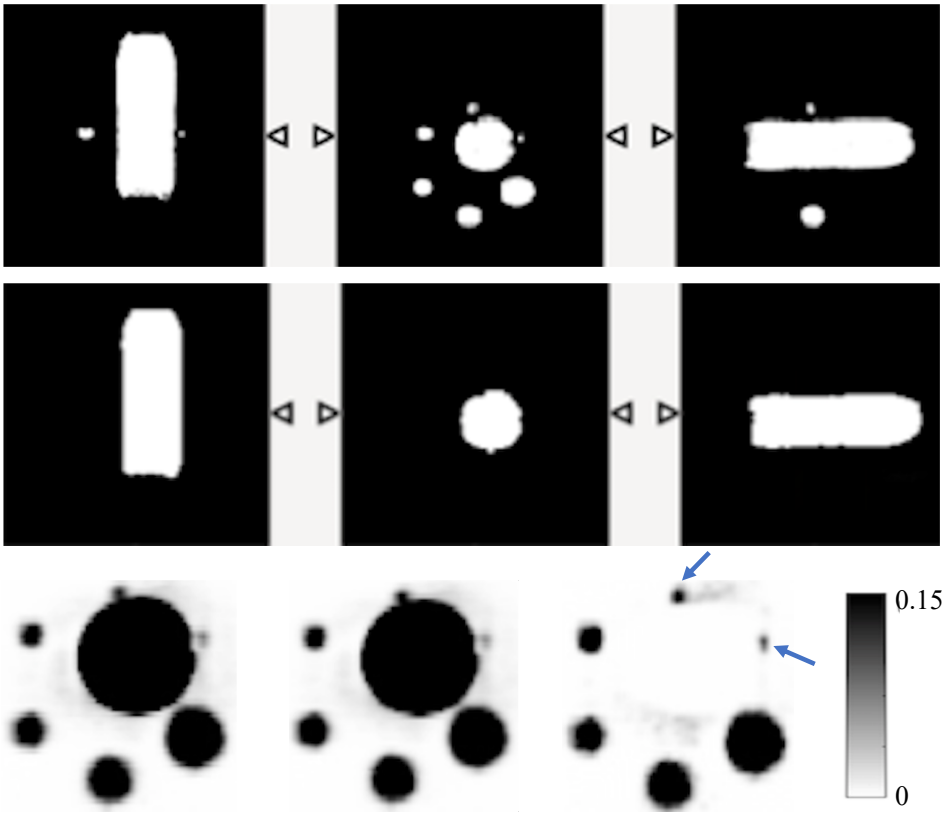

Figure 3.12: The NEMA bottle phantom used for the validation. The first row shows the MRAC image of the phantom; the middle row is the segmented bottle from the MRAC image; while the last row is showing the coronal view of the reconstructed images at 3 full iterations with 4 mm Gaussian filter for OSEM, OSEM+PSF and OSEM+PSF+BC reconstructions respectively. The blue arrows in the reconstructed images are pointing to the spheres in which there is visual improvement.

ment of more than 80% and 70% over OSEM and OSEM+PSF reconstructions respectively.

For the patient data, Figure 3.15 shows the normalised mean activity in the dilated shells around the spleen in all reconstructed images at 3 and 20 full iterations with and without post-filter. As expected, the mean activity in the dilated shells reduces as we move voxels away from the spleen, with the highest

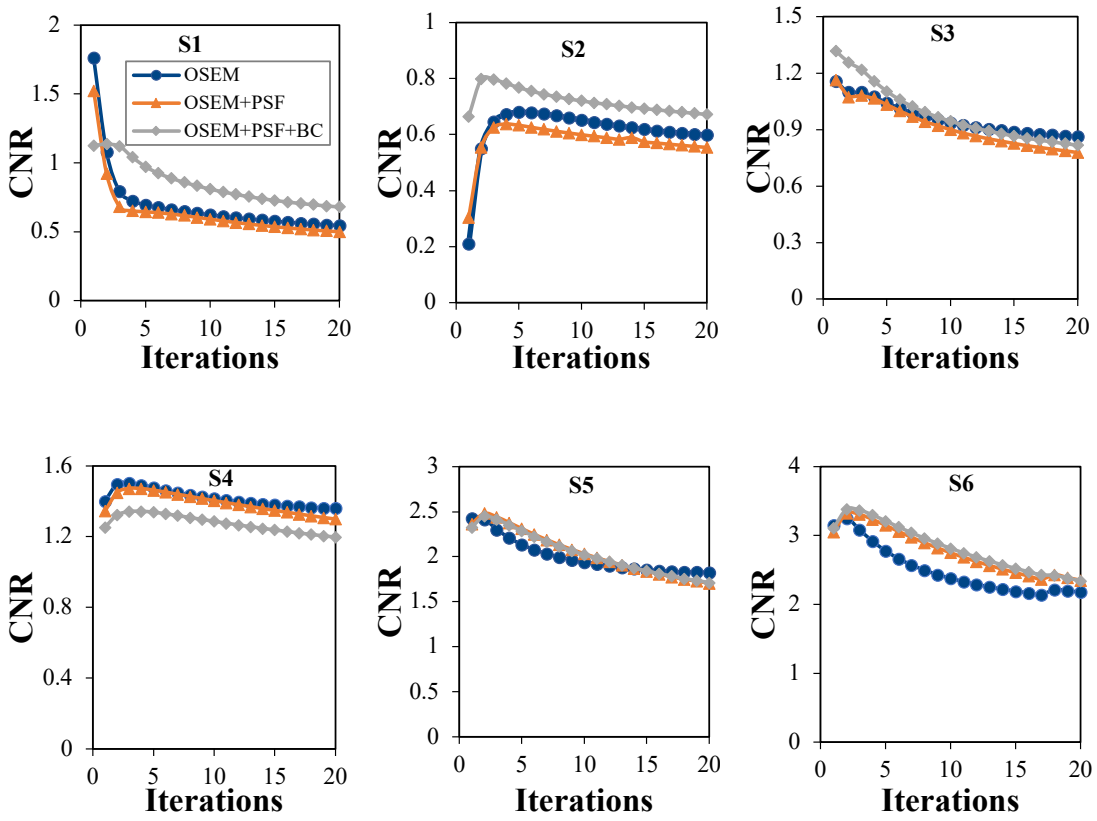

Figure 3.13: Plots of the CNR of the NEMA phantom spheres S1 - S6 against the iteration for all the reconstruction techniques across the 20 full iterations and without post-filtering. The CNR was estimated using the mean activity values in the spheres and background.

value at 1 voxel from the spleen in all cases. Also, increasing the number of iterations tends to reduce the activity in the dilated shell. For OSEM at voxel 1 and without post-filter, the mean activity is about 43% at 3 iterations but reduced to only 26% at iteration 20. However, with the application of post-filter, there is no pronounced difference in the voxel activities at 3 and 20 iterations. Also, OSEM+PSF has similar or even higher voxel activity than OSEM at 3 iterations with and without post-filter, but at 20 iterations, OSEM+PSF shows

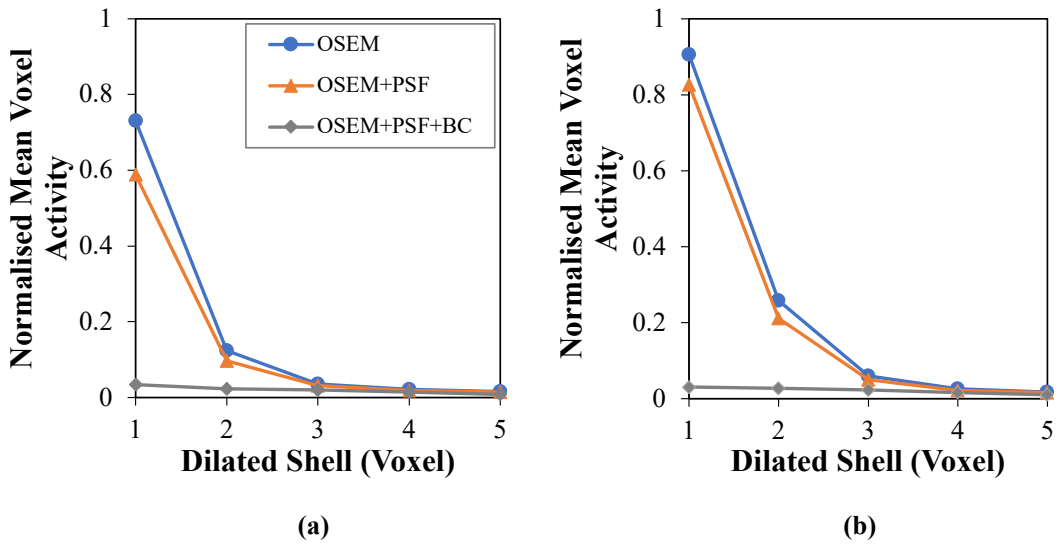

Figure 3.14: The normalised mean activity within the dilated shells surrounding the NEMA bottle obtained at 3 full iterations with (a) no postfilter and (b) 4 mm Gaussian postfilter. This demonstrates how spill in activity from the hot bottle to the surrounding shells reduces as we move further away from the bottle. The voxel activity were normalised with the actual activity in the spheres.

reduced voxel activity than OSEM. But in all cases, OSEM+PSF+BC has lower and almost constant voxel activity.

3.3.3 Investigating the Impact of TOF Reconstruction in Mitigating Spill in Effect

In order to explore the benefit of TOF reconstruction in correcting for spill in effect, the NEMA IQ phantom was reconstructed using the GE PET Toolbox with and without TOF implementation (with 28 subsets and 20 full iterations). The reconstructed images have 256 × 256 × 89 voxels with size 2.34 × 2.34 × 2.78 mm^3. The activity in the dilated shells surrounding the hot bottle was estimated using the morphological operation in Equation 3.3.

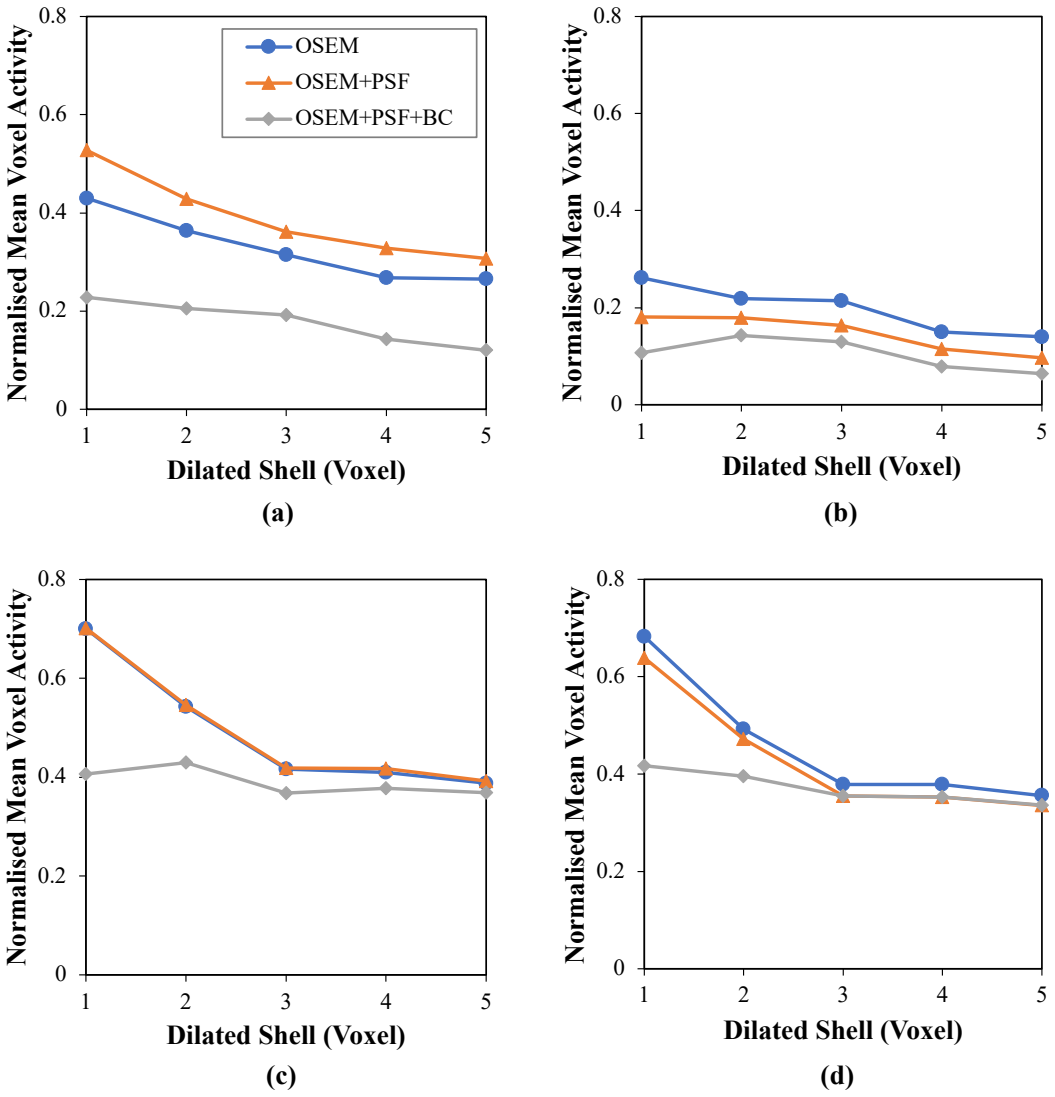

Figure 3.15: Validating the effect and correction of spill in effect using patient data. This figure shows the normalised mean values within the dilated shells surrounding the spleen at (a) 3 full iterations with no postfilter, (b) 20 full iterations with no postfilter, (c) 3 full iterations with 4 mm Gaussian postfilter, and (d) 20 full iterations with 4 mm Gaussian postfilter. The mean activity values in the dilated shells were normalised with the mean activity in the liver.

Figure 3.16 shows the normalised mean activity in each of the dilated shells surrounding the hot NEMA bottle, for TOF and non-TOF reconstructions. At

3 iterations, there is a slight improvement of TOF reconstruction over non-TOF reconstruction for 2 voxels around the bottle, however, at 20 iterations, the improvement is only seen at 1 voxel.

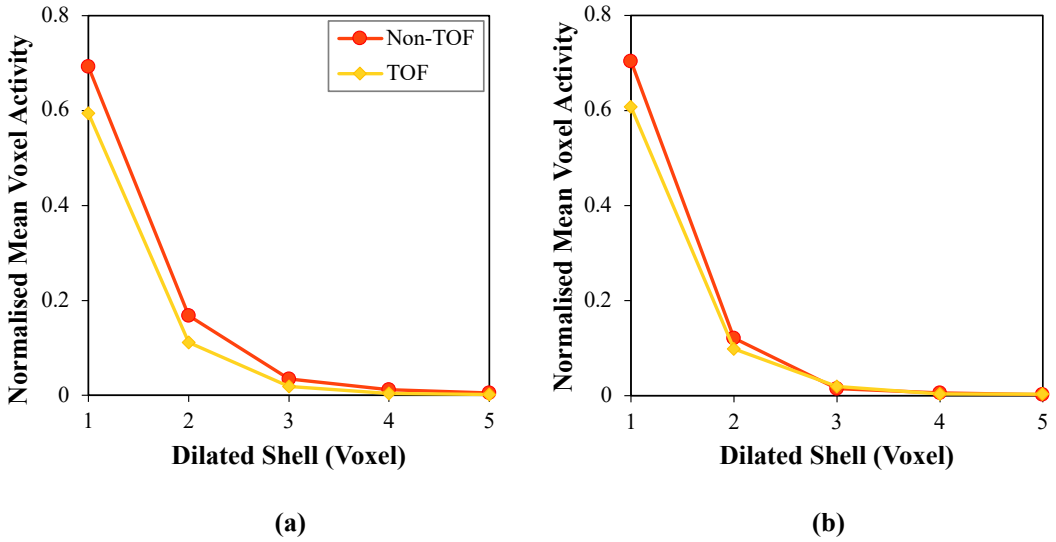

Figure 3.16: The normalised mean values within the dilated shells surrounding the NEMA bottle obtained at with (a) 3 iterations and (b) 20 iterations., with non-TOF and TOF reconstructions. The reconstructions were done with the GE PET toolbox. The voxel activity were normalised with the actual activity in the spheres.

It is worthy of note that at 2 voxels, the spill in activity in non-TOF image is up to 17% at 3 iterations, but only 12% at 20 iterations. This also reiterates the fact that SUV overestimation as a result of spill in effect reduces over iteration. Therefore, in order to reduce the spill in effect, slightly increasing the number of iterations might be a good alternative. However, this will be at the expense of reduced CNR and increased noise. For the NEMA bottle phantom, the spill in activity from the hot bottle to the surrounding shells reduces as we move further away from the bottle, and this is lower for TOF reconstruction than non-TOF. Similar trend is also seen in the patient data (Figure 3.17), but major

improvement with TOF reconstruction over non-TOF reconstruction in terms of reduced spill in effect around the segmented spleen is visible only at higher iterations.

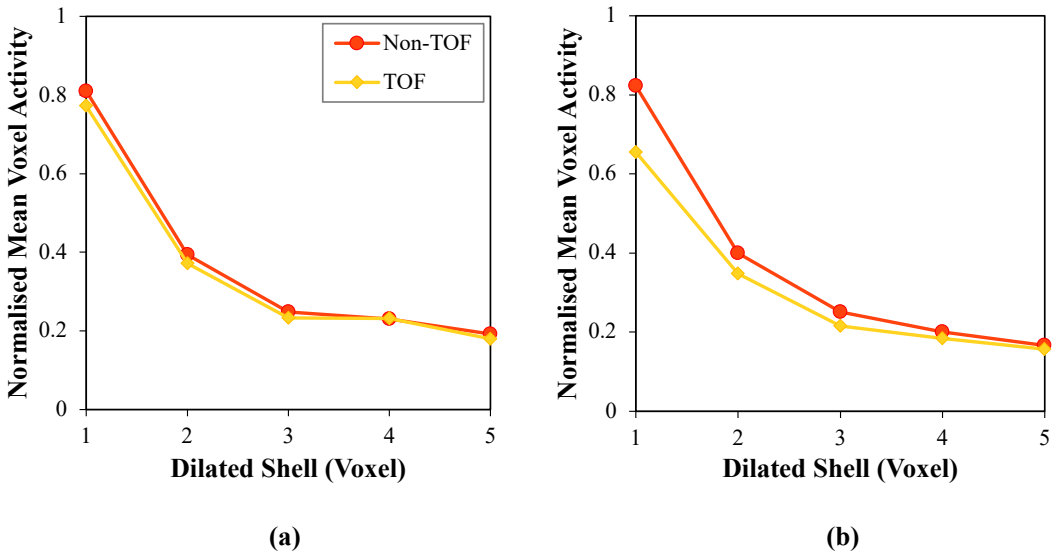

Figure 3.17: Normalised mean values within the dilated shells surrounding the spleen obtained with non-TOF and TOF reconstructions at (a) 3 iterations and (b) 20 iterations. The reconstructions were done with the GE PET toolbox. The voxel activity was normalised with the mean activity in the liver.

3.4 Discussion

An extensive investigation has been carried out with simulated and experimental phantoms on the full suppression of the spill in effect from background hot regions to the surrounding lesions as a function of increasing background activity, lesion size, and distance to the background, using the background correction technique (Silva-Rodriguez et al. [2016]).

The simulation results show that lesion uptake increases as bladder activity

increases (Figure 3.5) and this could be attributed to bladder accumulation, thereby causing spill in effects (Liu [2012]). L3 closest to the bladder has the highest change in SUV, while L1 and L2 further away have less SUV variation. This indicates that there is a high probability of SUV overestimation in lesions close to the bladder, and hence they suffer greatly from the spill in effect (Kolb et al. [2015], Puri et al. [2017]). A similar experiment was conducted by Liu [2012] and he concluded that if the lesions are within 40 - 50 mm from the hot source, the estimated SUV values are overestimated and therefore invalid. However, for our study, this SUV overestimation is only experienced in lesions within 15 - 20 mm from the bladder. This improved result may be due to the improved resolution of the simulated GE PET/MR scanner, which makes the effect less prominent (as seen in Figure 3.8).

It was also discovered that the spill in effect seems to increase with lesion size, and this is more evident in proximal lesions to the bladder (Figure 3.6). As expected, spill out effect from the lesions to the background causes an underestimation in lesion SUV for small diameter lesions, but the SUV increases as the diameter increases. However, the lesion SUV is further influenced by spill in effect from the bladder to the lesions, and this is dependent on the lesion distance. Lesion L3 which is the closest lesion to the bladder has the highest bias in SUVs while the background lesion has the least. For lesion L3, the spill in effect seems to increase with lesion diameter. This is because smaller lesions suffer from both spill out effect to the colder region and spill in effect from the hot background region. These two effects might sometimes cancel out, thereby giving a false impression of quantification accuracy in smaller lesions (as depicted in our study). However, for bigger lesions close to the bladder, spill in effect is

the major effect, thereby leading to a pronounced overestimation in SUV. For lesions L1 and L2 however, the impact of spill in effect on SUV quantification is small, and only evident for SUV_{max} (Details in Table 3.2). This also re-iterates the strong dependence of spill in effect on lesion distance.

It is worthy of note that the spill in effect is more pronounced in lesion SUV_{max} than SUV_{mean} as demonstrated by the results in Figures 3.5 to 3.9. This implies that if one is interested in quantification using SUV_{mean}, then, the spill in effect is minimal and can potentially be ignored. However, the fact that SUV_{max} is the global clinical standard for quantification informs the need for proper spill in correction. Our study also shows that SUV overestimation as a result of spill in effect reduces over iteration (as seen in Figures 3.4, 3.9, 3.15 - 3.17). Therefore, in order to reduce the spill in effect, slightly increasing the number of iteration might be a good alternative. However, this will be at the expense of reduced CNR and increased noise.

OSEM+PSF and OSEM+PSF+BC were used as correction techniques for the spill in effect (their convergence properties are shown in Figure 3.4). For L3, there does not seem to be any major improvement in OSEM+PSF reconstruction over OSEM especially for SUV_{max} (as seen in Figure 3.9). This could be because of the closeness of the lesion to the bladder, coupled with the blurring effect caused by post-filtering. This seems to nullify the recovery already obtained by incorporating PSF into the reconstruction algorithm, thereby making both ordinary OSEM and OSEM+PSF reconstructions to behave in a similar way. This blurring effect could further be confirmed by a pronounced bias at the bladder edges due to the spill in activity from the bladder as shown in Figure 3.10, as well as the edge analysis in Table 3.3. OSEM and OSEM+PSF are

greatly affected by filtering, but OSEM+PSF+BC is more robust and less sensitive to filters. Another reason for the similar behaviour between OSEM and OSEM+PSF might be the simplistic spatially-invariant resolution modelling in this study. This simple resolution modelling has been shown by past studies to increase edge artefact and system blurring (Alessio et al. [2010]).

From the NEMA phantom experiment (Figure 3.14), this spill in activity from the bottle can cause between 20 - 90% activity overestimation in a sphere if it is within 1-2 voxels away from the hot bottle, but it reduces as we move further away from the bottle. The spill in activity reduced greatly with OSEM+PSF+BC as it shows a value less than 3% in all cases. In this phantom experiment, spill in effect is only prominent within 3 voxels ($<$ 10 mm) around the hot bottle, whereas in the simulation study, this effect could potentially extend to about 15 mm with a very high activity in the bladder. This is an indication that this spill in effect is strongly dependent on the activity in the hot region. Further validation of this technique using patient data also establishes the spill in effect as a function of distance from the hot region (Figure 3.15). OSEM and OSEM+PSF images show an increased activity value in the immediate vicinity of the spleen compared to OSEM+PSF+BC image, but this disparity in activity value decreases as we move further away from the spleen.

From the results shown in Figures 3.9, 3.10 and 3.12, it could be seen that better lesion detection and quantification could be achieved with the recently proposed background correction technique, thereby potentially enhancing low contrast lesion detectability and better diagnosis. This was also confirmed by the NEMA phantom (Figure 3.13) as OSEM+PSF+BC demonstrate higher CNR than OSEM and OSEM+PSF especially at lower iterations and for smaller

spheres. Also, the recently proposed background correction method has a stable performance for both lesion SUV_{mean} and SUV_{max} (demonstrated by almost 0% change in Figure 3.9) irrespective of the bladder activity and application of post-filter. This performance stability is an indication that the correction method can be used in the clinic for treatment response monitoring, however, this is still subject to further validation.

When compared with previously published results (Liu [2012], Silva-Rodriguez et al. [2016]), this current study presented a complete and thorough analysis demonstrated on acquired PET data probably due to improved correction technique, incorporation of PSF in the reconstruction, and improved scanner resolution. There is an indication that the recently proposed background correction technique is robust and efficient in removing spill in activity from the high activity regions to the surroundings, thereby producing more reliable lesion quantification and better lesion visibility, compared with other correction techniques. Moreover, it is less tedious in that there is no need to calculate each lesion activity separately.

However, the recently proposed background correction technique is highly dependent on segmentation accuracy as shown in Figure 3.11. This is important especially for pelvic scans where the bladder changes in volume and shape over time. The results showed that the segmentation error is pronounced after 10 mins where the bladder expands majorly in an anterior direction towards the rectum and superior to the pelvic organs. This is in line with past studies (Foroudi et al. [2013], Grønborg et al. [2015]) which showed that bladder expands primarily in the superior anterior direction, and hence, addition of anisotropic margins to the bladder are necessary. The translation of this correction technique to

clinical application would need to take into account the inaccuracy in bladder segmentation either by adding additional margins or by manual correction as suggested by past studies.

With the emergence of new tracers such as [^{68}Ga]-prostate specific membrane antigen (PSMA) for prostate imaging, this correction technique can also be applicable for correcting shine-through effect in PET/MR imaging which causes loss of resolution and image artefacts due to its significant urinary excretion (Steiner et al. [2009], Kolb et al. [2015]). Therefore, accurate correction will enhance reliable quantification of PET images, and may lead to a tangible breakthrough in [^{68}Ga]-PSMA imaging.

Clinical translation of this technique would need to place careful emphasis on the segmentation of the high activity region. For example, it could be possible to use an MR image to segment the region as done in this study. Although segmentation could be performed on CT images as well, this is more challenging as PET/CT acquisitions are not performed simultaneously and there is the potential of bladder expansion between CT and PET scanning due to physiological motion. This has been reported to cause conspicuous distortions in lesions' shape and location (Cal-González et al. [2017]). Another segmentation mismatch could also result from increase in bladder shape and size during a typical PET/MR scanning session. These issues could cause loss of resolution and inadequate quantification, and also limit the applicability of this correction approach, as demonstrated in Figure 3.11. A potential way of dealing with the segmentation inaccuracies might be to perform segmentation using multi-MR sequences, which could track the bladder change in shape and volume during a typical PET/MR scan. Appropriate corrections for bladder expansion and motion is aimed to be

incorporated in the BC algorithm.

3.5 Conclusion

The effect of increasing activity from hot regions on adjacent lesion quantification, as well as the improvement brought about by the recently proposed background correction technique has been extensively studied in this work. This study shows that lesions relatively close to hot regions (within 15-20 mm) are greatly affected by the spill in effect, causing reduced visibility and activity overestimation of lesions. This effect is more pronounced in SUV_{max} than SUV_{mean}, and reduces over iteration, but it is further aggravated by the use of filter. However, improved quantification and better lesion detectability were achieved with the recently proposed background correction technique irrespective of the lesion size, lesion distance from the hot region, the activity in the hot region, or application of post-filter. It could therefore be concluded that the background correction method is appropriate for reliable quantification and diagnosis of lesions near a hot region. This is particularly important when examining the pelvic areas for infection, metastases and cancer. Furthermore, this correction technique is not limited to pelvic imaging. It could potentially be applied to imaging of any high activity region such as the brain, head and neck, myocardium, as well as bone.

Chapter 4

Comparison of Correction Techniques for the Partial Volume and Spill in Effects

In the previous chapter, a thorough analysis on the spill in effect and the contributing factors (i.e. low system resolution, proximity of ROI to an active region, and the application of post-filter) was carried out. It was also shown that the BC technique is effective in correcting for the spill in effect. In this chapter, the performance of the BC technique is compared with other recent techniques in mitigating the quantitative inaccuracies due to the spill in effect and the general PVE.

This chapter consists of work previously published in Akerele et al. [2018].

4.1 Introduction

PVE poses a great limitation to PET imaging in certain clinical investigations such as [^{18}F]-NaF PET imaging of the AAA where extensive spill in from the bone into the aneurysm can be observed (Forsythe et al. [2018]). Common image analysis techniques to mitigate the spill in effect include masking out the highly radioactive region in the image space, or simply excluding areas of spill in from regions of interest around the tissue of interest (Forsythe et al. [2018]). The challenge is the high dependence of the measurements on clinician expertise. In addition, a certain degree of potentially important physiological information might be lost from the excluded regions. There is therefore a clear need for more practical methods to correct for the spill in effects.

Recently, a BC technique was implemented which iteratively removes the entire background contribution from the reconstructed image (Tsoumpas and Thielemans [2009], Silva-Rodriguez et al. [2016], Akerele et al. [2018]). This method showed promising results for spill in correction, but it was not tested in relevant clinical data, neither was its performance compared with other correction techniques. Therefore, the aim of this study is to evaluate various recently proposed PET correction techniques to compensate for the partial volume and spill in effects in simulated phantom, experimental phantoms with known activity concentration and in patients with AAA lesions in close proximity to bone tissue. The rationale for using these sets of data was to mimic various clinical scenarios where spill in effect poses a serious challenge to quantification and diagnostic accuracy.

4.2 Methods and Materials

4.2.1 Correction Techniques

Correction of PET data was implemented using three approaches: (1) background correction (BC) technique; (2) local projection (LP) technique and (3) hybrid kernelised expectation maximization (HKEM) technique.

4.2.1.1 Background Correction (BC)

This method involves segmentation of the hot background region from a high-resolution anatomical image such as MR or CT; forward-projection of the segmented background mask; and iterative removal of the background contribution as previously discussed in Chapter 2. Although, a better approach would be to estimate the background contribution iteratively, however, in this thesis, a simple and easy-to-implement approach was used where the background contribution was estimated when the variation in the background activity is minimum.

For this purpose, the change in bone activity with iteration ($\triangle$SUV (%)) was estimated using:

$$\triangle SUV(it_n)(\%) = \frac{SUV(it_n) - SUV(it_{n-1})}{SUV(it_n)} \times 100 \tag{4.1}$$

where $SUV(it_n)$ and $SUV(it_{n-1})$ are the current and previous iterations respectively.

4.2.1.2 Local Projection (LP)

A previously introduced LP method (Moore et al. [2012], Cal-Gonzalez et al. [2018]) was adapted for spill in correction as discussed in Chapter 2. In this study, the reconstructed image was segmented into a target VOI (consisting of the ROI and the hot background), and the global background outside the target VOI.

4.2.1.3 Hybrid Kernelized Expectation Maximization (HKEM)

The recently proposed HKEM method (Deidda et al. [2019b,a]), which uses information from both PET and an anatomical image in order to compensate for partial volume effects, was used in this study. Its theory and implementation has also been discussed in Chapter 2. In this work, a high-resolution MRAC image was used to extract the anatomical information needed for the algorithm. Moreover, for the HKEM parameters, the values of $\sigma_a = \sigma_p = 1$, and σ_{da} and $\sigma_{dp} = 3$ were used as it yielded the best trade-off between image quality and noise according to a previous optimization study (Deidda et al. [2019a]). The advantage of the HKEM technique is the employment of the PET image to estimate one part of the hybrid kernel, thereby reducing the dependence on the anatomical image. Also, unlike BC and LP methods, there is no need for segmentation or a preliminary reconstruction step.

4.2.2 Datasets

Three datasets were used in this study: (i) digital phantom simulation with Siemens mMR scanner (ii) an experimental cold-sphere Jaszczak phantom ac-

quired with a PET/MR scan, and (iii) 3 clinical PET datasets from patients with AAA undergoing [^{18}F]-NaF PET/CT imaging.

4.2.2.1 Simulation

For this study, the pelvic region was simulated using a digital anthropomorphic XCAT2 Phantom (Segars et al. [2010]) with a typical [^{18}F]-FDG distribution. This simulated data include a fixed size bladder with SUV 55.5 (representing the hot source) and various-sized lesions with SUV 8 placed at different positions around the bladder (as shown in Figure 4.1). Emission and attenuation images were generated and these were blurred with Gaussian filter with FWHM ranging from 4-7.5 mm in order to simulate various degree of partial volume effects from various PET scanners. The blurred images were then forward projected to obtain the sinograms using simulated Siemens mMR scanner. The forward projector used is based on Siddon's ray tracing algorithm (Siddon [1985]), tracing 10 tangential rays for each bin. ACF were calculated from the attenuation image and this was used to attenuate the emission sinogram. Constant normalisation and randoms sinograms were also generated, with the random counts making up to 20% of the total projection data. Scatter was estimated analytically using the SSS approach (Watson et al. [1996]) as incorporated into STIR (Tsoumpas et al. [2004]). A scaling factor was applied to make the scatter count 35% of the total simulated events. The random and scatter sinograms were used to generate the additive term, while the attenuation and normalisation sinograms were used as multiplicative terms.

Poisson noise was simulated for approximately 65M counts and the noisy sinograms were reconstructed using OSEM with 21 subsets and 10 full itera-

tions. The images have 344 × 344 × 127 voxels with voxel size 2.086 × 2.086 × 2.031 mm^3. Both simulation and reconstruction were done using STIR package (Thielemans et al. [2012]).

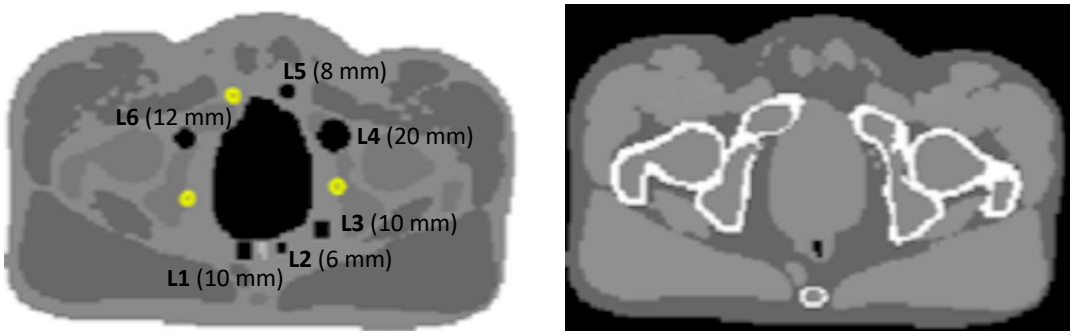

Figure 4.1: The simulated data from digital XCAT2 phantom: (a) is the emission image showing an active bladder surrounded with lesions of various diameters ranging from 6mm to 20 mm, while (b) is the attenuation image used for attenuation correction. The yellow ROIs in (a) are the selected background ROIs used to calculate the CNR.

For background correction, the bladder was automatically segmented from the digital phantom by generating an emission image where the activity is 1 in the bladder and 0 everywhere outside the bladder. The segmented bladder was multiplied by the reconstructed image obtained after three iterations to obtain the bladder contribution in the reconstructed image. This was then forward-projected to obtain the sinogram using the same settings for the simulation. The sinogram was then included as a background term along with additive term in the reconstruction to obtain a corrected image with bladder activity masked out.

ROI analysis was done by placing spherical ROIs with diameters equal to the lesion sizes on the exact position of the lesions. Mean and maximum SUV

values (SUV_{mean} and SUV_{max}) in each ROI was estimated for quantification purpose. For each reconstruction technique, the RC and CNR of each lesion was estimated using Equations (4.2) and (4.3). These were used as figures of merit to show the resolution recovery, image contrast as well as the noise properties of each correction technique.

$$RC = \frac{lesion\ SUV_{estimated}}{lesion\ SUV_{true}} \tag{4.2}$$

$$CNR = \frac{SUV_{lesion} - SUV_{background}}{\sqrt{\left(SD^2_{lesion} + SD^2_{background}\right)}} \tag{4.3}$$

The background values were estimated as the average of the 3 yellow ROIs shown in Figure 4.1a.

Furthermore, cross-combination of the reconstruction algorithms was performed in order to explore whether the performance of each algorithm (in terms of resolution recovery, image contrast and spill in reduction) can be further enhanced.

4.2.2.2 Experimental phantom

A physical phantom experiment was performed using the Jaszczak Flangeless Deluxe Phantom[1] acquired with the Siemens Biograph mMR^{TM} PET/MR scanner (Siemens Healthineers, Erlangen, Germany) in Mount Sinai Hospital, NY, USA. This phantom (shown in Figure 4.2) consists of six cold spheres S1 - S6 (of diameters 9.5 mm, 12.7 mm, 15.9 mm, 19.1 mm, 25.4 mm and 31.8 mm

[1]Biodex: Flangeless Deluxe PET SPECT Phantoms. Last accessed 6/6/2019. http://www.biodex.com/nuclear-medicine/products/pet-positron-emission-tomography/pet-phantoms/flangeless-deluxe-pet-and-sp

respectively) and a hot background filled with 155 MBq of [^{18}F]-FDG acquired for one hour. The Siemens mMR scanner has an energy resolution of 14.5% with a 430-610 keV energy window. The transaxial FoV is 59.4 cm and the axial FoV is 25.8 cm. The reconstructed images consisted of 344 $\times$ 344 $\times$ 127 voxels of 2.086 $\times$ 2.086 $\times$ 2.031 mm^3. Uncorrected prompt, normalization and random sinograms were generated from the acquired listmode data using the STIR (Thielemans et al. [2012]) (with 344 bins: bin size 2.04 mm; 252 views; axial compression 11 and maximum ring difference 60). The randoms were estimated using the delayed coincidence window technique with smoothing (Delso et al. [2011]). The attenuation image was obtained from a 19s MR VIBE sequence with two segmented tissue classes: air and water (Karakatsanis et al. [2016]). The attenuation image was co-registered with the PET image and resliced to match the PET resolution and FoV. ACFs were obtained from the attenuation image, while scatter was estimated using the SSS algorithm (Watson et al. [1996]) implemented in STIR (Tsoumpas et al. [2004]).

The dedicated PSF kernel for the Siemens mMR scanner was modeled as a Gaussian filter with 4.1 mm axial and 4.0 mm transverse FWHM according to experimental point source PSF measurements with the Siemens mMR scanner (Karlberg et al. [2016]). PVE correction was performed with all the techniques highlighted in Section 4.2.1. For the background correction, the hot background region of the phantom was segmented from the MRAC image and included as an additive sinogram term in the OSEM reconstruction (details in section 4.2.1a). The LP method was implemented for the phantom using two regions, namely: the 6 cold spheres, as the target VOI, and the segmented hot background region, as the global background.

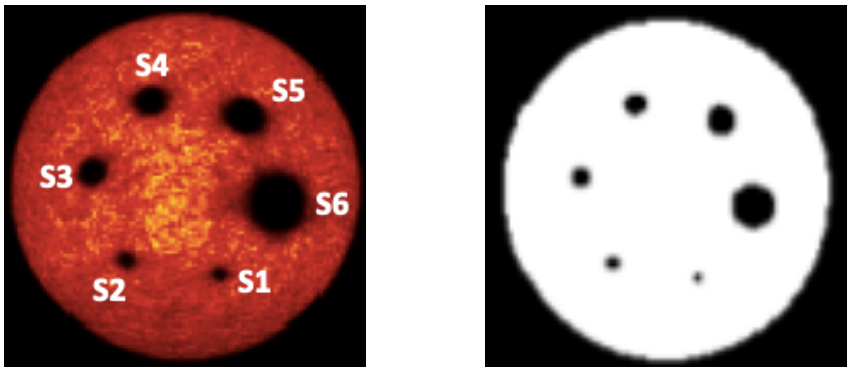

(a) (b)

Figure 4.2: The Jaszczak resolution phantom: (a) transverse slice of the PET image showing the hot background, and six cold spheres S1-S6, (b) segmented MRAC image highlighting the background region.

ROI analysis was performed by placing spherical ROIs with diameters equal in size to the actual diameters of the cold spheres. Another spherical ROI of 15 mm diameter was placed in the hot background region. These ROIs were used to extract the sphere and background mean uptakes respectively. The normalized mean activity, A_N, in each sphere was estimated so as to compare the sphere activity for each correction technique, using Equation 4.4:

$$A_N = \frac{A_{sph}}{A_{bkg}} \tag{4.4}$$

where A_{sph} and A_{bkg} are the mean uptakes in the cold spheres and hot background respectively.

4.2.2.3 Patient data

Three human patient datasets were randomly selected from the archive of the SoFIA^3 ([^{18}F]-NaF uptake in AAA) study (Forsythe et al. [2018]) involving [^{18}F]-

NaF PET/CT imaging of AAA lesions. Each patient was injected with 125 MBq of [^{18}F]-NaF and imaged on the Biograph mCT^{TM} PET-CT scanner (Siemens Healthineers, Knoxville, TN, USA) (Irkle et al. [2015]). A low-dose CTAC scan was performed (120 kV, 50 mAs, 5/3 mm) followed by a PET acquisition using 3 $\times$ 10 min bed positions to ensure coverage from the thoracic aorta to the aortic bifurcation. The raw data were extracted into sinograms using the Siemens e7 tool, and the sinograms were reconstructed with OSEM using 21 subsets and 30 iterations. PSF modelling was incorporated into the reconstruction of all the spill in correction methods as an isotropic 3D Gaussian kernel with 4.4 mm FWHM in both axial and transverse planes (Karlberg et al. [2016]). A 3-tissue LP algorithm was implemented, where the image was segmented into a target VOI consisting of the aneurysm, and the hot bone (i.e. J=2), and the global background outside the target VOI. A sample patient scan showing the attenuation image, PET image and the segmented bone is shown in Figure 4.3.

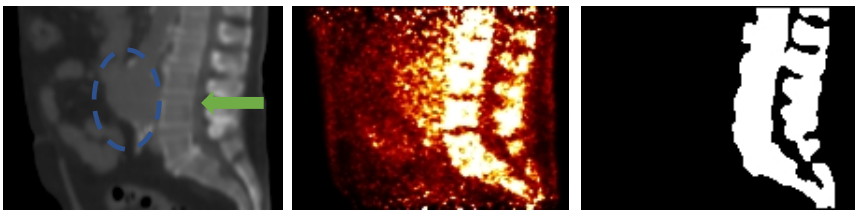

Figure 4.3: Sagittal view of an [^{18}F]-NaF PET/CT scan of a patient with AAA: (a) CT-based attenuation image where the AAA (circled with a blue dashed line) is in close proximity to the bone (shown with green arrow), (b) PET image, and (c) active bone segmented from the CTAC image.

ROI analysis was performed by delineating the aneurysmal aorta to estimate the mean and maximum SUVs (SUV$_{mean}$ and SUV$_{max}$) in the aneurysm. The

scaling factor between the Siemens and STIR reconstructed images was obtained with one data from patient using the least-squares fitting technique. This scaling factor was then applied to all patient datasets to obtain the SUVs. Following the standard clinical quantification (Vallabhaneni et al. [2004], Pawade et al. [2016], Forsythe et al. [2018]), the maximum target-to-background ratio TBR_{max} was estimated using:

$$TBR_{max} = \frac{SUV_{max}(T)}{SUV_{mean}(B_p)} \tag{4.5}$$

where $SUV_{max}(T)$ corresponds to the maximum SUV in the target (aneurysm), while $SUV_{mean}(B_p)$ is the mean SUV in the background (blood pool region in the inferior vena cava).

To demonstrate the magnitude of the spill in effect from the bone to the aorta, two ROIs were delineated: ROI_1, denoted as AAA, covers the entire aneurysm and ROI_2, denoted as AAA_{exc}, excludes the AAA parts very close to the bone, as has been reported previously (Forsythe et al. [2018]). The SUV at the aneurysm was then quantified using these two ROIs as shown for all the 3 patient datasets in Figure 4.4.

The performance of all the reconstruction algorithms was evaluated in terms of the contrast (C_{TB}) of the aneurysm region against normal tissue.

$$C_{TB} = \frac{\frac{1}{N_T}\sum_j^{N_T} T_j}{\frac{1}{N_B}\sum_j^{N_B} T_k} \tag{4.6}$$

where T_j is the value of voxel j of the reconstructed image, j is one of the N_T voxels of the target region (AAA), and k is one of the N_B voxels of the background normal tissue.

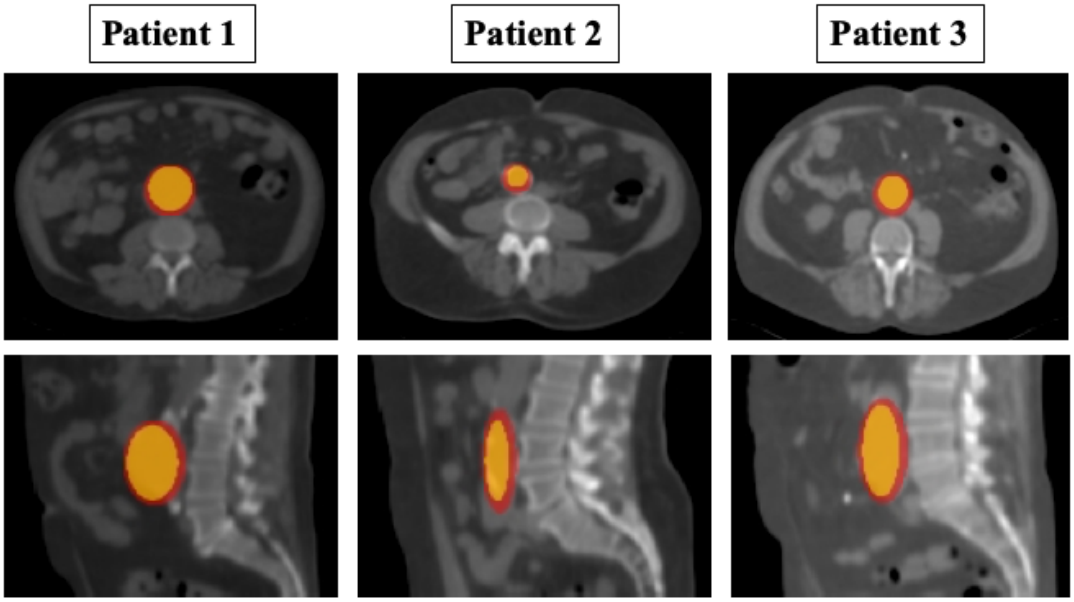

Figure 4.4: The transverse and sagittal views of the CTAC images for all the 3 patients, showing the ROIs used to extract the SUVs at the aneurysm.

The coefficient of variation (CoV) was used as the noise metrics for all algorithms, defined as:

$$COV = \frac{1}{\frac{1}{N_T}\sum_j^{N_T} T_j}\sqrt{\frac{1}{N_T - 1}\sum_j^{N_T}\left(T_j - \frac{1}{N_T}\sum_j^{N_T} T_j\right)^2} \tag{4.7}$$

These metrics were computed at each iteration using AAA_{exc} in order to avoid the influence of the spill in contamination on the results.

4.3 Results

4.3.1 Simulation

4.3.1.1 Partial volume and the spill in effects as it affects lesion quantification

In order to explore how partial volume affects lesion quantification, various PET resolution were simulated by blurring the simulated images with Gaussian filters ranging from 4 mm to 7.5 mm FWHM.

Figure 4.5 shows the RC_{mean} and RC_{max} of all the simulated lesions as the FWHM increases. These were obtained from the SUV_{mean} and SUV_{max} of all lesions using Equation 4.2, and estimated from the OSEM images at 10 full iterations. As expected, the RC_{mean} and RC_{max} for all the lesions increase as the resolution FWHM improves, with the best recovery obtained at 4 mm FWHM. Also, the lesion L2 which has the smallest diameter (i. e. 6 mm) has the smallest recovery coefficient. Even at the best simulated resolution of 4 mm FWHM, the recovery is only about 0.6 and 0.7 for RC_{mean} and RC_{max} respectively. The highest RC is expected for L4, being the biggest lesion (diameter = 20 mm), however, L1 (10 mm) closest to the bladder has the highest RC_{mean} and RC_{max} for all FWHMs. Also, L5 (8 mm) close to the bladder has almost the same RC_{mean} and RC_{max} with L4 (20 mm), and this is higher than that of L3 (10 mm) and L6 (12 mm).

These effects are further explored for all lesions as iteration increases, and the result is displayed in Figure 4.6. In both cases, one would expect the RC values to increase with iterations. However, this is only true for lesions L3, L4

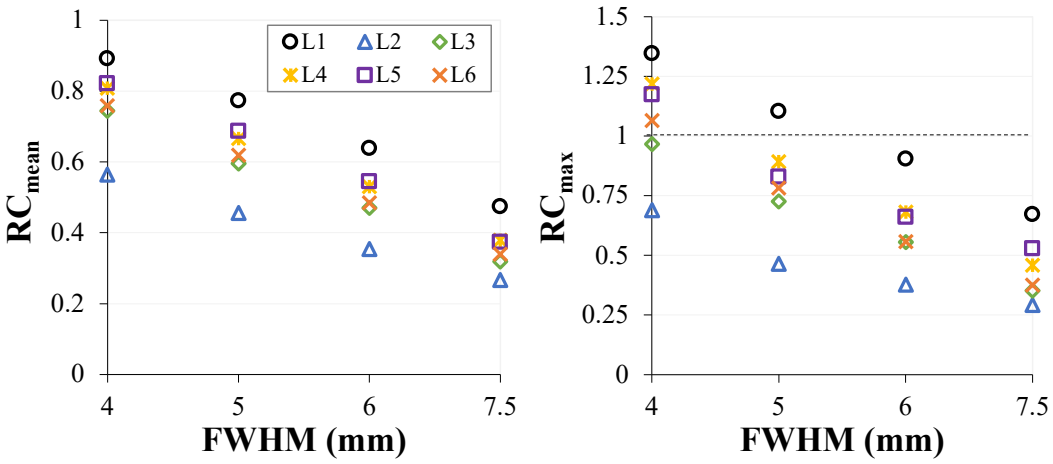

Figure 4.5: The RC_{mean} and RC_{max} of all lesions as a function of increasing FWHM. This is shown for OSEM reconstruction at 10 full iterations with the application of 4 mm Gaussian post-filter. A good recovery is given by an RC value of 1 as specified by the dashed line.

and L6 which are farther from the bladder. Lesions L1, L2 and L5 (close to the bladder) have overestimated RCs (> 1) at lower iterations, and these slightly reduce towards convergence as iteration increases, especially at 7.5 mm FWHM. But, at 4mm FWHM, the RC of L1, L2 and L5 only reduces for the first 3 iterations, after which it starts to increase. However, in all cases, RC seems to be stable at the 10^{th} iteration, therefore, all analyses were performed at iteration 10.

4.3.1.2 Correction of partial volume and spill in effects with the correction algorithms

Figure 4.7 shows the RC_{mean} and RC_{max} of all the lesions at 4 mm FWHM for all the reconstruction algorithms. OSEM and PSF show higher RC_{max} than other methods, especially for lesions L1 and L4 with a significant RC overestimation of up to 40%. However, the correction methods: BC, LP and HKEM have almost

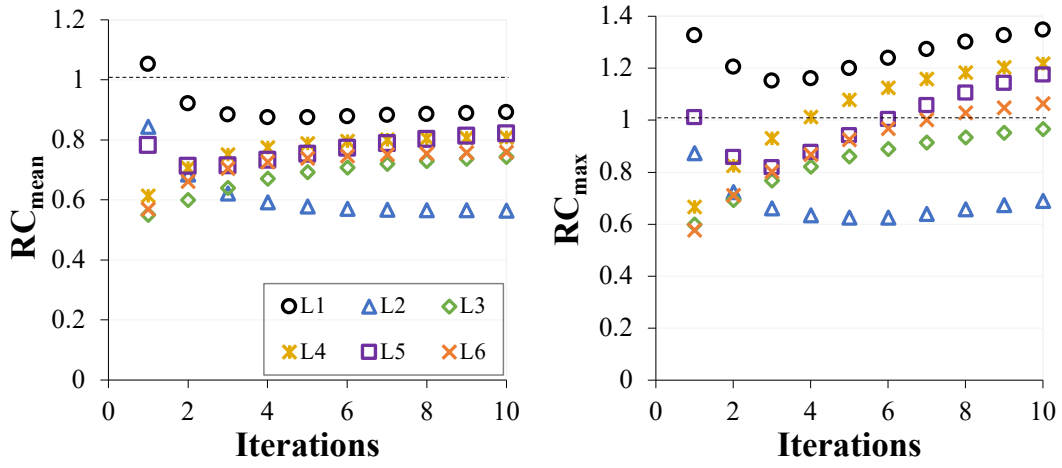

(a)

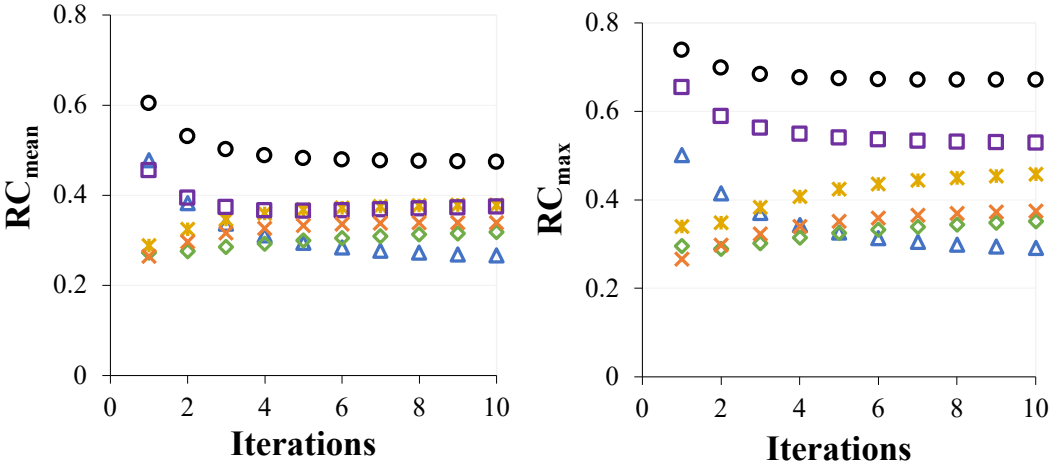

(b)

Figure 4.6: The RC_{mean} and RC_{max} of all lesions as a function of increasing iteration. Images are reconstructed with OSEM algorithm with the application of 4 mm Gaussian post-filter. This is shown for (a) 4 mm FWHM and (b) 7.5 mm FWHM. A good recovery is given by an RC value of 1 as specified by the dashed line.

steady RC values (close to 1) for all lesions except for lesion L2 which is greatly underestimated with HKEM.

In order to estimate how all algorithms perform as system resolution changes, the RC_{mean} was estimated at different FWHM used for the simulation. This is

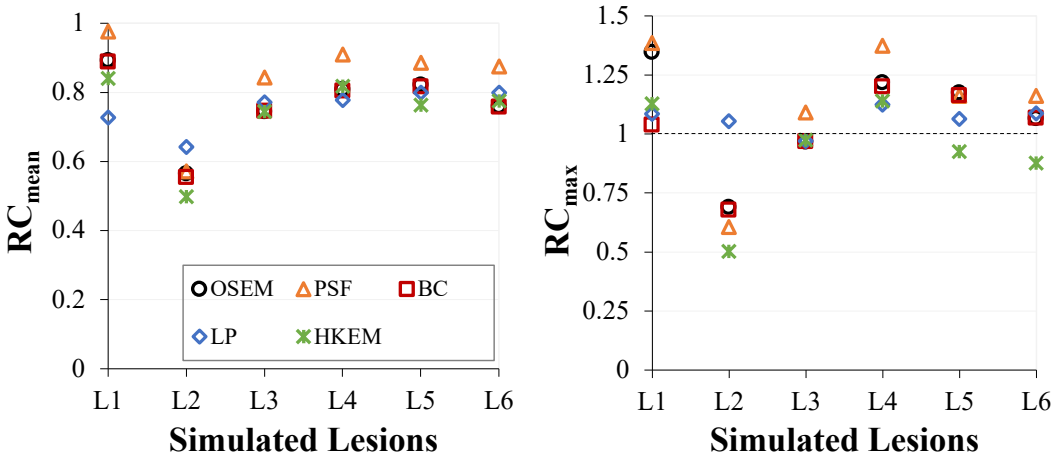

Figure 4.7: The RC_{mean} and RC_{max} of all lesions for all the methods. This is shown for FWHM 4mm at 10 full iterations. A good recovery is given by an RC value of 1 as specified by the dashed line.

estimated for lesion L3 at 10 full iterations and shown in Table 4.1.

Table 4.1: RC_{mean} for lesion L3 as a function of system resolution (FWHM). This is obtained from the SUV_{mean} at 10 iterations

FWHM (mm)	OSEM	PSF	BC	LP	HKEM
4	0.73	0.82	0.73	0.75	0.83
5	0.60	0.81	0.60	0.63	0.74
6	0.48	0.78	0.50	0.52	0.62
7.5	0.34	0.73	0.35	0.38	0.47

As expected, the RC reduces with a decreasing system resolution, but PSF, LP and HKEM have very good RC even at low resolution. HKEM has the highest RC at 4mm FWHM, while PSF gives the highest RC for all others FWHM, with a relatively small % change as FWHM increases from 4 to 7.5 mm.

To estimate the image contrast and noise properties of each method, the CNR_{mean} and CNR_{mean} were calculated for lesion L3 as iteration increases using Equation 4.3, and this is shown in Figure 4.8. BC, LP and HKEM methods have higher CNR than OSEM and PSF using both SUV_{mean} and SUV_{max}, but LP

and HKEM have significantly higher values than BC for CNR_{max}.

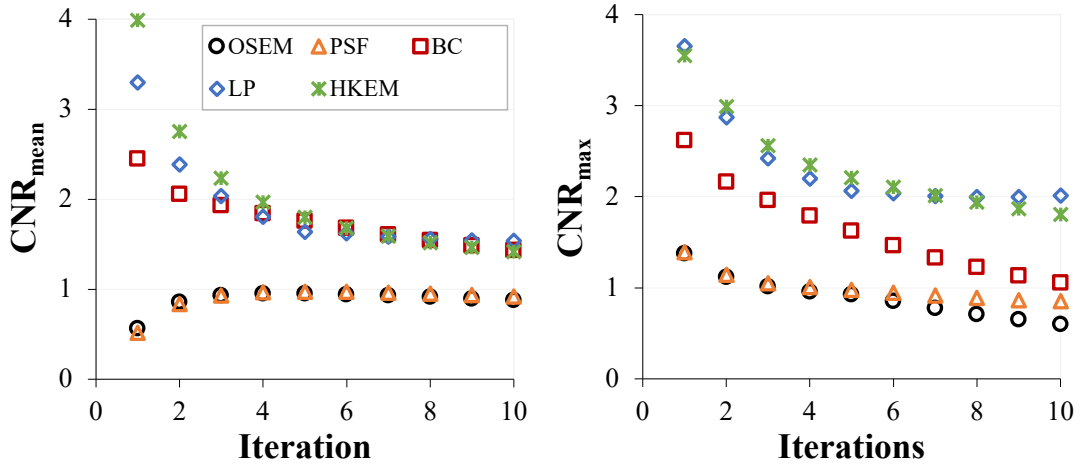

Figure 4.8: The CNR_{mean} and CNR_{max} of both uncorrected and corrected images. This is shown for lesion L1 and FWHM 4mm.

4.3.1.3 Improved performance of the correction algorithms by cross-combination

Potential improvement in the correction algorithms was explored by combining each algorithm with another. The possible combination pairs and the resultant RC mean of the algorithms at FWHM 7.5 mm are displayed in Table 4.2.

Table 4.2: RC_{mean} of L3 at FWHM 7.5 mm obtained by method combination. The diagonal values are the original values for each correction technique, while the off-diagonal ones are obtained from cross-combination.

	PSF	BC	LP	HKEM
PSF	**0.73**			
BC	0.81	**0.35**		
LP	0.84	0.39	**0.38**	
HKEM	0.77	0.40	0.39	**0.47**

The result shows that BC, LP and HKEM methods give major improvement

when they are combined with PSF, but a very small improvement when they combine with each other.

4.3.2 Experimental Phantom

For the resolution phantom, the normalized mean uptake value in each of the cold spheres was obtained from all the reconstructed images (using Equation 4.4). The result is displayed in Figure 4.9.

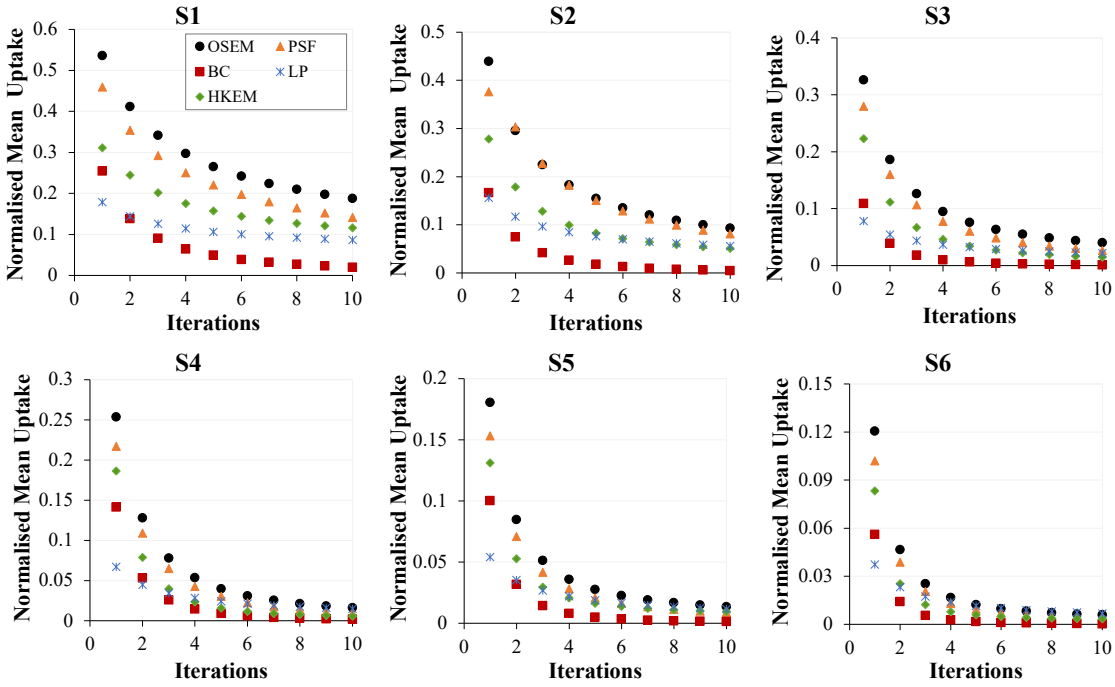

Figure 4.9: Normalized mean uptake against the iterations in each sphere for each reconstruction algorithm.

Although the spheres are meant to be cold (i.e. without any uptake), the reconstructed images showed a certain level of residual uptake in the spheres which varied in magnitude as a function of the spheres' diameter. Smaller spheres

had higher uptake than bigger ones, with sphere S1 having the highest activity and S6 having the least. For OSEM images at the 3^{rd} iteration, sphere S1 had about 34% of the background activity, while sphere S6 had only 3%. The residual uptake in the spheres reduced with increasing number of iterations. For S1, the uptake was as much as 54% at the 1^{st} iteration but reduced to only 19% at the 10^{th} iteration (showing about 75% reduction in spill in activity). The correction techniques reduced the spill in effects in the cold spheres, with BC exhibiting the best performance for all the spheres. Furthermore, LP performed better than other reconstruction algorithms in reducing the spill in activity in the spheres, but not as much as BC.

4.3.3 Patient Data

4.3.3.1 Estimation of the background contribution

The background contribution was estimated at an iteration when the variation in background activity is minimum. This was done for the patient datasets, where the change in bone SUV with iterations was estimated using Equation 4.1. Figure 4.10 showed the plots of $\triangle\text{SUV}_{mean}$ (%) and $\triangle\text{SUV}_{max}$ (%) against iterations for the 3 patient datasets used in this study. For almost all cases, the $\triangle$SUV (%) is negligible after the 3^{rd} iterations. The background contribution was therefore estimated using the reconstructed images at the 3^{rd} iterations.

4.3.3.2 Comparative evaluation of the reconstruction algorithms

Figure 4.11 shows the convergence properties of each reconstruction algorithm in the 3 patient datasets. In all the 3 patients, OSEM algorithm has the high-

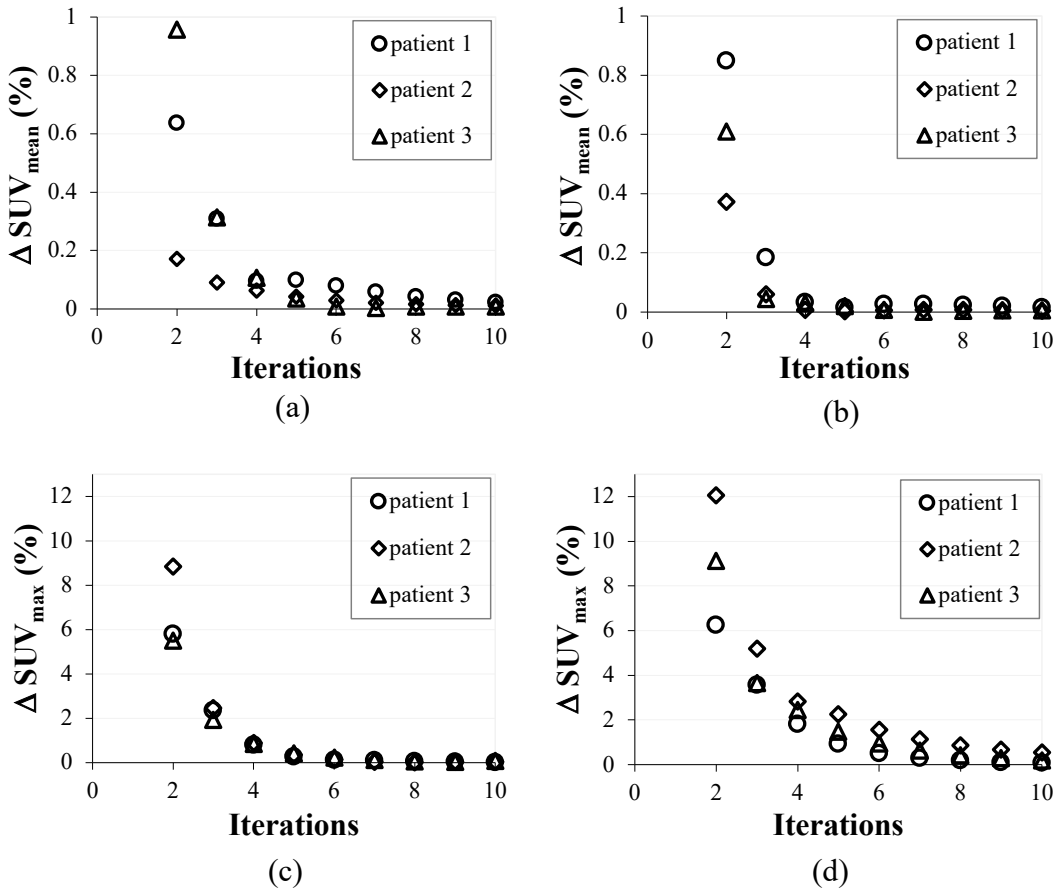

Figure 4.10: $\triangle$SUV$_{mean}$ (%) and $\triangle$SUV$_{max}$ (%) of the bone activity for the 3 patient datasets. (a) and (c) are for OSEM reconstructed images, while (b) and (d) are for PSF images.

est SUV and TBR values at early iterations, while HKEM algorithm has the least. But at late iterations, PSF has the highest values, except for patient 3 where OSEM has the highest TBR$_{max}$ at both early and late iterations. PSF and PSF+BC have similar behavior, and they do not show good convergence. However, OSEM and PSF+LP have good convergence for all the quantification metrics.

Figure 4.12 shows the CT attenuation and PET reconstructed images of the

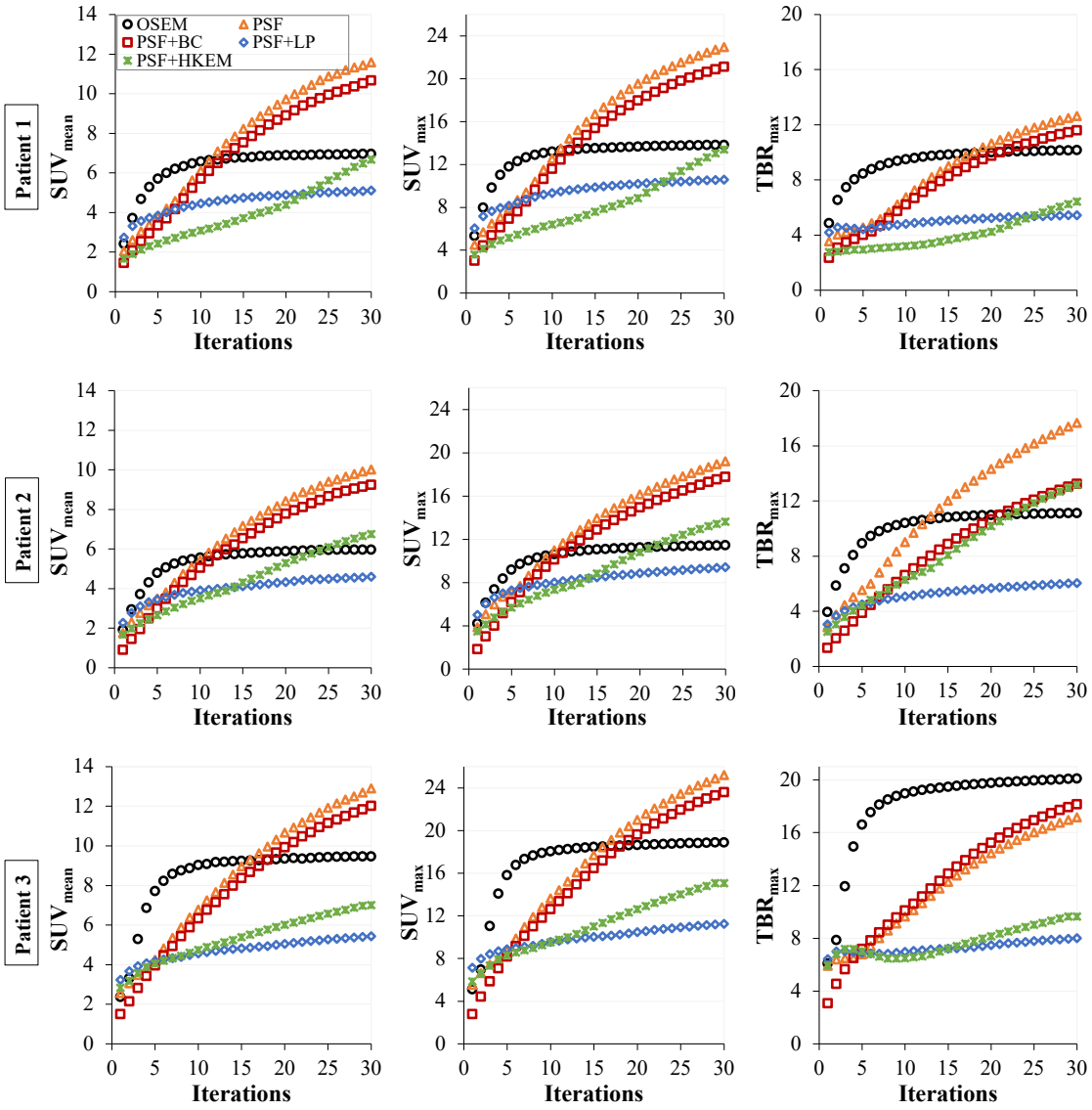

Figure 4.11: The convergence plots of the reconstruction algorithms for the three patient datasets. These plots are shown for all the quantification metrics used in this study, and the ROI was drawn over the entire aneurysm region.

three datasets under review. The PET images demonstrated higher [^{18}F]-NaF uptake in the aneurysm, compared to normal tissue. Also, a high uptake was observed in the adjacent bone, which might significantly influence quantification

at the aneurysm. It could also be seen that for all the patients, PSF-based reconstructions attained a better contrast and more reduced noise than OSEM reconstruction, with the PSF+HKEM algorithm yielding the best performance. This was also shown quantitatively for each reconstruction algorithm in terms of the contrast and CoV in Figure 4.13.

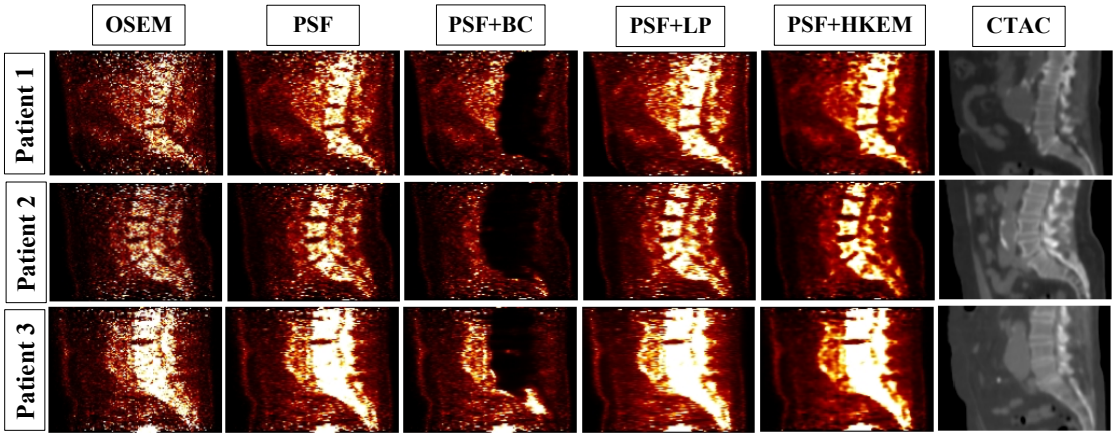

Figure 4.12: Sagittal views of the PET reconstructed images at 3 full iterations, shown for the 3 patients (top-to-bottom rows). All images are displayed with the same maximum SUV threshold value 6.

4.3.3.3 Spill in estimation and correction

The spill in activity from the bone into the aneurysm was estimated by drawing 2 ROIs on the aneurysm: ROI_1 was drawn over the entire aneurysm region (AAA), while ROI_2 was drawn such that it excluded regions close to the active bone (AAA_{exc}). Figure 4.14 shows the SUV_{mean}, SUV_{max}, and the TBR_{max} for both ROI_1 and ROI_2. These values were estimated at 3 iterations for all reconstruction algorithms. The results showed that OSEM images have higher quantitative values than PSF-based images, while PSF+HKEM images yielded

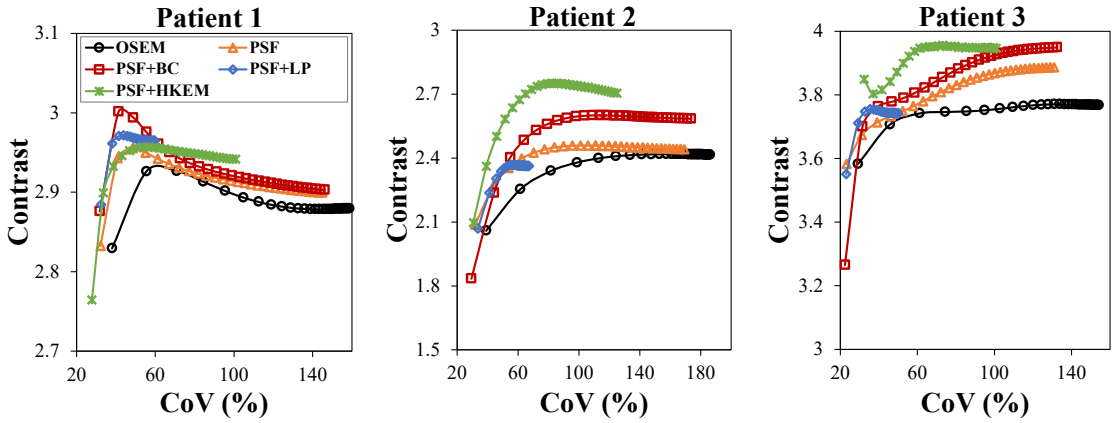

Figure 4.13: Contrast versus COV in the aneurysm as iteration increases.

the least quantitative values. Also, substantial differences between AAA and AAA_{exc} were observed for SUV_{mean}, SUV_{max} and TBR_{max}.

This discrepancy in SUV between the two ROIs is most likely due to the spill in effect emanating from the adjacent active bone. PSF-based reconstructions performed well in reducing this spill in activity for patient 1, but not for patients 2 and 3. For all 3 patients under review, PSF+BC exhibited the least differences between the two ROIs for all the quantitative metrics used, thereby suggesting the most robust spill in correction performance.

The difference in SUVs and TBR between AAA and AAA_{exc} as iteration increases was computed for all patients, and the result is displayed in Figure 4.15. The difference decreased with iterations for all algorithms, with patient 3 exhibiting the largest difference. However, PSF+BC showed an almost zero difference for all patients.

The spill in effect from the bone into the aneurysm was also shown by drawing a line profile across the bone and the aneurysm as shown in Figure 4.16. Indeed,

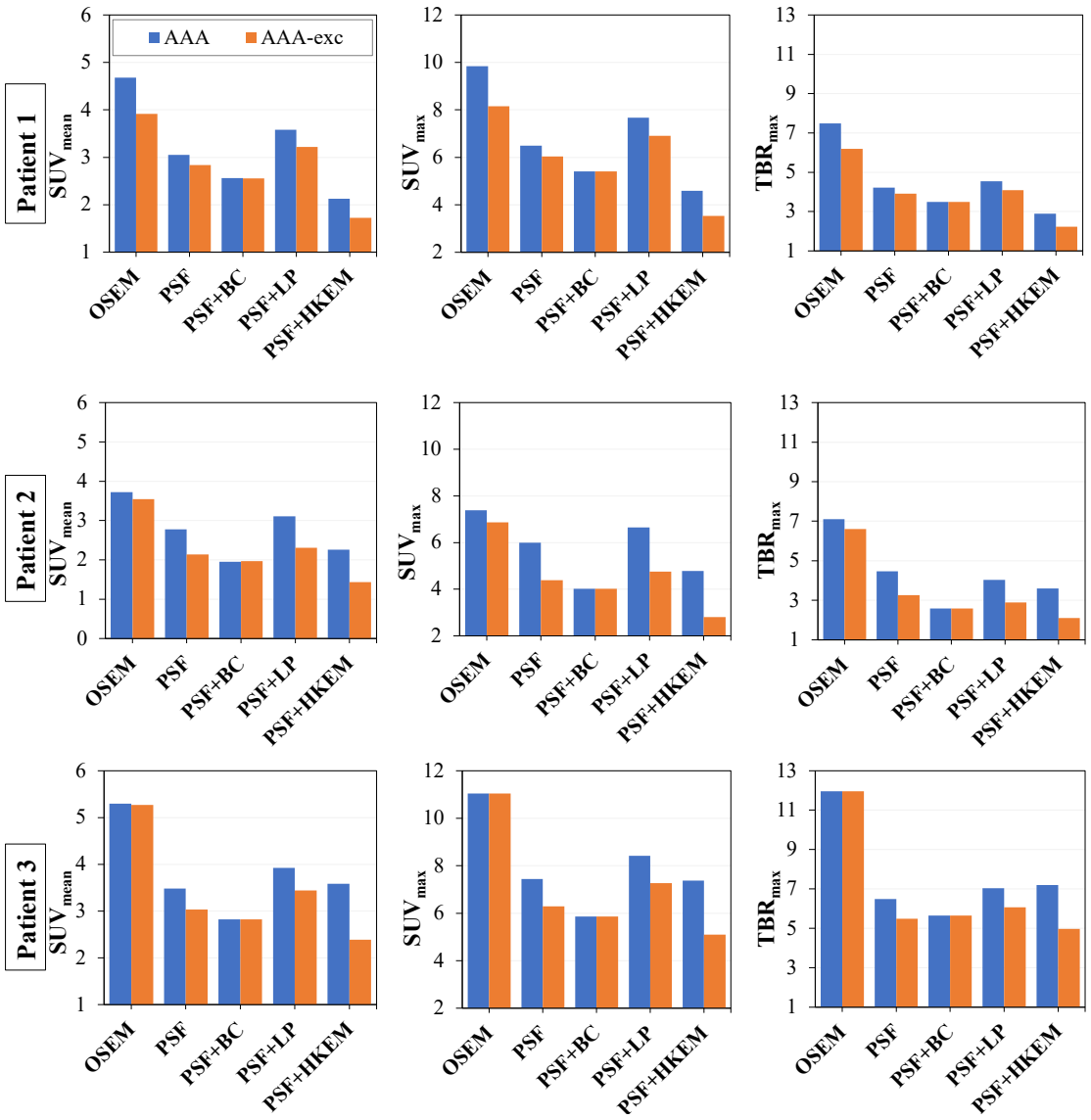

Figure 4.14: The ROI analysis for patients 1-3 (top-to-bottom rows) using all the quantification metrics for all evaluated reconstruction algorithms at 3 iterations.

the regions of the aneurysm in close proximity to the bone appeared to exhibit higher activity concentration, as they are expected to be more prone to the spill in effects from the hot background signal in the bone tissues. This was true for all the reconstruction algorithms, except PSF+BC, where the bone contribution

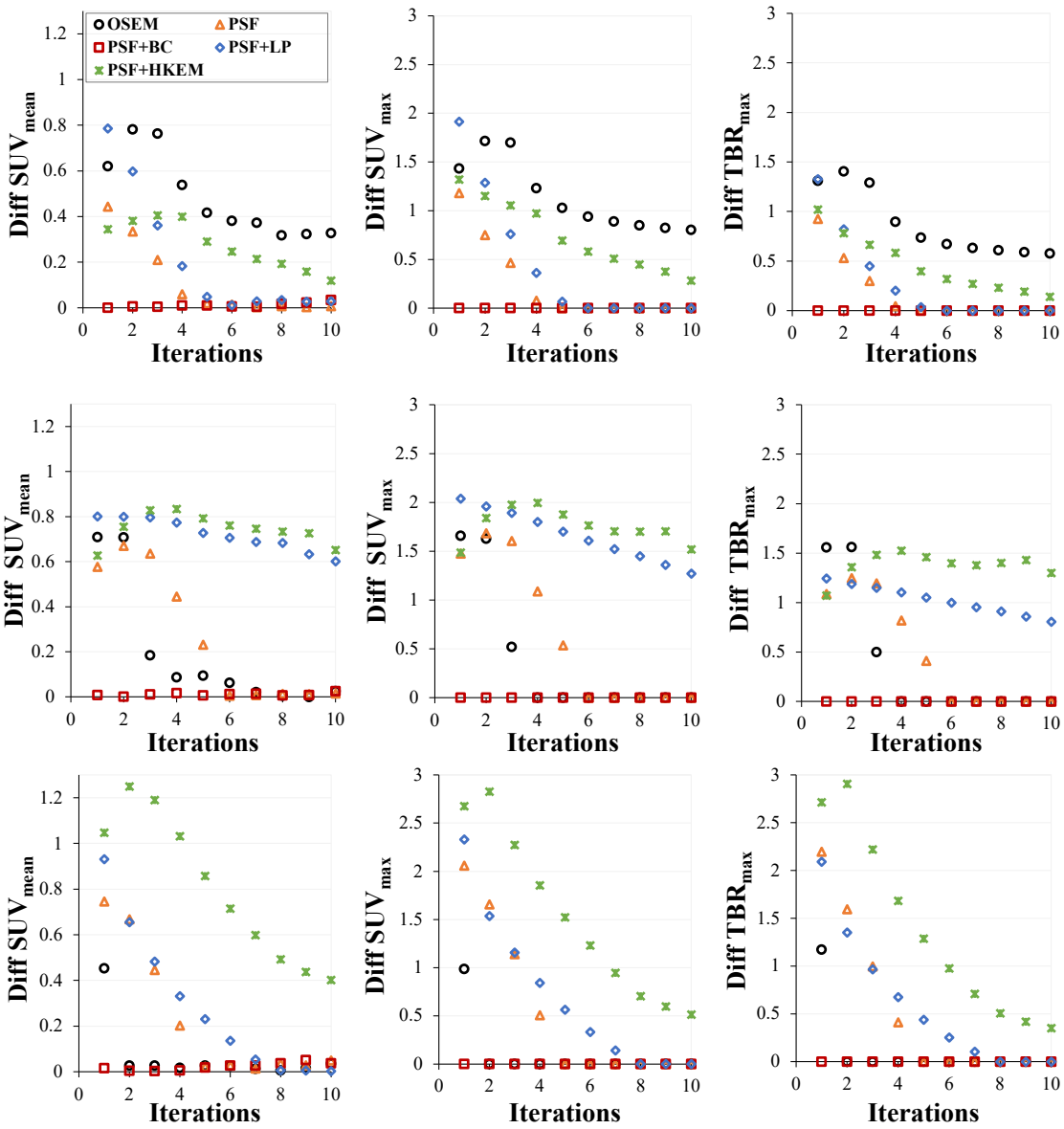

Figure 4.15: Quantification difference between AAA and AAA$_{exc}$ for all metrics. This is shown for patients 1 – 3 (from top to bottom).

was successfully removed.

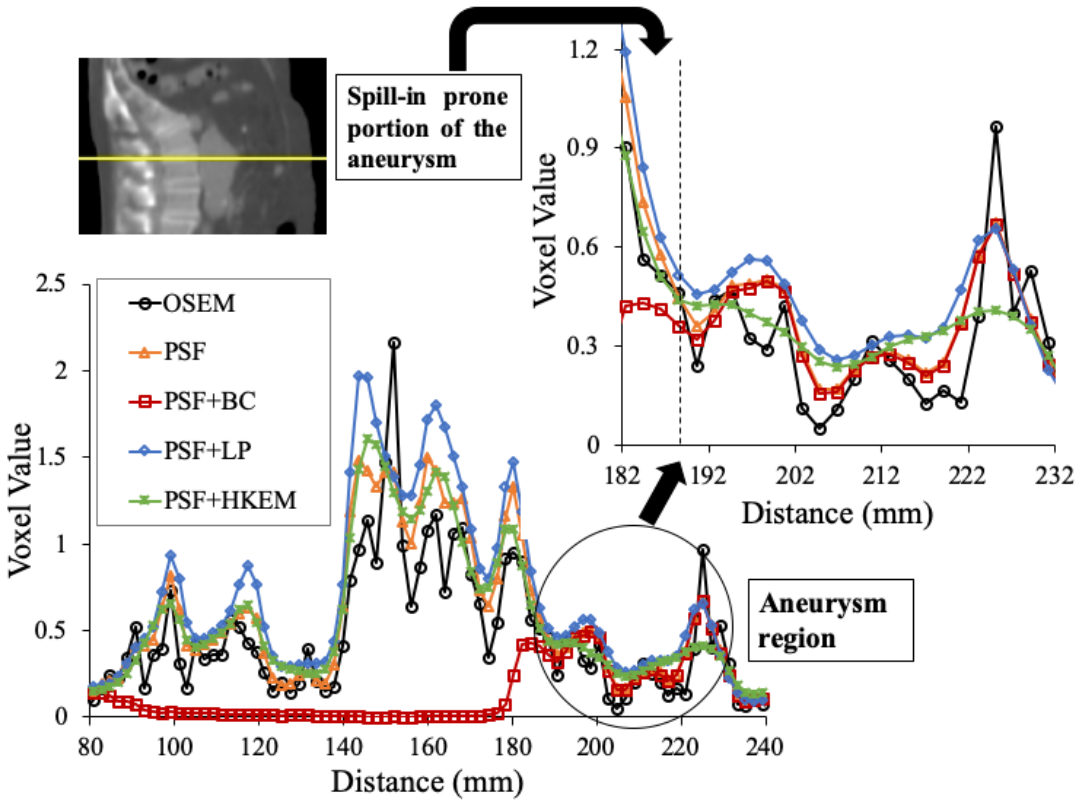

Figure 4.16: Profile across the bone and the aneurysm, showing that the portion of the aneurysm in contact with the bone are more prone to the spill in effect from the bone.

4.4 Discussion

This study has investigated the partial volume and spill in effects in target regions close to highly active background regions, and evaluated new techniques which are capable of compensating for both effects especially as it applies to different set of clinical scenarios. These techniques were compared using a simulated phantom, the resolution PET/MR phantom data obtained from a Siemens Biograph mMR^{TM} scanner and AAA [^{18}F]-NaF PET/CT data of three patients scanned with the Siemens Biograph mCT^{TM} scanner.

For the simulation, the recovery coefficients increases with increasing lesion diameter, where lesion L2 with the smallest diameter of 6 mm has the smallest recovery coefficient. Although, one would expect the RC values for all lesions to improve with increasing iterations, this is only true for lesions L3, L4 and L6. Lesions L1, L2 and L5 have their RC reducing as iteration increases, especially at 7.5 mm FWHM, until it converges at about 10 iterations. This behaviour is attributed to the spill in effect in previous studies (Akerele et al. [2018]) as these lesions are more prone to spill in effect because they are closer to the bladder (Liu [2012], Kolb et al. [2015], Puri et al. [2017], Akerele et al. [2018]). Even though L1 and L3 have the same diameter (10 mm), this spill in effect resulted in a big difference in quantification of up to 15% and 38% in RC_{mean} and RC_{max} respectively between L1 and L3. The spill in effect also makes L5 (8 mm) to have higher RC than even L4 (20 mm). However, despite the spill in effect in L2 (6 mm), it still has lower RC than other lesions for all reconstruction algorithms. This is due to the fact that the spill in effect is probably offset by the spill out effect which is more prominent in small lesions. While the spill in effects in L1 and L2 might not be surprising, one would possibly query why there is spill in effect in L5 and not L3 or L4 (because they are relatively at the same distance from the bladder). However, a possible explanation to this is that bladder expands primarily in the superior anterior direction (Foroudi et al. [2013], Grønborg et al. [2015], Akerele et al. [2018]). Therefore, lesions in that direction are more likely to be affected by an increase in bladder size and volume, and hence by the spill in effect from the bladder.

Comparing the reconstruction algorithms, OSEM and PSF images show a significant overestimation in lesion SUV_{max} of up to 40% for lesions very close

to the bladder, and small lesions are greatly underestimated (Figure 4.6). But BC, LP and HKEM methods have almost steady uptake recovery (close to 1) for all lesions except L2. Although PSF could not give a good recovery for lesions L1 and L2, it does give the highest value and lowest variability in RC for L3, as system resolution reduces (Table 4.1). This shows that PSF is more robust for resolution recovery when the lesions are not close to hot region and are bigger than 8 mm. So, for clinical routines involving these specific cases, combining PSF with any of BC, LP or HKEM methods will be an added advantage as seen in Table 4.2.

Comparing the image contrast and noise properties of all the methods, BC, LP and HKEM have significantly higher CNR than OSEM and PSF (as seen in Figure 4.8). This is because there is a spill of activity from the bladder to the surrounding, thereby making the background values higher, and subsequently reducing the CNR of the lesions. This spill of activity is corrected for by the 3 correction techniques, hence showing higher CNR.

For the resolution phantom in Figure 4.9, although the spheres were meant to be cold (i.e. without any radioactivity), the reconstructed images showed a certain level of residual activity in the spheres due to spill in effect from the background. The amount of radioactivity varied in magnitude as a function of the sphere diameter, with smaller spheres having higher activity than bigger ones, thereby suggesting that spill in effect from the background to the cold spheres is prominent in small structures. The apparent higher activity in the small spheres might also have been affected by the ROI selection. A small activity was observed also in the bigger spheres, this may be due to the positive bias induced by the non-negativity constraint of the OSEM algorithm and less because of PVEs at

the periphery of the cold spheres. The correction techniques reduced the spill in effects in the cold spheres, with BC yielding the best correction performance, as demonstrated by the almost zero activity values observed in all empty spheres at about 10 iterations. HKEM yielded a considerably lower activity for all the spheres compared to OSEM and PSF, while LP outperformed HKEM. However, LP could not remove as much activity from the cold spheres as the BC method.

The performance of the reconstruction algorithms for the patient PET images were evaluated in terms of convergence properties, contrast and CoV as displayed in Figures 4.11 and 4.13. In all 3 patients, OSEM yielded the highest SUV_{mean}, SUV_{max} and TBR_{max} at early iterations while the PSF+HKEM algorithm exhibited the lowest. However, at late iterations, PSF and PSF+BC methods attained the highest values. This could be clearly seen in Figures 4.12 and 4.13 where PSF-reconstructed images attained better noise reduction and higher contrast compared to the OSEM images. The high SUVs in OSEM reconstructed images might be due to the noise amplification of the algorithm, compared with PSF-reconstruction. In addition to the considerable noise reduction, PSF+LP and PSF+HKEM images achieved higher contrast, with PSF+HKEM yielding the best performance. The significant noise reduction attained with the PSF+HKEM method could be partly responsible for the considerably lower values obtained from the PSF+HKEM images. It should also be noted, however, that PSF reconstructions exhibited a slow convergence, which has been a commonly reported issue in past PSF resolution modelling reconstruction studies (Rahmim et al. [2013], Munk et al. [2017]).

For the patient data, the spill in effect from the active bone adjacent to the aneurysm resulted in major differences between the two ROIs (AAA and AAA_{exc})

for SUV_{mean}, SUV_{max} and TBR_{max} (Figure 4.14), especially for patient 3. This spill in effect was further demonstrated by extracting a profile across the bone and the aneurysm as demonstrated in Figure 4.16. It could be seen that regions of the aneurysm in close proximity to the bone were relatively more prone to the spill in effect from the bone. This was true for all the reconstructions algorithms, except PSF+BC, where the bone contribution was successfully removed. The differences in SUVs and TBR between AAA and AAA_{exc} decreased with a larger number of iterations for all algorithms, except PSF+BC which showed an almost zero difference in all cases. This suggests that the spill in effect might have been reduced at later iterations, as previously reported (Akerele et al. [2018]). This observation might be explained by the convergence of all algorithms with more iterations. However, a high noise amplification with little or no improvement in the image contrast was observed for higher number of iterations (Figure 4.13). Therefore, all analysis were performed at three iterations, which follows the recommended clinical settings, but without the use of post-filter.

It could also be noted that PSF+HKEM and PSF+LP images had considerably higher differences compared to the other techniques in all the quantification metrics used. Although PSF+LP performed slightly better than PSF+HKEM, it could not remove as much spill in effects in the patient data as it did for the phantom data. This could be due to the assumption that the segmented tissue inside the VOI had a uniform activity concentration (Moore et al. [2012], Cal-Gonzalez et al. [2018]). Since this is not the case for the patient data, the LP method might have had the tendency to enforce a uniform uptake over the aneurysm and the bone tissues, thereby limiting the performance of the algorithm. Also, the seemingly high spill in effect in the PSF-based reconstructions could have

been observed due to the commonly reported Gibbs artefacts, resulting in an overshoot around the hot region (i.e. bone) (Rahmim et al. [2013], Nuyts [2015], Munk et al. [2017]). This might have led to the considerably higher values for AAA than AAA_{exc}, making it appear as though there is a higher spill in effect with PSF reconstruction. However, the background correction (BC) technique corrected for this overestimation, and also improved the spill in correction in the aneurysm. The large difference between AAA and AAA_{exc} noticed for patient 3 might also have been observed due to inaccurate segmentation of the bone, and ROI-induced errors (where the aneurysm ROI partly covers the bone). This was also true for the resolution phantom where the performance of the LP method was dependent on segmentation (as earlier discussed). This suggests that these correction techniques were sensitive to segmentation errors (and potentially, misalignment of PET and CT images), which might have posed limitations to their performance. Investigations have been carried out on the effect of registration errors on the HKEM technique (Deidda et al. [2019a]) and the effect of segmentation errors on the BC reconstruction method (Akerele et al. [2018]). Past studies have also shown that there is currently no firm consensus as to which correction approach is the best (Soret et al. [2007], Hutton et al. [2013], Thomas et al. [2016]).

The performance of the BC techniques could have been further enhanced by further optimizing its implementation parameters. However, in this current work, the BC was implemented as a simple, yet effective, spill in correction technique which could be easily adopted for routine use in the clinic. Thus, we estimated the background contribution at the 3^{rd} iterations which is the most commonly employed iteration in clinical PET exams. More so, the estimated background

regions were quite active and large, and hence, it was reasonably expected that the background activity would have nearly converged after the 3^{rd} iteration, as demonstrated in Figure 4.10. However, for smaller background regions, a higher number of iteration might be required to ensure an adequate convergence.

4.5 Conclusion

The impact of the partial volume and spill in effects on PET quantification accuracy in regions of interest close to high background activity regions has been investigated. For that purpose, a systematic performance evaluation of three recently proposed promising correction techniques was carried out using simulated and experimental PET/MR phantom data as well as AAA PET/CT human patient data. The results showed that the BC method could be successfully used to correct for the spill in effects in regions close to a hot background region. The BC method was also robust to ROI-selection variability thus enhancing the accurate PET signal quantification in large varieties of target regions of interest. Although the other two techniques could not accurately correct for the spill in effect, they did give a good resolution recovery and improved detectability for small lesions. Their performance can be effectively improved when combined with PSF, or when their implementation is further optimised. These methods are promising for clinical integration for some specific cases where PVE has a significant impact on clinical decisions.

Chapter 5

Clinical Application of the Background Correction Technique

The previous chapter compared the performance of the background correction technique, in mitigating the quantitative inaccuracies due to the spill in effect and the general partial volume effect, with other novel correction techniques. The results showed that while other techniques gave improved resolution recovery and image contrast, none could effectively correct for the spill in effect as much as the BC method. Therefore, in this chapter, the BC method was applied to a specific clinical scenario where the spill in effect poses a significant limitation to PET quantification.

5.1 Introduction

Abdominal aortic aneurysm (AAA) is the irreversible dilation of the abdominal aorta to greater than 30 mm diameter, representing a more than 50% increase compared with a normal aortic diameter. As the disease progresses, the aorta becomes more enlarged, and could potentially rupture unless there is a timely clinical intervention (Sakalihasan et al. [2005]). AAA rupture is life-threatening, with more than 80% mortality rate and accounts for over 8,000 deaths annually in the UK (Metcalfe et al. [2011]). The exact causes of the emergence and progression of AAA are not completely understood, however, the most common risk factors for AAA development are smoking, male sex, hypertension and advancing age (Johansen and Koepsell [1986], Alcorn et al. [1996]).

In clinical practice, once an AAA is identified, the patient enters a surveillance programme, with serial measurements of the aortic diameter (commonly using ultrasound) until the aneurysm meets a 'diameter threshold' for considering intervention (typically 55 mm). However, the use of aortic diameter alone as a prognostic measure is somewhat limited because aneurysms vary in their progression rate and risk of rupture (Kurvers et al. [2004], Hong et al. [2010], Malm and Sadeghi [2017]). This suggests the need for more reliable tools to identify patients at risk of AAA expansion and rupture, and so the use of imaging biomarkers to assess the biological activity of AAA is a field of increasing interest.

At the moment, [^{18}F]-FDG is the most commonly used radiotracer for imaging AAA due to its property of detecting vascular diseases caused by inflammation (Cocker et al. [2012], Vaidyanathan et al. [2015]), which is a key process in

AAA progression (Lindeman et al. [2008]). However, different studies show contradictory findings in terms of correlation between [^{18}F]-FDG uptake and AAA expansion or risk of rupture (Forsythe et al. [2016], Lee et al. [2018]). The use of [^{18}F]-FDG in imaging of AAA is therefore limited, with potential confounding factors and lack of specificity, thereby raising concerns about its future clinical use in predicting potential AAA expansion and risk of rupture (Forsythe et al. [2016], Lee et al. [2018]). Therefore, an alternative radiotracer, [^{18}F]-NaF, is currently being explored as a marker for microcalcification in the cardiovascular system (Janssen et al. [2013], Dweck et al. [2014], Bellinge et al. [2018]) and has been used to investigate coronary atherosclerosis (Dweck et al. [2012a]), abdominal atherosclerosis (Cal-Gonzalez et al. [2018]), aortic stenosis (Ferreira et al. [2018]) and AAA diseases (Forsythe et al. [2018]). Preliminary investigation (Forsythe et al. [2018]) shows that this tracer is promising for improved prediction of AAA disease progression, and may therefore facilitate early intervention for those at higher risk of rupture. However, a major confounding issue is the spill in contamination from the bone into the aneurysm due to the limited PET resolution and the associated partial volume effect. [^{18}F]-NaF is predominantly taken up by bones, so, the AAA regions in close proximity to the bones have considerably higher uptake than more distal regions (Forsythe et al. [2018]).

Common conventional techniques to mitigate the spill in contamination include masking out the high uptake region in the image space, or simply excluding areas of spill in from regions of interest during image analysis. The obvious challenge in these techniques is the high dependence of the measurements on clinician subjective choices. In addition, a certain degree of potentially important physiological information might be lost from the excluded regions. These issues clearly

suggest the need for a more objective method to correct for the spill in effects. Therefore, the aim of this study is to investigate the spill in effects in patients diagnosed with AAA as a function of AAA diameter, [^{18}F]-NaF uptake in bone, as well as ROI selection. We also aim to correct for the spill in effects using the background correction technique, and then compare its performance against the conventional correction technique.

5.2 Methods and Materials

5.2.1 Datasets

Sixty-five (65) patient datasets with varying aneurysm diameter were selected at random from the archive of the [^{18}F]-sodium fluoride uptake in abdominal aortic aneurysm (SoFIA^3) study (NCT02229006) (Forsythe et al. [2018]) which involved [^{18}F]-NaF PET/CT imaging of AAA. The data consists of 55 males and 10 females with age range 72.6 $\pm$ 6.9 years, body mass index 27.4 $\pm$ 3.4 kg/m^2 and aortic diameter 48.4 $\pm$ 7.6 mm. Each patient was injected with 125 MBq of [^{18}F]-NaF and scanned with the Biograph mCT^{TM} PET-CT (Siemens Healthineers, Knoxville, TN, USA) (Irkle et al. [2015]). A low-dose CTAC scan was performed (120 kV, 50 mAs, 5/3 mm) followed by acquisition of PET data using 3 $\times$ 10 min bed positions to ensure coverage from the thoracic aorta to the aortic bifurcation.

5.2.2 Reconstruction and Spill in Correction

The data were reconstructed using the STIR library (Thielemans et al. [2012]) with the OSEM algorithm (21 subsets, 3 iterations). Additionally, PSF modelling was incorporated into the reconstruction as an isotropic 3D Gaussian kernel with 4.4 mm FWHM in both axial and transverse planes (Karlberg et al. [2016]). The spill in effect from the bone into the aneurysm was corrected using the previously proposed background correction technique (Tsoumpas and Thielemans [2009], Silva-Rodriguez et al. [2016], Akerele et al. [2018]) as explained in Chapter 2. All resulting reconstructed images were post-filtered with an isotropic 3 mm FWHM Gaussian filter which is the standard clinical setting.

5.2.3 Image Analysis

All reconstructed images (OSEM, PSF and PSF+BC) were analysed using OsiriX imaging software (version 10.0.2, Geneva, Switzerland), but, results from only sixty-three (63) reconstructed images were included in the final analysis because two (2) of them were outliers. ROI analysis was performed by drawing semi-automated ellipsoidal ROIs on the CT images. In order to investigate the spill in effect, two ROIs were drawn: (i) an ROI over the entire aneurysm (AAA), and (ii) an ROI over the aneurysm but excluding the part close to the bone (AAA_{exc}). All ROIs were drawn on the CTAC images, and then transferred to the PET images. For both ROIs, the maximum SUV was recorded on each slice and averaged, following the same approach used in the SOFIA^3 study. An ROI was also drawn on the normal aorta (non-AAA) in order to investigate if there is a significant uptake discrepancy between aneurysm and normal aorta. Following standard

clinical quantification methods (Vallabhaneni et al. [2004], Chen and Dilsizian [2015], Pawade et al. [2016], Forsythe et al. [2018]), the corrected maximum SUV, $cSUV_{max}$, and maximum target-to-background ratio, TBR_{max}, were estimated using:

$$cSUV_{max} = SUV_{max}(T) - SUV_{mean}(B_p) \tag{5.1}$$

$$TBR_{max} = \frac{SUV_{max}(T)}{SUV_{mean}(B_p)} \tag{5.2}$$

where $SUV_{max}(T)$ corresponds to the maximum SUV in the target aneurysm region, while $SUV_{mean}(B_p)$ is the mean SUV in the background (blood pool region). The blood pool SUV was taken as the average of 3 circular 2 cm^2 ROIs placed on consecutive slices at the inferior vena cava.

5.2.4 Statistical Analysis

Statistical analysis was performed using the IBM SPSS software package version 23. For all patients, we investigated whether there was a significant uptake in the aneurysm compared with the normal aorta. It is useful to note here that the AAA is normally said to have a clinically significant uptake when the % uptake difference between AAA and non-AAA is greater than 25% (Dweck et al. [2012b], Joshi et al. [2014], McBride et al. [2016.]). Additionally, a linear regression analysis was performed to investigate the correlation between [^{18}F]-NaF uptake in the aneurysm and AAA diameter, both for the uncorrected (OSEM) and corrected (PSF and PSF+BC) images. Finally, the significance of the uptake differences between the uncorrected and corrected images and between the two ROI groups

(AAA and AAA_{exc}) for all reconstruction methods was compared using a paired t-test. A P-value less than 0.05 was considered statistically significant.

5.3 Results

This section presents the quantification results of the aneurysm and normal aorta obtained from all the reconstruction algorithms. All analyses were done with reconstructed images at 3 full iterations with and without post-filtering.

Figure 5.1 shows the images as reconstructed from all three reconstruction algorithms which show a good [^{18}F]-NaF uptake in the aneurysm and the bone. Note that the bone uptake has been removed in the PSF+BC images.

5.3.1 [^{18}F]-NaF Uptake in Aneurysm (AAA) and Normal Aorta (non-AAA)

For all the patient data involved in the study, there is a higher [^{18}F]-NaF uptake (quantified as SUV_{max}) in the aneurysm than in the normal aorta both for filtered and unfiltered images, as shown in Figure 5.2. With the application of filtering, the mean SUV_{max} for the normal aorta is similar for all the algorithms, while for the aneurysm, the mean SUV_{max} is different for all the algorithms. The t-test conducted on the reconstruction algorithms showed that there is a significant difference in the aneurysm (AAA) SUV_{max} between OSEM versus PSF+BC, but not with OSEM versus PSF. There is also a statistically significant difference in the aneurysm SUV_{max} between the correction algorithms (i.e. PSF and PSF+BC). However, for the normal aorta, there is no significant difference between the uptake values of the different reconstruction methods. Without post-

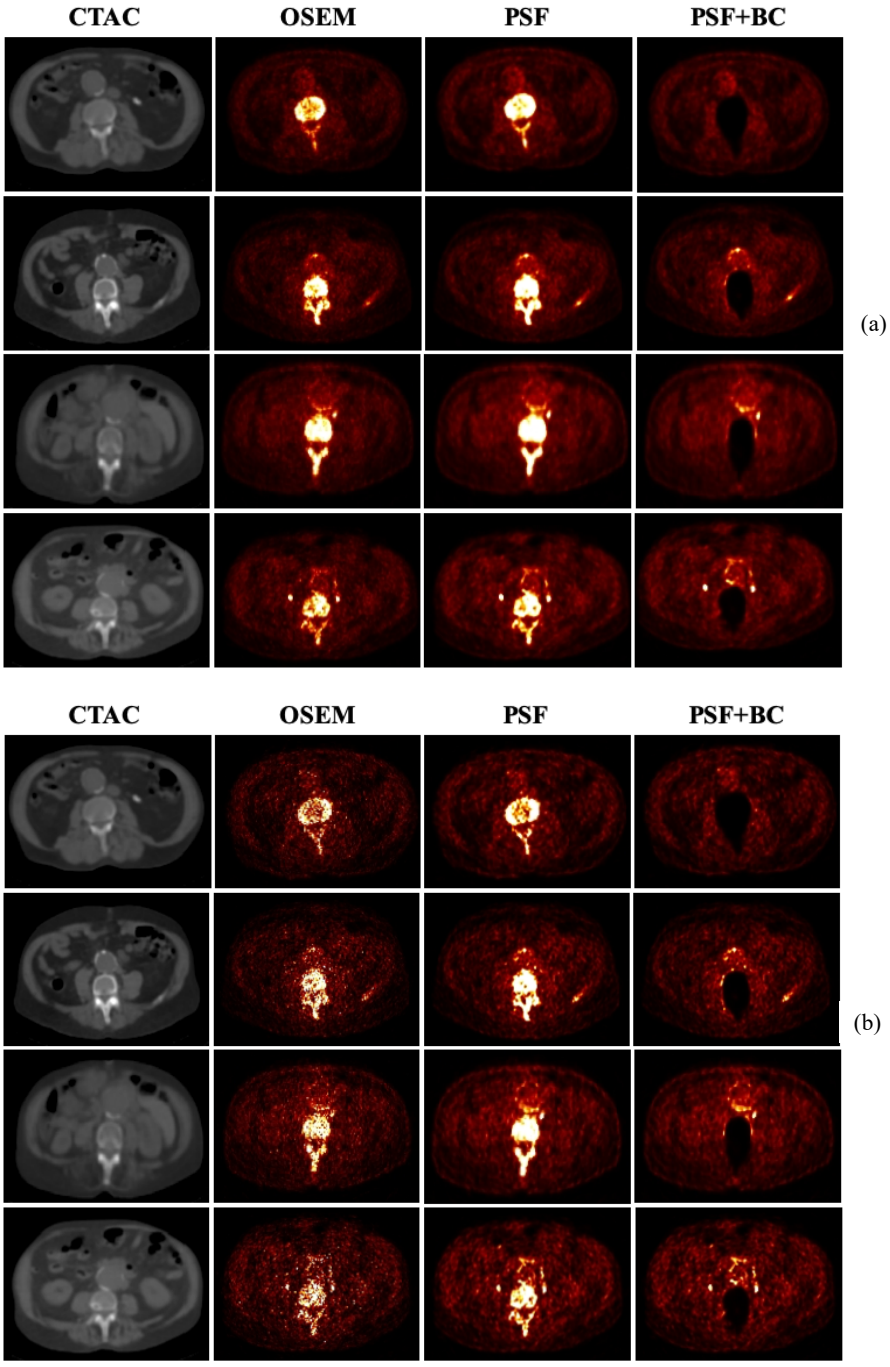

Figure 5.1: CT and PET reconstructed images of four indicative patient datasets (a) with and (b) without postfilter. These images show high [^{18}F]-NaF uptake in the bone and the aneurysm.

filtering, OSEM images have significantly higher uptake than PSF-reconstructed images, both for the aneurysm and the normal aorta, but there is no significant difference in SUV_{max} between PSF and PSF+BC images.

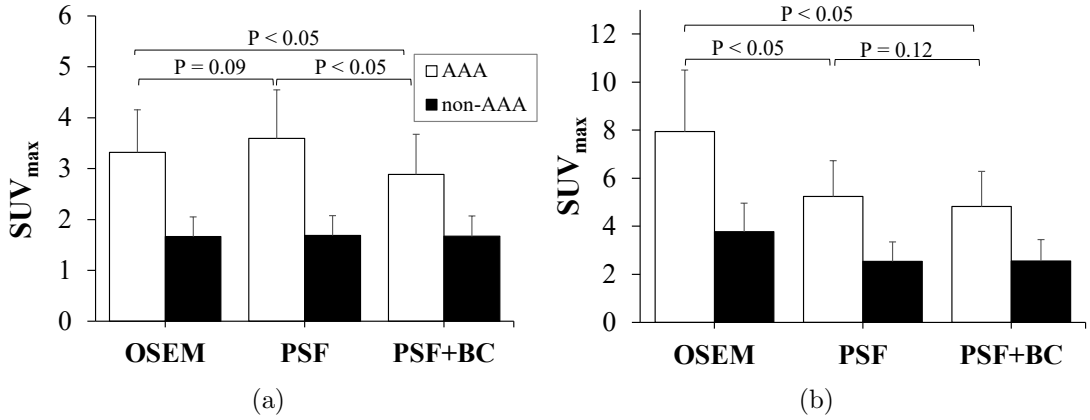

Figure 5.2: The SUV_{max} of AAA and non-AAA obtained from all the reconstruction algorithms with: (a) application of 3 mm Gaussian filter, and (b) no post-filtering. The plot displays the mean SUV_{max} of all patients and the error bar (SD). The significance of uptake differences in AAA was evaluated using paired t- test.

5.3.2 Correlation between [^{18}F]-NaF Uptake and AAA Diameter

Figure 5.3 shows the results of the regression analysis performed on all the uncorrected (OSEM) and corrected (PSF and PSF+BC) images to investigate the correlation between [^{18}F]-NaF uptake and AAA diameter. For all the reconstruction algorithms and with post-filtering, no significant correlation was observed between [^{18}F]-NaF uptake in the aneurysm and AAA diameter, (OSEM: R=0.097, P=0.99; PSF: R=0.057, P=0.99; PSF+BC: R=0.025, P=1). Although without post-filtering, there seems to be a linear but weak correlation between aneurysm

uptake and diameter, but this is not statistically significant for either of the reconstruction algorithms (OSEM: R=0.175, P=0.96; PSF: R=0.206, P=0.99; PSF+BC: R=0.161, P=0.99). Also, PSF seems to have a slightly higher (but non-significant) R value than PSF+BC, both with and without post-filtering.

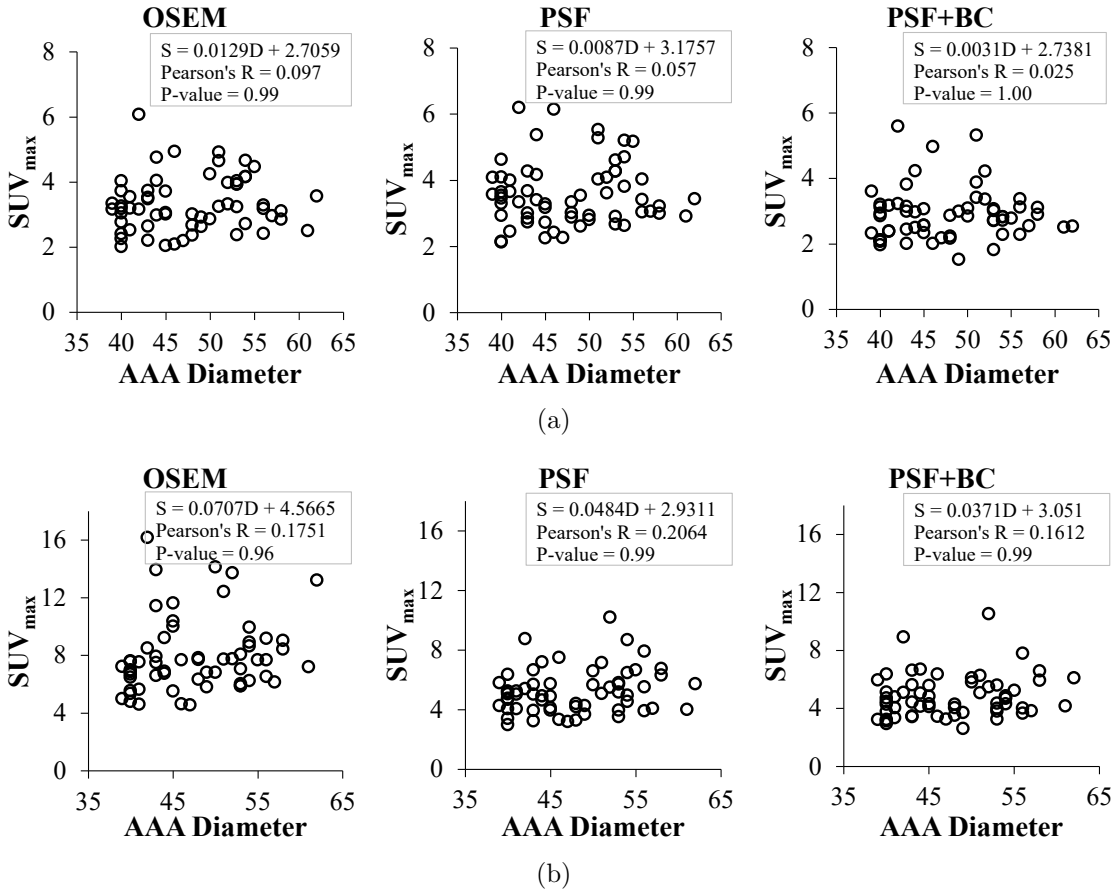

Figure 5.3: Regression analysis to investigate the relationship between [^{18}F]-NaF uptake and AAA diameter, (a) with and (b) without post-filtering respectively. [^{18}F]-NaF uptake was quantified using SUV_{max} with an ROI covering the entire aneurysm (AAA). In the equations, S & D are the AAA SUV_{max} and diameters respectively.

5.3.3 AAA Uptake Differences due to ROI Selection

Table 5.1 shows the SUV_{max}, $cSUV_{max}$ and TBR_{max} of the AAA and AAA_{exc} calculated using Equations 5.1 and 5.2. It can be seen that there is an uptake difference between AAA and AAA_{exc} for all the reconstruction algorithms, both with and without the application of post-filter. With AAA_{exc} and with post-filtering, PSF and PSF+BC almost have the same SUV_{max} (2.80), but with the whole AAA, PSF has the highest SUV_{max} (3.59 $\pm$ 0.96), while PSF+BC has the lowest (2.89 $\pm$ 0 .79). For SUV_{max}, $cSUV_{max}$ and TBR_{max}, the difference in quantification between AAA and AAA_{exc} is statistically significant for OSEM and PSF, but not for PSF+BC. Also, PSF+BC showed the least difference between AAA and AAA_{exc}, and it also had the least SD across all the quantification metrics used. Although the SUVs are significantly increased without post-filtering, there appears not to be any significant uptake difference between AAA and AAA_{exc} for all the reconstruction algorithms, except for PSF where there is a significant difference in SUV_{max} and $cSUV_{max}$.

It could also be seen (in Table 5.2) that while using AAA_{exc} with post-filtering, the mean % uptake difference ($\bar{d}$) between the aneurysm and normal aorta is about 70% for all algorithms, but this is much higher when quantifying with the AAA, as OSEM and PSF images have higher values than PSF+BC (OSEM $\approx$ 109%, PSF $\approx$ 122% and PSF+BC $\approx$ 79%). The 95% Limit of Agreement of $\bar{d}$, defined as $LOA = \bar{d} \pm 1.96SD$, is also higher in OSEM and PSF images than PSF+BC images. There is also a major difference in the number of patients having a significant AAA uptake (as depicted by a % difference >25%). With AAA_{exc}, about 84% (86% for PSF and PSF+BC reconstructions)

Table 5.1: The SUV_{max}, $cSUV_{max}$ and TBR_{max} of the aneurysm (AAA) for all the reconstruction algorithms with and without post-filtering. The SUVs of AAA were extracted using two ROIs (AAA and AAA_{exc}) in order to quantify the spill in effect from the bone. The differences between AAA and AAA_{exc} were compared using a paired t-test. Values are expressed as mean ± standard deviation (SD). A P-value less than 0.05 was considered statistically significant.

			Mean ± SD		P-Value
			AAA	AAA_{exc}	
3 mm post-filter	SUV_{max}	OSEM	3.31 ± 0.84	2.80 ± 0.80	0.00023
		PSF	3.59 ± 0.96	2.80 ± 0.75	<0.0001
		PSF+BC	2.89 ± 0.79	2.80 ± 0.76	0.43
	$cSUV_{max}$	OSEM	2.60 ± 0.79	2.07 ± 0.74	0.0001
		PSF	2.71 ± 0.88	1.92 ± 0.67	<0.0001
		PSF+BC	2.08 ± 0.69	2.00 ± 0.69	0.38
	TBR_{max}	OSEM	4.87 ± 1.58	4.10 ± 1.49	0.003
		PSF	4.27 ± 1.28	3.33 ± 1.05	<0.0001
		PSF+BC	3.80 ±1.23	3.70 ±1.25	0.55
no post-filter	SUV_{max}	OSEM	7.93 ± 2.56	7.36 ± 2.68	0.23
		PSF	5.24 ± 1.49	4.62 ± 1.50	0.026
		PSF+BC	4.82 ± 1.46	4.63 ± 1.49	0.49
	$cSUV_{max}$	OSEM	7.23 ± 2.55	6.66 ± 2.66	0.23
		PSF	4.39 ± 1.49	3.77 ± 1.48	0.024
		PSF+BC	4.04 ± 1.42	3.86 ± 1.46	0.48
	TBR_{max}	OSEM	12.15 ± 5.22	11.30 ± 5.36	0.38
		PSF	6.54 ± 2.61	5.78 ± 2.56	0.11
		PSF+BC	6.67 ±2.80	6.42 ±2.85	0.64

of the patients have significant uptake in the aneurysm, whereas with AAA, it is 94% in OSEM, 95% in PSF and 87% in PSF+BC. But without post-filtering, although the mean % uptake difference ($\bar{d}$) between the aneurysm and normal aorta is significantly increased in all the algorithms, the % number of patients having a significant AAA uptake is greatly reduced for PSF (from 95% to 89%) and PSF+BC (from 87% to 84%), but it remains the same for OSEM images. Also, the resulting difference in the % number of significant AAA uptake when quantifying with AAA and AAA_{exc} is 10% for OSEM, 3% for PSF and 1% for

PSF+BC.

Table 5.2: The analysis of the % uptake difference (d) between aneurysm (AAA or AAA_{exc}) and normal aorta (non-AAA) using the SUV_{max} with and without post-filtering. $\bar{d}$ is the mean % uptake difference for all the patients, and LOA is the 95% Limit of Agreement of $\bar{d}$, defined as $LOA = \bar{d} \pm 1.96SD$.

			Mean % difference, $\bar{d}$	SD	LOA	No with d >25% (%)
3 mm post-filter	OSEM	AAA	108.98	61.43	-11.42 to +229.38	59 (94)
		AAA_{exc}	73.54	47.33	-19.23 to +166.31	53 (84)
	PSF	AAA	121.59	65.21	-6.21 to +249.40	60 (95)
		AAA_{exc}	70.48	39.84	-7.62 to +148.57	54 (86)
	PSF+BC	AAA	78.94	42.13	-3.62 to +161.51	55 (87)
		AAA_{exc}	73.81	42.37	-9.22 to +156.85	54 (86)
no post-filter	OSEM	AAA	127.50	91.66	-52.15 to +307.15	59 (94)
		AAA_{exc}	111.01	91.00	-67.36 to +289.37	53 (84)
	PSF	AAA	119.78	77.80	-32.71 to +272.26	56 (89)
		AAA_{exc}	93.29	73.93	-51.62 to +238.20	54 (86)
	PSF+BC	AAA	103.33	76.06	-45.74 to +252.41	53 (84)
		AAA_{exc}	95.94	78.07	-57.08 to +248.95	52 (83)

This disparity in quantification between AAA and AAA_{exc} is partly due to the spill in effect from the bone into the aneurysm, as shown with line profiles extracted from all the reconstruction algorithms in Figure 5.4. The Figure presented two patient cases: Case 1 where aneurysm is detached from the bone (Figure 5.4a and c); and Case 2 where the aneurysm is attached (Figure 5.4b and d). The maximum voxel values were extracted from the normal aneurysm part (A1) and the aneurysm part close to the bone (A2), and the results are presented in Table 5.3.

This spill in effect varies in magnitude with the relative position of the aneurysm to the bone, as aneurysms in close contact with the bone suffer more spill in effect than detached aneurysms. When the aneurysm is detached from the bone (Figure 5.4a), the maximum voxel value for PSF obtained with 3 mm

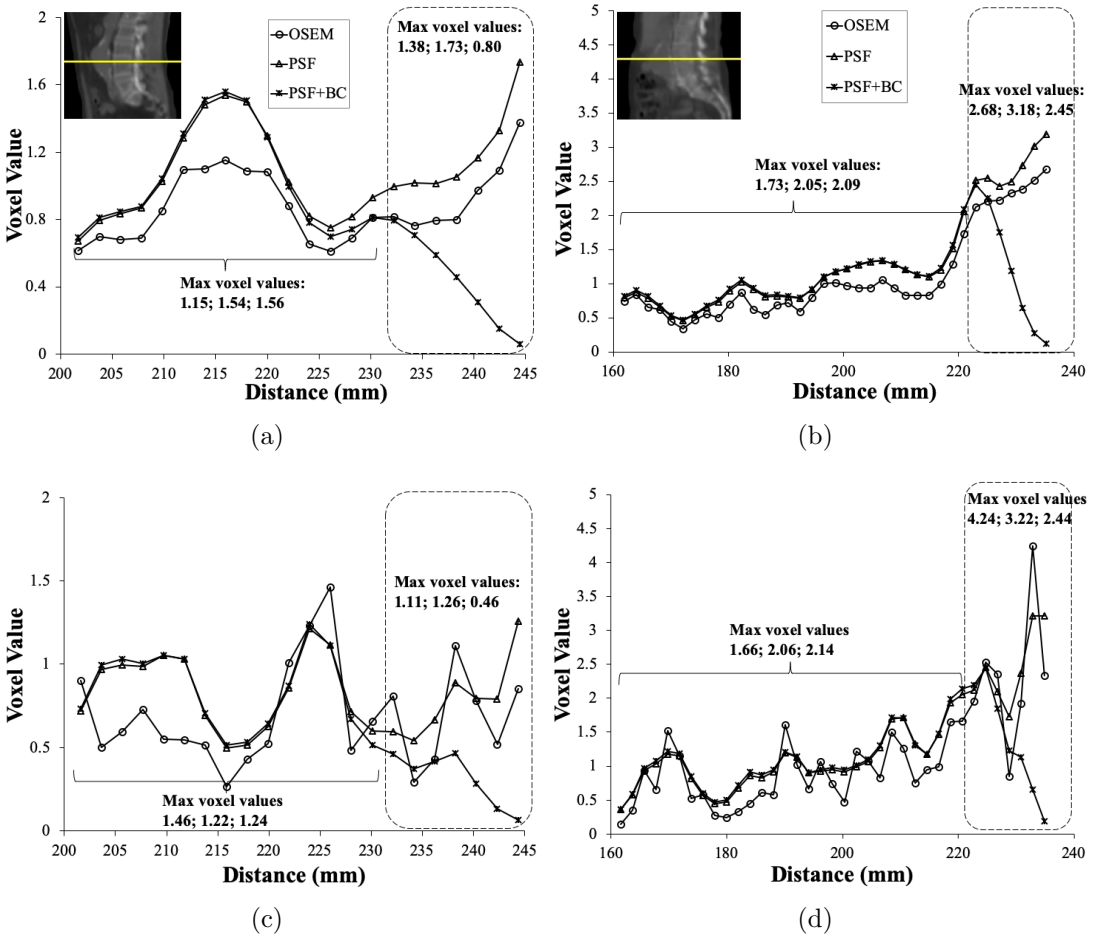

Figure 5.4: Profile across the bone and the aneurysm showing the spill in effect from the bone to the aneurysm. (a) and (b) are images with 3 mm Gaussian filter, while (c) and (d) are images without post-filter. The portion of the aneurysm prone to the spill in effects from the bone is highlighted with the dashed rectangle. In (a,c), the aneurysm is detached from the bone, but in (b, d), it is in contact with the bone.

post-filter is 1.73 in the spill in prone area, and 1.54 in the rest of the aneurysm. This implies that the spill in effect can potentially increase the SUV_{max} in the aneurysm by a factor of 1.12. However, when the aneurysm is in contact with the bone (Figure 5.4b), the maximum voxel value is 3.18 in the spill in prone area, and 2.05 in the rest of the aneurysm, resulting in a spill in factor of about 1.55.

Table 5.3: The analysis of the spill in effect as a result of application of post-filter and relative location of the aneurysm to the bone. This is done by extracting the SUV_{max} in the normal aneurysm area (A1) and in the spill in prone areas (A2) (close to the bone) with and without post-filter.

		3 mm post-filter			No post-filter		
		A1	A2	spill in factor ($\frac{A1}{A2}$)	A1	A2	spill in factor ($\frac{A1}{A2}$)
Case 1	OSEM	1.15	1.38	1.20	1.46	1.11	0.76
	PSF	1.54	1.73	1.12	1.22	1.26	1.03
	PSF+BC	1.56	0.80	0.51	1.24	0.46	0.37
Case 2	OSEM	1.73	2.68	1.55	1.66	4.24	2.55
	PSF	2.05	3.18	1.55	2.06	3.22	1.56
	PSF+BC	2.09	2.45	1.17	2.14	2.44	1.14

However, without the application of post-filter, the spill in factor is reduced when the aneurysm is detached from the bone (Figure 5.4c). For aneurysm attached to the bone ((Figure 5.4d), the spill-in factor is greatly increased for OSEM (from 1.55 to 2.55) and slightly for PSF (1.55 to 1.56). The reason for this behaviour might be because of noise interference which mostly affects the OSEM image.

5.4 Discussion

[^{18}F]-NaF PET imaging is currently being explored as a promising imaging biomarker for microcalcification in AAA. However, a confounding issue is the spill in contamination from the bone into the aneurysm. Therefore, this study has investigated the spill in effect in [^{18}F]-NaF PET imaging of the abdominal aortic aneurysms and how it changes with ROI selection. We also evaluated the performance of the background correction technique aimed at reducing the spill in effect.

For all the patient data involved in the study, there is a significant [^{18}F]-NaF uptake in the aneurysms, and for post-filtered images, the SUV_{max} in the

aneurysm obtained from PSF-reconstructed images is higher than that in OSEM images, and this is the case for 49 out of the 63 patients under review. But without post-filtering, OSEM images have higher SUV_{max} than PSF images. However, the regression analysis performed on all the reconstructed images showed that there is no significant correlation between [^{18}F]-NaF uptake and AAA diameter for all the reconstruction algorithms both with and without post-filtering (Figure 5.3). Similar studies were conducted with [^{18}F]-FDG PET (Reeps et al. [2008], Truijers et al. [2008], Barwick et al. [2014]) where no correlation was recorded between [^{18}F]-FDG PET uptake and aneurysm diameter. It was then concluded that PET uptake is a feature of both normal and aneurysmal aortic walls, and therefore not related to the aneurysm size. For example, a patient with a large aneurysm size (diameter 61 mm) showed a low SUV_{max} of 2.50 and he is still alive. However, three patients with the lowest aneurysm size (diameter 40-43 mm) showed a high uptake ($SUV_{max} > 4$). These patients died within a year of follow-up, still with their aneurysms intact. This suggests that [^{18}F]-NaF may have the ability to stratify high risk aneurysms even before rupture, as revealed by previous work published from results obtained from the SoFIA^3 study (Forsythe et al. [2018]). Therefore, better AAA disease prediction using [^{18}F]-NaF would be of great benefits for patients with high-risk aneurysms which size may be smaller than what the current guidelines may suggest (i.e. 55 mm).

Also, all reconstruction algorithms demonstrated a higher [^{18}F]-NaF uptake in the aneurysms than normal aorta, as illustrated in Figure 5.2. For filtered images, the mean SUV_{max} for the normal aorta is almost the same for all the algorithms, whereas for the aneurysm, the SUV_{max} is different for all the algorithms, with the PSF algorithm producing images with the highest SUV_{max}. The

paired t-test, conducted on the reconstruction algorithms, showed that there is a significant difference in AAA SUV_{max} between OSEM and PSF+BC, but not for OSEM versus PSF. There is also a statistically significant difference in the AAA SUV_{max} between the correction algorithms (i.e. PSF and PSF+BC). Apart from the uptake differences observed across the reconstruction algorithms, a statistically significant uptake difference was also noticed in the aneurysm when the ROIs were drawn differently (i.e. with AAA and AAA_{exc}). PSF and PSF+BC produced almost the same SUV_{max} in AAA_{exc}, but PSF produced the highest SUV_{max} in AAA, while PSF+BC produced the lowest. These higher values observed in PSF reconstructions might likely be due to the commonly reported Gibbs artefacts, resulting in an overshoot around the hot region (i.e. bone) (Rahmim et al. [2013], Nuyts [2015]). This led to a considerably higher value for AAA than AAA_{exc}, making it appear as though there is a higher spill in effect with PSF reconstruction. However, the background correction technique was not susceptible to this overestimation, thereby making the technique effective for spill in correction area of the aneurysm. For SUV_{max}, $cSUV_{max}$ and TBR_{max}, the difference in quantification between AAA and AAA_{exc} was statistically significant for OSEM and PSF, but not for PSF+BC (Table 5.1). Also, PSF+BC showed the least difference between AAA and AAA_{exc}, and it also had the least SD across all the quantification metrics used.

Again, it could be seen that when using AAA_{exc} with 3 mm post-filter, the % difference between aneurysm and normal aorta is within 70% for all algorithms, but there is a big disparity when quantifying with the AAA. This also leads to a major difference in the number of patients having a significant AAA uptake as shown in Table 5.2 (note that significant difference is defined as % Difference

$> 25\%$ (Dweck et al. [2012a], Joshi et al. [2014], McBride et al. [2016.]). With AAA_{exc}, about 84% (86% in PSF-based reconstructions) of the patients have significant uptake in the aneurysm, whereas with AAA, we have 94% in OSEM, 95% in PSF but only 87% in PSF+BC. But without post-filtering, the % number of patients having a significant AAA uptake is greatly reduced for PSF and PSF+BC, but it remains the same for OSEM images. Also, the resulting difference in the % number of significant AAA uptake when quantifying with AAA or AAA_{exc} with (or without) post-filtering is 10% (10%) for OSEM, 9% (3%) for PSF and 1% (1%) for PSF+BC.

This significant disparity between the two ROIs is partly due to the spill in effect emanating from the adjacent bone into the aneurysm, as demonstrated in Figure 5.4. This spill in effect varies in magnitude with the position of the aneurysm relative to the bone, as aneurysms in close contact with the bone are more susceptible to the spill in effects from the bone (SUV_{max} amplified by about 1.55) than aneurysms detached from the bone (SUV_{max} amplified by about 1.12). It then appears that a good option would be to exclude areas close to the bone during image analysis. However, the obvious challenge would be that a certain degree of potentially important physiological information might be lost from the excluded regions. This is because the posterior retroperitoneal rupture (rupture from the aneurysm site close to the bone) is the most common and which could be treated with early clinical intervention (Sakalihasan et al. [2005], Assar and Zarins [2009]). It could also be seen in the patient cases presented in Figure 5.1 that there are genuine CT signal and PET uptake in the posterior parts of the aneurysm which are distinct from spill in effect from the bone.

This spill in effect and the Gibbs artefacts in the PSF-reconstructed images

were considerably reduced when the images were analysed without post-filtering. PSF images have lower quantitative values than OSEM images, and the discrepancies in quantification between AAA and AAA_{exc} were significantly reduced (Tables 5.1 and 5.2). Therefore, a good option for reducing the spill in effect would also be to avoid post-filtering of the images, as previously validated in Akerele et al. [2018]. However, the challenge is the noise amplification in the reconstruction algorithms, which would inversely impact image contrast and quantification. This would be particularly challenging when using SUV_{max} for quantification, as this metric is more prone to noise.

5.5 Conclusion

This study has investigated the spill in effect in the [^{18}F]-NaF PET imaging of the AAA, and also evaluated the performance of the background correction (BC) technique in improving quantification and correcting for the spill in effect. This study showed that the spill in effects from the bone leads to overestimation of SUV_{max} in the aneurysm and this may adversely affect patient management and treatment decision. It has also been shown that the spill in effect is further influenced by the ROI selection especially when the aneurysm is adjacent to the active bone, in which case SUV_{max} in the aneurysm could be amplified by about a factor of 1.5. However, the background correction (BC) technique is effective in correcting for the spill in effect from the bone, thereby enhancing accurate quantification at the aneurysm. Since this method helps to artificially eliminate the activity from the bone and the consequent spill in effect, employing this technique will lead to a more accurate SUV_{max} quantification at the aneurysm.

Chapter 6

General Conclusion and Future Work

6.1 Summary

Despite the wide applicability of PET imaging in oncology, cardiology and neurology, its quantitative strength is often limited due to the partial volume effect. This effect is particularly challenging when imaging a region of interest close to an active region such as the urinary bladder, myocardium and the bone. The main objective of this thesis was to investigate the partial volume spill in effect and how it affects PET quantification in the regions of interest, as well as investigate the feasibility of the background correction technique in mitigating this effect. In the different chapters of the thesis, different issues have been addressed, including: investigation of the spill in effect using simulated and experimental phantoms as well as patient datasets; spill in correction with the proposed background correction technique; comparison of the background correction with other

novel techniques; and application of the background correction to a specific clinical application.

Following the overview and the theoretical background to the thesis in Chapters 1 and 2, Chapter 3 extensively investigated the effect of the spill in activity from hot regions on adjacent lesion quantification, as well as the improvement brought about by the background correction technique. This work revealed that lesions or tissues relatively close to hot regions (within 15-20 mm) are more prone to the spill in effect, causing reduced visibility and activity overestimation. The overestimation in lesion activity is considerably high at lower iterations but it gradually reduces as iteration increases. However, even at 30 iterations, the overestimation is still up to about 31% and 6% for SUV_{max} and SUV_{mean} respectively, indicating that the spill in effect is more pronounced in SUV_{max} than SUV_{mean}, and reduces over iteration. It might then appear that a natural solution to reducing the spill in effect is by increasing the iteration. However, this comes at the expense of reduced lesion contrast and increased noise, and the SUV_{max} is quite sensitive to noise. This partly explains why the SUV_{max} is more prone to the spill in effect. On the other hand, post-filtering the reconstructed images to reduce the noise will in turn aggravate the spill in effect, as the activity overestimation is doubled by the use of filtering. It was also shown that for lesions in close proximity to the hot region, PSF algorithm performed similar or even worse than the OSEM algorithm. This behaviour is possibly due to the commonly reported Gibbs artefacts, resulting in an overshoot around the hot region. However, improved quantification and better lesion contrast were achieved with the BC technique irrespective of the lesion size, lesion distance from the hot region, the activity in the hot region, or application of post-filter.

Chapter 4 systematically evaluated the performance of the BC technique in comparison with two novel correction techniques LP and HKEM using both simulated and experimental PET/MR phantom data as well as abdominal aortic aneurysm (AAA) PET/CT human patient data. In all the data, the results showed that the LP and HKEM techniques have improved lesion contrast and noise-reduction capabilities compared with OSEM, PSF and BC, but they could not successfully correct for the spill in effects in regions close to a hot background region as much as the BC technique. They are also sensitive to segmentation and ROI-induced errors resulting in a huge difference in SUVs when the ROIs were drawn slightly differently. However, the BC method was robust to segmentation and ROI-selection variability thus enhancing the accurate PET signal quantification in large varieties of target regions of interest close to a hot background region. Since the BC method could only correct for the spill in effect, while the other methods gave improved contrast and reduced noise, it was therefore stipulated that the performance of the BC method could be further enhanced by combining it with more advanced reconstruction methods. The combination effect was demonstrated using the simulated phantom (Table 4.2) as the RC of the BC method could potentially be increased from 35% to around 80%.

Chapter 5 specifically applied the BC technique to 65 sets of abdominal aortic aneurysm PET/CT human patient data with the intent of correcting for the spill in effect emanating from the bone into the aneurysm. The results showed a significantly higher uptake in the aneurysm compared to normal aorta. This uptake in the aneurysm is not related to the aneurysm diameter with and without BC correction. This is also in line with previous studies which showed that PET uptake is a feature of both aneurysm and normal aorta. However, there was

a significant difference in the aneurysm uptake with OSEM and PSF methods when the ROIs were drawn slightly differently. This uptake difference is partly due to the spill in effect from the bone into the aneurysm which affected mostly the posterior part of the aneurysm adjacent to the bone. This spill in effect might adversely affect patient management and treatment decision as the result showed a net difference of 10% and 9% with OSEM and PSF respectively in the number of patients having significant aneurysm uptake. However, the net difference is only 1% with the BC method. Also, this effect is dependent on the proximity of the aneurysm to the bone, as the SUV_{max} could be amplified by almost a factor of 1.5 for aneurysms almost attached to the bone, but only a factor of 1.1 for those detached from the bone. Thus, the study concluded that accurate quantification can be achieved in the aneurysm region using the BC technique irrespective of the proximity of the aneurysm to the bone, and the ROI delineation criteria.

In general, the background correction method has been shown to be appropriate for reliable quantification and diagnosis of regions near a hot region. In this project, the background correction technique has been shown to be applicable for two major clinical investigations, namely: indicative PET examination of the pelvic areas for infection, metastases and cancer; and in the [^{18}F]-NaF PET examination of patients with abdominal aortic aneurysm. However, this correction technique is not limited to the investigated clinical scenarios. It could potentially be applied to imaging of any high activity regions such as the brain, head and neck, myocardium, as well as bone.

6.2 Limitations

A major limitation of this work is that there is no TOF implementation, whereas the modelled GE and the Biograph PET/CT scanners support TOF. Although TOF has been shown to mitigate errors due to data inconsistency (Vandenberghe et al. [2016]), it is not yet certain if TOF implementation can sufficiently correct for spill in effect, especially for proximal lesions as shown in Chapter 3. However, this has recently been implemented in the STIR library (Efthimiou et al. [2019]), and it could be potentially included in future investigations.

Another limitation is the lack of detailed realistic simulations to model some effects such as positron range, non-collinearity, detector response, inter-crystal scattering etc. Furthermore, a crucial approximation is that an image-based position-invariant Gaussian blurring was modelled, and the same analytical model was used to simulate and reconstruct the data. Although this is helpful for investigating the performance of the algorithm, it would have been preferable to utilise Monte Carlo simulators. Nevertheless, these limitations do not cancel the relevance of the background correction method because acquired phantom and patient datasets were also utilised which demonstrated that the recently proposed background correction method successfully corrects for the background activity.

Also, a spatially-invariant model of the PSF was used in this work due to the complexities and computational demands associated with the use of a spatially-variant model. This might have limited the performance of the PSF algorithm in correcting for the spill in effect as the results clearly showed that PSF performed similarly to OSEM especially for proximal lesions. Although previous works have

reported similar behaviour between spatially-variant and spatially-invariant PSF models in terms of resolution, contrast and noise metrics (Teo et al. [2007], Alessio et al. [2010]), however, it is reasonable that a spatially-variant model of the PSF would improve the system resolution in the entire field of view. Therefore, it might be more appropriate to implement a realistic, spatially-variant PSF modelling.

6.3 Future Work

In this current work, the BC was implemented as a simple, yet effective, spill in correction technique which could be easily adopted for routine use in the clinic. Thus, the background contribution was estimated at the 3^{rd} iteration which is the most commonly employed iteration in clinical PET exams. However, the performance of the BC techniques could be further enhanced by optimizing its implementation parameters. Since the estimated background regions were quite active and large, it was reasonably expected that the background activity would have nearly converged after the 3^{rd} iteration. However, for smaller background regions, a higher number of iteration might be required to ensure an adequate convergence.

A natural extension of this work would be to validate the applicability of the BC technique with more relevant clinical datasets. It might also be required to perform more clinically-oriented method evaluation such as lesion detectability with receiver operating characteristics (ROC) analysis and inter-observer variability studies. Also for the clinical validation in chapter 5, the investigation was done with only baseline data, so the effect of spill in correction on the abil-

ity of [^{18}F]-NaF PET/CT to predict AAA disease progression was not studied. Therefore, follow-up datasets could potentially be included in future work.

Also, the clinical study involved the use of [^{18}F]-NaF PET/CT imaging where the background region (i.e. bone) was segmented from the CTAC image. The clinical translation of the BC technique might be challenging for [^{18}F]-NaF PET/MR imaging in terms of the anatomical segmentation of the bone. An alternative approach will then be to segment the bone from the PET image, but this will require a more careful implementation as the segmented bone might also include the spill in prone regios of the aneurysm. Therefore, another potential advantage of using the BC method could be in improving automated segmentation methods. Although segmentation is better carried out using anatomical images due to their better contrast, it has however been shown in Chapters 3 and 5 that the background correction technique enhances better lesion contrast and visibility, as it makes it easier to see the boundaries of the lesions of interest more clearly. Therefore, this suggests that an automatic or semi-automated segmentation may be more accurate if performed on background corrected PET images. It will also be interesting to carry out radiomic analysis study where the proposed background correction method is expected to offer a larger uptake area to evaluate its characteristics.

Throughout the thesis, it has been shown that the spill in effect is more pronounced in SUV_{max} than SUV_{mean}. So the use of SUV_{mean} might be considered for use in the clinic as opposed to the currently used SUV_{max}. However, the use of SUV_{mean} might not accurately reflect the functional distribution in an heterogeneous lesion such as the aneurysm where the activity in the most diseased part is considerably higher than the remaining parts. So a potential future direction

might be to introduce alternative SUV metrics such as the SUV_{50}, SUV_{70}, SUV_{90} which might be less sensitive to the spill in effect.

Chapter 7

Bibliography

M. Abella, A. M. Alessio, D. A. Mankoff, L. R. MacDonald, J. J. Vaquero, M. Desco, and P. E. Kinahan. Accuracy of CT-based attenuation correction in PET/CT bone imaging. *Physics in Medicine and Biology*, 57(9):2477–2490, 2012.

M. C. Adams, T. G. Turkington, J. M. Wilson, and T. Z. Wong. A systematic review of the factors affecting accuracy of SUV measurements. *American Journal of Roentgenology*, 195(2):310–320, 2010.

A. Afshar-Oromieh, U. Haberkorn, H. P. Schlemmer, M. Fenchel, M. Eder, M. Eisenhut, B. A. Hadaschik, A. Kopp-Schneider, and M. Rothke. Comparison of PET/CT and PET/MRI hybrid systems using a 68Ga-labelled PSMA ligand for the diagnosis of recurrent prostate cancer: initial experience. *European Journal of Nuclear Medicine and Molecular Imaging*, 41(5):887–897, 2014.

S. Ahn, S. G. Ross, E. Asma, J. Miao, X. Jin, L. Cheng, S. D. Wollenweber,

and R. M. Manjeshwar. Quantitative comparison of OSEM and penalized likelihood image reconstruction using relative difference penalties for clinical PET. *Physics in Medicine and Biology*, 60(15):5733–5751, 2015.

M. Akerele, P. Wadhwa, S. Vandenberghe, and C. Tsoumpas. Comparison of partial volume correction techniques for lesions near high activity regions. In *2017 IEEE Nuclear Science Symposium and Medical Imaging Conference (NSS/MIC), Atlanta, GA*, pages 1–7, 2017.

M. I. Akerele, D. Deidda, J. Cal-Gonzalez, N. A. Karakatsanis, and C. Tsoumpas. Improved correction techniques to compensate for partial volume and spill-in effects in PET. In *2018 IEEE Nuclear Science Symposium and Medical Imaging Conference Proceedings (NSS/MIC)*, pages 1–5, 2018.

M. I. Akerele, P. Wadhwa, J. Silva-Rodriguez, W. Hallett, and C. Tsoumpas. Validation of the physiological background correction method for the suppression of the spill-in effect near highly radioactive regions in positron emission tomography. *European Journal of Nuclear Medicine and Molecular Imaging Physics*, 5(1):34, 2018.

K. Z. Al-Nabhani, R. Syed, S. Michopoulou, J. Alkalbani, A. Afaq, E. Panagiotidis, C. Omeara, A. Groves, P. Ell, and J. Bomanji. Qualitative and quantitative comparison of PET/CT and PET/MR imaging in clinical practice. *Journal of Nuclear Medicine*, 55(1):88–94, 2014.

H. G. Alcorn, S. K. Wolfson, K. Sutton-Tyrrell, L. H. Kuller, and D. O'Leary. Risk factors for abdominal aortic aneurysms in older adults enrolled in the car-

diovascular health study. *Arteriosclerosis, Thrombosis and Vascular Biology*, 16(8):963–970, 1996.

A. M. Alessio, C. W. Stearns, S. Tong, S. G. Ross, S. Kohlmyer, A. Ganin, and P. Kinahan. Application and evaluation of a measured spatially variant system model for PET image reconstruction. *IEEE Transactions on Medical Imaging*, 29(3):938–49, 2010.

A. N. Assar and C. K. Zarins. Ruptured abdominal aortic aneurysm: a surgical emergency with many clinical presentations. *Postgraduate Medical Journal*, 85 (1003):268–273, 2009.

J. A. Aston, V. J. Cunningham, M.-C. Asselin, A. Hammers, A. C. Evans, and R. N. Gunn. Positron emission tomography partial volume correction: estimation and algorithms. *Journal of Cerebral Blood Flow & Metabolism*, 22(8): 1019–1034, 2002.

B. C. Auday. *Magill's Medical Guide*. Ipswich, Massachusetts : Salem Press, 8th edition, 2018.

N. Avril, S. Sassen, B. Schmalfeldt, J. Naehrig, S. Rutke S, W. A. Weber, M. Werner, H. Graeff, M. Schwaiger, and W. Kuhn. Prediction of response to neoadjuvant chemotherapy by sequential F-18-fluorodeoxyglucose positron emission tomography in patients with advanced-stage ovarian cancer. *Journal of Clinical Oncology*, 23(30):7445–7453, 2005.

M. R. Ay, M. Shirmohammad, S. Sarkar, A. Rahmim, and H. Zaidi. Comparative assessment of energy-mapping approaches in ct-based attenuation correction for PET. *Molecular Imaging Biology*, 13(1):187–198, 2011.

T. Bach-Gansmo, J. A. Dybvik, T. C. Adamsen, and A. Naum. Variation in urinary excretion of FDG, yet another uncertainty in quantitative PET. *Acta Radiologica Short Reports*, 1(8):1–3, 2012.

B. Bai, J. Bading, and P. S. Conti. Tumor quantification in clinical positron emission tomography. *Theranostics*, 3(10):787–801, 2013.

D. L. Bailey, J. S. Karp, and S. Surti. Physics and instrumentation in PET. In *Positron Emission Tomography*, chapter 2, pages 13–39. Springer, London, 2005.

M. Bartscher, U. Hilpert, J. Goebbels, and G. Weidemann. Enhancement and proof of accuracy of industrial computed tomography (CT) measurements. *CIRP Annals*, 56(1):495 – 498, 2007.

T. Barwick, O. Lyons, N. G. Mikhaeel, M. Waltham, and M. O'Doherty. 18F-FDG PET-CT uptake is a feature of both normal diameter and aneurysmal aortic wall and is not related to aneurysm size. *European Journal of Nuclear Medicine and Molecular Imaging*, 41(12):2310–2318, 2014.

M. Beheshti, S. Haim, R. Zakavi, M. Steinmair, P. Waldenberger, T. Kunit, M. Nader, W. Langsteger, and W. Loidl. Impact of 18F-choline PET/CT in prostate cancer patients with biochemical recurrence: influence of androgen deprivation therapy and correlation with PSA kinetics. *Journal of Nuclear Medicine*, 54(6):833–840, 2013.

J. W. Bellinge, R. J. Francis, K. Majeed, G. F. Watts, and C. J. Schultz. In search of the vulnerable patient or the vulnerable plaque: 18 F-sodium fluoride

positron emission tomography for cardiovascular risk stratification. *Journal of Nuclear Cardiology*, 25(5):1774–1783, 2018.

M. A. Belzunce, A. Mehranian, and A. J. Reader. Enhancement of partial volume correction in MR-guided PET image reconstruction by using MRI voxel sizes. *IEEE Transactions on Radiation and Plasma Medical Sciences*, 3(3):315–326, 2018.

S. Ben-Haim and P. Ell. 18F-FDG PET and PET/CT in the evaluation of cancer treatment response. *Journal of Nuclear Medicine*, 50(1):88–99, 2009.

T. Beyer, D. W. Townsend, and T. M. Blodgett. Dual-modality PET/CT tomography for clinical oncology. *The Quarterly Journal of Nuclear Medicine*, 46(1):24–34, 2002.

J. Bland, A. Mehranian, M. A. Belzunce, S. Ellis, C. J. McGinnity, A. Hammers, and A. J. Reader. MR-guided kernel EM reconstruction for reduced dose PET imaging. *IEEE Transactions on Radiation and Plasma Medical Sciences*, 2(3): 235–243, 2017.

J. Bland, M. Belzunce, S. Ellis, C. McGinnity, A. Hammers, and A. Reader. Spatially-compact MR-guided kernel EM for PET image reconstruction. *IEEE Transactions on Radiation and Plasma Medical Sciences*, 2(5):470–482, 2018.

F. Bloch. Nuclear induction. *Physical Review*, 70(7-8):460–474, 1946.

F. E. Boas and D. Fleischmann. CT artifacts: Causes and reduction techniques. *Imaging in Medicine*, 4(2):229–240, 2012.

R. Boellaard. Standards for PET image acquisition and quantitative data analysis. *Journal of Nuclear Medicine*, 50(supplement2):11S–20S, 2009.

K. Bouchelouche and P. Oehr. Positron emission tomography and positron emission tomography/computerised tomography of urological malignancies, an update review. *Journal of Urology*, 179(1):34–45, 2008.

A. Bromiley, A. Welch, F. Chilcott, S. Waikar, S. McCallum, M. Dodd, S. Craib, L. Schweiger, and P. Sharp. Attenuation correction in PET using consistency conditions and a three-dimensional template. *IEEE Transactions on Nuclear Science*, 48(4):1371–1377, 2001.

J. Cal-González, C. Tsoumpas, M. L. Lassen, S. Rasul, L. Koller, M. Hacker, K. Schäfers, and T. Beyer. Impact of motion compensation and partial volume correction for 18f-NaF PET/CT imaging of coronary plaque. *Physics in Medicine & Biology*, 63(1):015005, 2017.

J. Cal-Gonzalez, X. Li, D. Heber, I. Rausch, S. C. Moore, K. Schäfers, M. Hacker, and T. Beyer. Partial volume correction for improved PET quantification in 18F-NaF imaging of atherosclerotic plaques. *Journal of Nuclear Cardiology*, 25(5):1742–1756, 2018.

C. Capirci, L. Rampin, P. A. Erba, F. Galeotti, G. Crepaldi, E. Banti, M. Gava, S. Fanti, G. Mariani, P. Muzzio, and D. Rubello. Sequential FDG-PET/CT reliably predicts response of locally advanced rectal cancer to neo-adjuvant chemo-radiation therapy. *European Journal of Nuclear Medicine Molecular Imaging*, 34(10):1583–1593, 2007.

M. F. Di Carli and S. Dorbala. Cardiac PET-CT. *Journal of Thoracic Imaging*, 22(1):101–106, 2007.

G. L. Cascini, A. Avallone, P. Delrio, C. Guida, F. Tatangelo, P. Marone, L. Aloj, F. De Martinis, P. Comella, V. Parisi, and S. Lastoria. 18F-FDG PET is an early predictor of pathologic tumor response to preoperative radiochemotherapy in locally advanced rectal cancer. *Journal of Nuclear Medicine*, 47(8): 1241–1248, 2006.

W. Chen and V. Dilsizian. PET assessment of vascular inflammation and atherosclerotic plaques: SUV or TBR? *Journal of Nuclear Medicine*, 56(4): 503–504, 2015.

S. R. Cherry. Multimodality imaging: beyond PET/CT and SPECT/CT. *Seminars in Nuclear Medicine*, 39(5):348–353, 2009.

S. R. Cherry, T. L. Jones, J. S. Karp, J. Qi, W. W. Moses, and R. D. Badawi. Total-body PET: Maximizing sensitivity to create new opportunities for clinical research and patient care. *Journal of nuclear medicine*, 59(1):3–12, 2018.

S. Chondrogiannis, M. Marzola, G. Grasseto, A. Maffione, L. Rampin, A. Massaro E. Veronese, and D. Rubello. New acquisition protocol of 18F-Choline PET/CT in prostate cancer patients: review of the literature about methodology and proposal of standardization. *BioMed Research International*, 2014: 215650, 2014.

S. Y. Chun, T. G. Reese, J. Ouyang, B. Guerin, C. Catana, X. Zhu, N. Alpert, and G. Fakhri. MRI-based nonrigid motion correction in simultaneous PET/MRI. *Journal of Nuclear Medicine*, 53(8):1284–1291, 2012.

M. S. Cocker, B. Mc Ardle, J. D. Spence, C. Lum, R. Hammond, D. Ongaro, M. McDonald, R. DeKemp, J-C. Tardif, and R. Beanlands. Imaging atherosclerosis with hybrid [18F]fluorodeoxyglucose positron emission tomography/computed tomography imaging: What leonardo da vinci could not see. *Journal of Nuclear Cardiology*, 19(6):1211–1225, 2012.

C. Cohade, M. Osman, H. K. Pannu, and R. L. Wahl. Uptake in supraclavicular area fat ("USA-Fat"): description on 18F-FDG PET/CT. *Journal of Nuclear Medicine*, 44(2):170–176, 2003.

A. M. Cormack. Representation of a function by its line integrals, with some radiological applications. *Journal of Applied Physics*, 34(9):2722–2727, 1963.

M. C. F. Cysouw, G. M. Kramer, L. J. Schoonmade, R. Boellaard, H. C. W. de Vet, and O. S. Hoekstra. Impact of partial volume correction in oncological PET studies: a systematic review and meta-analysis. *European Journal of Nuclear Medicine and Molecular Imaging*, 44(12):2105–2116, 2017.

D. Deidda, N. A. Karakatsanis, P. M. Robson, C. Calcagno, M. L. Senders, W. J. M Mulder, Z. A. Fayad, R. G. Aykroyd, and C. Tsoumpas. Hybrid PET/MR kernelised expectation maximisation reconstruction for improved image-derived estimation of the input function from the aorta of rabbits. *Contrast Media and Molecular Imaging*, 2019:3438093, 2019a.

D. Deidda, N. A. Karakatsanis, P. M. Robson, N. Efthimiou, Z. A. Fayad, R. G. Aykroyd, and C. Tsoumpas. Effect of PET-MR inconsistency in the kernel image reconstruction method. *IEEE Transactions on Radiation and Plasma Medical Sciences*, 3(4):400–409, 2019b.

D. Deidda, N. A. Karakatsanis, P. M. Robson, Y. Tsai, N. Efthimiou, K. Thielemans, Z. A. Fayad, R. G. Aykroyd, and C. Tsoumpas. Hybrid PET-MR list-mode kernelized expectation maximization reconstruction. *Inverse Problems*, 35(4):044001, 2019c.

G. Delso, S. Furst, B. Jakoby, R. Ladebeck, C. Ganter, S. G. Nekolla, M. Schwaiger, and S. I. Ziegler. Performance measurements of the Siemens mMR integrated whole-body PET/MR scanner. *Journal of Nuclear Medicine*, 52(12):1914–1922, 2011.

G. Delso, B. Kemp, S. Kaushik, F. Wiesinger, and T. Sekine. Improving PET/MR brain quantitation with template-enhanced ZTE. *NeuroImage*, 181: 403–413, 2018.

S. E. Derenzo, T. F. Budinger, R. H. Huesman, and J. L. Cahoon. Dynamic positron-emission tomography in man using small bismuth germanate crystals. In *The Sixth International Conference on Positron Annihilation; Ft. Worth, TX*, page 1–11, 1982.

J. A. Disselhorst, I. Bezrukov, A. Kolb, C. Parl, and B. J. Pichler. Principles of PET/MR imaging. *Journal of Nuclear Medicine*, 55(Supplement 2):2S–10S, 2014.

Y. Du, I. Mada, M. J. Stumpf, X. Rong, G. S. K. Fung, and E. C. Frey. Compensation for spill-in and spill-out partial volume effects in cardiac PET imaging. *Journal of Nuclear Cardiology*, 20(1):84–98, 2013.

M. R. Dweck, M. W. L. Chow, N. V. Joshi, Fletcher AM Williams MC, Jones C, H. Richardson, A. White, G. McKillop, E. J. R. van Beek, N. A. Boon, J. H. F.

Rudd, and D. E. Newby. Coronary arterial 18F-sodium fluoride uptake: A novel marker of plaque biology. *Journal of the American College of Cardiology*, 59(17):1539–1548, 2012a.

M. R. Dweck, C. Jones, N. V. Joshi, A. M. Fletcher, H. Richardson, A. White, M. Marsden, R. Pessotto, J. C. Clark, W. A. Wallace, D. M. Salter, G. Mckillop, E. J. van Beek, N. A. Boon, J. H. Rudd, and D. E. Newby. Assessment of valvular calcification and inflammation by positron emission tomography in patients with aortic stenosis. *Circulation*, 125(1):76–86, 2012b.

M. R. Dweck, W. S. A. Jenkins, A. T. Vesey, M. A. H. Pringle, C. W. L. Chin, T. S. Malley, W. Cowie, V. Tsampasian, H. Richardson, A. Fletcher, W. A. Wallace, R. Pessotto, E. Beek, N. Boon, J. Rudd, and D. E. Newby. 18F-NaF uptake is a marker of active calcification and disease progression in patients with aortic stenosis. *Circulation. Cardiovascular imaging*, 7(2):371–378, 2014.

N. Efthimiou, E. Emond, P. Wadhwa, C. Cawthorne, C. Tsoumpas, and K. Thielemans. Implementation and validation of time-of-flight PET image reconstruction module for listmode and sinogram projection data in the STIR library. *Physics in Medicine and Biology*, 64(3):035004, 2019.

M. J. Ehrhardt, P. Markiewicz, M. Liljeroth, A. Barnes, V. Kolehmainen, J. S. Duncan, L. Pizarro, D. Atkinson, B. F. Hutton, S. Ourselin, K. Thielemans, and S. R. Arridge. PET reconstruction with an anatomical MRI prior using parallel level sets. *IEEE Transactions on Medical Imaging*, 35(9):2189–2199, 2016.

P. J. Ell and G. K. von Schulthess. PET/CT: a new road map. *European Journal of Nuclear Medicine and Molecular Imaging*, 29(6):719–720, 2002.

F. H. Fahey. Data acquisition in PET imaging. *Journal of Nuclear Medicine Technology*, 30(2):39–49, 2002.

M. J. V. Ferreira, M. Oliveira-Santos, R. Silva, A. Gomes, N. Ferreira, A. Abrunhosa, J. Lima, M. Pego, L. Gonçalves, and M. Castelo-Branco. Assessment of atherosclerotic plaque calcification using F18-NaF PET-CT. *Journal of Nuclear Cardiology*, 25(5):1733–1741, 2018.

V. Filippou and C. Tsoumpas. Recent advances on the development of phantoms using 3D printing for imaging with CT, MRI, PET, SPECT, and ultrasound. *Medical Physics*, 45(9):e740–e760, 2018.

F. Foroudi, M. Bressel D. Pham, S. Gill, and T. Kron. Intrafraction bladder motion in radiation therapy estimated from pretreatment and posttreatment volumetric imaging. *International Journal of Radiation Oncology Biology Physics*, 86(1):77–82, 2013.

R. O. Forsythe, D. E. Newby, and J. M. J. Robson. Monitoring the biological activity of abdominal aortic aneurysms beyond ultrasound. *Heart*, 102(11): 817–824, 2016.

R. O. Forsythe, M. R. Dweck, O. M. B. McBride, A. T. Vesey, S. I. Semple, A. S. V. Shah, P. Adamson, W. A. Wallace, J. Kaczynski, W. Ho, E. Beek, C. Gray, A. Fletcher, C. Lucatelli, A. Marin, P. Burns, and R. Chalmers A. Tambyraja, G. Weir, and D. E. Newby. 18F-sodium fluoride uptake in

abdominal aortic aneurysms: The SOFIA3 study. *Journal of the American College of Cardiology*, 71(5):513–523, 2018.

E. C. Frey, J. L. Humm, and M. Ljungberg. Accuracy and precision of radioactivity quantification in nuclear medicine images. *Seminar in Nuclear Medicine*, 42(3):208–218, 2012.

V. Frouin, C. Comtat, A. Reilhac, and M. C. Gregoire. Correction of partial-volume effect for PET striatal imaging: fast implementation and study of robustness. *Journal of Nuclear Medicine*, 43(12):1715–1726, 2002.

F. C. Gaertner, A. J. Beer, M. Souvatzoglou, M. Eiber, S. Furst, S. I. Ziegler, F. Brohl, M. Schwaiger, and K. Scheidhauer. Evaluation of feasibility and image quality of 68Ga-DOTATOC positron emission tomography/magnetic resonance in comparison with positron emission tomography/computed tomography in patients with neuroendocrine tumors. *Investigative Radiology*, 48 (5):263–272, 2013.

K. Getliffe and M. Dolman. *Promoting Continence: A Clinical and Research Resource*. Elsevier Health Sciences, 2007.

L. Geworski, B. O. Knoop, M. L. de Cabrejas, W. H. Knapp, and D. L. Munz. Recovery correction for quantitation in emission tomography: a feasibility study. *European Journal of Nuclear Medicine*, 27(2):161–169, 2000.

E. González, J. Cui, G. Pratx, M. Bieniosek, P. D. Olcott, and C. S. Levin. Point spread function for PET detectors based on the probability density function of the line segment. In *2011 IEEE Nuclear Science Symposium Conference Record*, pages 4386–4389, 2011.

A. M. Grant, T. W. Deller, M. M. Khalighi, S. H. Maramraju, G. Delso, and C. S. Levin. NEMA NU 2-2012 performance studies for the SiPM-based ToF-PET component of the GE SIGNA PET/MR system. *Medical Physics*, 43(5): 2334–2343, 2016.

C. Grønborg, A. Vestergaard, M. Høyer, M. Söhn, E. M. Pedersen, J. B. Petersen, M. Agerbaek, and L. Muren. Intra-fractional bladder motion and margins in adaptive radiotherapy for urinary bladder cancer. *Acta Oncologica*, 54(9): 1461–1466, 2015.

J. G. Guillem, H. G. Moore, T. Akhurst, D. S. Klimstra, L. Ruo, M. Mazumdar, B. D. Minsky, L. Saltz, W. D. Wong, and S. Larson. Sequential preoperative fluorodeoxyglucose-positron emission tomography assessment of response to preoperative chemoradiation: a means for determining longterm outcomes of rectal cancer. *Journal of the American College of Surgeons*, 199(1):1–7, 2004.

J. Hamill and T. Bruckbauer. Iterative reconstruction methods for high-throughput PET tomographs. *Physics in Medicine and Biology*, 47(15):2627, 2002.

N. Hawkes. Cancer survival data emphasise importance of early diagnosis. *BMJ*, 364:l408, 2019.

S. I. Heiba, B. Raphael, I. Castellon, E. Altinyay, N. Sandella, G. Rosen, and H. M. Abdel-Dayem. PET/CT image fusion error due to urinary bladder filling changes: consequence and correction. *Annals of Nuclear Medicine*, 23 (6):739–744, 2009.

G. T. Herman. *Fundamentals of Computerized Tomography: Image Reconstruc-*

tion from Projections. Springer Publishing Company, Incorporated, 2nd edition, 2009.

T. Heuber, P. Mann, C. M. Rank, M. Schafer, A. Dimitrakopoulou-Strauss, H-P. Schlemmer, B. Hadaschik, K. Kopka, P. Bachert, M. Kachelrieb, and M. Freitag. Investigation of the halo-artifact in 68Ga-PSMA-11-PET/MRI. *PloS ONE*, 12(8):e01833329, 2017.

R. Hicks, E. Lau, and D. Binns. Hybrid imaging is the future of molecular imaging. *Biomedical Imaging and Intervention Journal*, 3(3):e49, 2007.

C. J. Hoekstra, I. Paglianiti, O. S. Hoekstra, E. F. Smit, P. E. Postmus, G. J. J. Teule, and A. A. Lammertsma. Monitoring response to therapy in cancer using F-18 -2-Fluoro-2-Deoxy-D-Glucose and positron emission tomography: An overview of different analytical methods. *European Journal of Nuclear Medicine*, 27(6):731–743, 2000.

C. J. Hoekstra, O. S. Hoekstra, S. G. Stroobants, J. Vansteenkiste, J. Nuyts, E. F. Smit, M. Boers, J. W. R. Twisk, and A. A. Lammertsma. Methods to monitor response to chemotherapy in non-small cell lung cancer with F-18-FDG PET. *Journal of Nuclear Medicine*, 43(10):1304–1309, 2002.

F. Hofheinz, J. Langner, J. Petr, B. Beuthien-Baumann, L. Oehme, J. Steinbach, J. Kotzerke, and J. Hoff. A method for model-free partial volume correction in oncological PET. *European Journal of Nuclear Medicine and Molecular Imaging Research*, 2(1):16, 2012.

M. Hofmann, I. Bezrukov, F. Mantlik, P. Aschoff, F. Steinke, T. Beyer, B. J. Pichler, and B. Scholkopf. MRI-based attenuation correction for whole-body

PET/MRI: quantitative evaluation of segmentation-and atlas-based methods. *Journal of Nuclear Medicine*, 52(9):1392–1399, 2011.

D. Hogg, K. Thielemans, T. Spinks, and N. Spyrou. Maximum-likelihood estimation of normalisation factors for PET. In *IEEE Nuclear Science Symposium and Medical Imaging Conference Record*, volume 4, pages 2065–2069, 2001.

C. K. Hoh. Clinical use of FDG PET. *Nuclear Medicine and Biology*, 34(7): 737–742, 2007.

J. W. Hole. *Human Anatomy and Physiology*. Dubuque, IA: WCB, 2nd edition, 1981.

H. Hong, Y. Yang, B. Liu, and W. Cai. Imaging of abdominal aortic aneurysm: the present and the future. *Current Vascular Pharmacology*, 8(6):808–819, 2010.

G. N. Hounsfield. Computerized transverse axial scanning (tomography). part 1. description of system. *The British Journal of Radiology*, 46(552):1016–1022, 1973.

J. Hsieh. Image artifacts: Appearances, causes, and corrections. In Jiang Hsieh, editor, *Computed Tomography: Principles, Design, Artifacts, and Recent Advances*, pages 245–338. Belligham: SPIE, 3rd edition, 2015.

H. Hudson and R. Larkin. Accelerated image reconstruction using ordered subsets of projected data. *IEEE Transactions on Medical Imaging*, 13(4):601–609, 1994.

B. F. Hutton, B. A. Thomas, A. Bousse K. Erlandsson, A. Reilhac-Laborde, D. Kazantsev, S. Pedemonte, K. Vunckx, S. R. Arridge, and S. Ourselin. What approach to brain partial volume correction is best for PET/MRI? *Nuclear Instruments and Methods in Physics Research Section A*, 702:29–33, 2013.

A. Irkle, A. T. Vesey, D. Y. Lewis, J. N. Skepper, J. L. E. Bird, M. R. Dweck, F. R. Joshi, F. A. Gallagher, E. A. Warburton, M. R. Bennett, K. M. Brindle, D. E. Newby, J. H. Rudd, and A. P. Davenport. Identifying active vascular micro-calcification by 18F-sodium fluoride positron emission tomography. *Nature Communications*, 6(7495):1–11, 2015.

T. Janssen, P. Bannas, J. Herrmann, S. Veldhoen, J. D. Busch, A. Treszl, and J. Mester S. Münster, and T. Derlin. Association of linear 18F-sodium fluoride accumulation in femoral arteries as a measure of diffuse calcification with cardiovascular risk factors: A PET/CT study. *Journal of Nuclear Cardiology*, 20(4):569–577, 2013.

K. Johansen and T. Koepsell. Familial tendency for abdominal aortic aneurysms. *Journal of American Medical Association*, 256(14):1934–1936, 1986.

K. A. Johnson, S. Minoshima, N. I. Bohnen, K. J. Donohoe, N. L. Foster, P. Herscovitch, J. H. Karlawish, C. C. Rowe, M. C. Carrillo, D. M. Hartley, S. Hedrick, V. Pappas, and W. H. Thies. Appropriate use criteria for amyloid PET: A report of the amyloid imaging task force, the society of nuclear medicine and molecular imaging, and the alzheimer's association. *Alzheimer's dementia : the journal of the Alzheimer's Association*, 9(1):E1–E16, 2013.

N. V. Joshi, A. T. Vesey, M. C. Williams, F. H. M. Craighead A. S. V. Shah,

P. A. Calvert, S. E. Yeoh, W. Wallace, D. Salter, Alison M Fletcher, E. J. R. van Beek, A. D. Flapan, N. G. Uren, M. W. H. Behan, N. L. M. Cruden, N. L. Mills, K. A. A. Fox, J. H. F. Rudd, M. R. Dweck, and D. E. Newby. 18F-fluoride positron emission tomography for identification of ruptured and high-risk coronary atherosclerotic plaques: a prospective clinical trial. *Lancet*, 383(9918):705–713, 2014.

L. Jødal, C. Le Loirec, and C. Champion. Positron range in PET imaging: An alternative approach for assessing and correcting the blurring. *Physics in Medicine and Biology*, 57(12):3931–3943, 2012.

W. A. Kalender. X-ray computed tomography. *Physics in Medicine and Biology*, 51(13):29–43, 2006.

N. Karakatsanis, P. Robson, M. Dweck, R. Abgral, M. Trivieri, J. Sanz, J. Contreras, J. Narula, M. Padilla, U. Gidwani, V. Fuster, J. Kovacic, and Z. Fayad. MR-based attenuation correction in cardiovascular PET/MR imaging: challenges and practical solutions for cardiorespiratory motion and tissue class segmentation. *Journal of Nuclear Medicine*, 57(2):452, 2016.

A. M. Karlberg, O. Saether, L. Eikenes, and P. E. Goa. Quantitative comparison of PET performance-siemens biograph mCT and mMR. *European Journal of Nuclear Medicine and Molecular Imaging Physics*, 3(1):5, 2016.

J. S. Karp, G. Muehllehner, D. A. Mankoff, C. E. Ordonez, J. M. Ollinger, M. E. Daube-Witherspoon, A. T. Haigh, and D. J. Beerbohm. Continuous-slice PENN-PET: a positron tomograph with volume imaging capability. *Journal of Nuclear Medicine*, 31(5):617–627, 1990.

P. E. Kinahan and J. W. Fletcher. Positron emission tomography-computed tomography standardized uptake values in clinical practice and assessing response to therapy. *Seminars in Ultrasound, CT, and MR*, 31(6):496–505, 2010.

P. E. Kinahan, L. MacDonald, L. Ng, A. Alessio, P. Segars, B. Tsui, and S. Pathak. Compensating for patient respiration in PET/CT imaging with the registered and summed phases (RASP) procedure. In *3rd IEEE International Symposium on Biomedical Imaging: Nano to Macro. Arlington, VA*, page 1104–1107. IEEE, 2006.

P.E Kinahan, B. H. Hasegawa, and T. Beyer. X-ray-based attenuation correction for positron emission tomography/computed tomography scanners. *Seminar in Nuclear Medicine*, 33(3):166–179, 2003.

O. Klein and Y. Nishina. On the scattering of radiation by free electrons according to dirac's new relativistic quantum dynamics. In *The Oskar Klein Memorial Lectures by Hans A. Bethe and Alan H. Guth with Translated Reprints by Oskar Klein*, volume 2, page 113–139. World Scientific Publishing Co. Pte. Ltd., Singapore, 1994.

A. Kolb, A. W. Sauter, L. Eriksson, A. Vandenbrouke, C. C. Liu, C. Levin, B. Pichler, and M. Rafecas. Shine-through in PET/MR imaging: Effects of the magnetic field on positron range and subsequent image artifacts. *Journal of Nuclear Medicine*, 56(6):951–954, 2015.

S. Kosuda, S. Fisher, and R. L. Wahl. Animal studies on the reduction and/or dilution of 2-deoxy-2- 18F fluoro-d-glucose (FDG) activity in the urinary system. *Annals of Nuclear Medicine*, 11(3):213–218, 1997.

K. Koyama, T. Okamura, M. Miyama, H. Ochi, and R. Yamada. Evaluation of 18F-FDG PET with bladder irrigation in patients with uterine and ovarian tumors. *Journal of Nuclear Medicine*, 44(3):353–358, 2003.

H. Kurvers, F. J. Veith, E. C. Lipsitz, O. Toshiyuki, J. G. Nicholas, S. C. Neal, D. S. William, H. T. Carlos, Y. K. Grace, J. R. Soo, and A. C. S. Christian. Discontinuous, staccato growth of abdominal aortic aneurysms. *Journal of the American College of Surgeons*, 199(5):709–715, 2004.

C. Labbe, H. Zaidi, C. Morel, K. Thielemans, and C. Tsoumpas. *Glossary for STIR*, volume 2.3. 2012.

K. Lange and R. Carson. EM reconstruction algorithms for emission and transmission tomography. *Journal of Computer Assisted Tomography*, 8(2):306–316, 1984.

H. Lee, J. C. Paeng, K. H. Kim, G. J. Cheon, D. Lee, J-K. Chung, and K. Kang. Correlation of FDG PET/CT findings with long-term growth and clinical course of abdominal aortic aneurysm. *Nuclear Medicine and Molecular Imaging*, 52(1):46–52, 2018.

S. W. Lee and J. H. Kim. The significance of natural bladder filling by the production of urine during cystometry. *Neurourology Urodynamics*, 27(8):772–774, 2008.

C. S. Levin, H. Maramraju, M. M. Khalighi, T. W. Deller, G. Delso, and F. Jansen. Design features and mutual compatibility studies of the time-of-flight PET capable GE SIGNA PET/MRI system. *IEEE Transactions on Medical Imaging*, 35(8):1907–1914, 2016.

Z-P. Liang and P. C. Lauterbur. *Principles of Magnetic Resonance Imaging: A Signal Processing Perspective*. New York: Wiley–IEEE Press, 1999.

J. H. N. Lindeman, H. Abdul-Hussien, A. F. M. Schaapherder, J. Bockel, J. von der Thüsen, D. Roelen, and R. Kleemann. Enhanced expression and activation of pro-inflammatory transcription factors distinguish aneurysmal from atherosclerotic aorta: IL-6- and IL-8-dominated inflammatory responses prevail in the human aneurysm. *Clinical Science*, 114(11)):687–697, 2008.

G. Liney. *MRI in Clinical Practice*. Springer Science & Business Media, 2007.

M. L. Lipton. *Totally Accessible MRI: A User's Guide to Principles, Technology, and Applications*. New York: Springer, 2008.

C. Liu, L. A. Pierce, A. M. Alessio, and P. E. Kinahan. The impact of respiratory motion on tumor quantification and delineation in static PET/CT imaging. *Physics in Medicine and Biology*, 54(24):7345–7362, 2009.

F. Liu, H. Jang, R. Kijowski, T. Bradshaw, and A. B. McMillan. Deep learning MR imaging–based attenuation correction for PET/MR imaging. *Radiology*, 286(2):676–684, 2017.

Y. Liu. Invalidity of SUV measurements of lesions in close proximity to hot sources due to shine-through effect on FDG PET-CT interpretation. *Radiology Research and Practice*, 2012(868218):1–4, 2012.

E. Lo, L. Nicolle, S. Coffin, C. Gould, L. Maragakis, J. Meddings, D. Pegues, A. Pettis, S. Saint, and S. Yokoe. Strategies to prevent catheter-associated urinary tract infections in acute care hospitals: 2014 update. *Infection Control and Hospital Epidemiology*, 35(5):464–479, 2014.

M. E. Lyra and A. Ploussi. Filtering in SPECT image reconstruction. *International Journal of Biomedical Imaging*, 2011(693795):693795, 2011.

B. J. Malm and M. M. Sadeghi. Multi-modality molecular imaging of aortic aneurysms. *Journal of Nuclear Cardiology*, 24(4):1239–1245, 2017.

A. Martinez-Moller, M. Souvatzoglou, G. Delso, R. A. Bundschuh, S. Ziegler, N. Navab, M. Schwaiger, and S. Nekolla. Tissue classification as a potential approach for attenuation correction in whole-body PET/MRI: evaluation with PET/CT data. *Journal of Nuclear Medicine*, 50(4):520–526, 2009.

A. Massaro, A. Ferreti, C. Secchiero, S. Cittadin, E. Milan, L. Tamiso, L. Pavan, E. Tommasi, M. Marzola, S. Chondrogiannis, L. Rampin, A. Marcolongo, and D. Rubello. Optimising 18F-Choline PET/CT acquisition protocol in prostate cancer patients. *North American Journal of Medical Sciences*, 4(9):416–420, 2012.

S. Mastrogiacomo, W. Dou, J. A. Jansen, and X. F. Walboomers. Magnetic resonance imaging of hard tissues and hard tissue engineered bio-substitutes. *Molecular Imaging and Biology*, Epub ahead of print, 2019.

O. M. B. McBride, N. V. Joshi, J. M. J. Robson, T. J. Macgillivray, C. D. Gray, A. M. Fletcher, M. R. Dweck, E. J. van Beek, J. H. Rudd, D. E. Newby, and S. I. Semple. Positron emission tomography and magnetic resonance imaging of cellular inflammation in patients with abdominal aortic aneurysms. *European Journal of Vascular and Endovascular Surgery*, 51(4):518–526, 2016.

D. W. McRobbie, E. A. Moore, M. J. Graves, and M. R. Prince. *MRI: From Picture to Proton*. Cambridge University Press, 3rd edition, 2017.

A. Mehranian and H. Zaidi. Emission-based estimation of lung attenuation coefficients for attenuation correction in time-of-flight PET/MR. *Physics in Medicine and Biology*, 60(12):4813–4833, 2015.

C. C. Meltzer, J. P. Leal, H. S. Mayberg, H. N. Wagner(Jr), and J. J. Frost. Correction of PET data for partial volume effects in human cerebral cortex by MR imaging. *Journal of Computer Assisted Tomography*, 14(4):561–570, 1990.

D. Metcalfe, P. J. E. Holt, and M. M. Thompson. The management of abdominal aortic aneurysms. *BMJ*, 342:d1384, 2011.

F. A. Mettler Jr and M. J. Guiberteau. *Essentials of Nuclear Medicine Imaging: Expert Consult-Online and Print*. Elsevier Health Sciences, 6th edition, 2012.

C. Michel, M. Sibomana, A. Bol, X. Bernard, M. Lonneux, M. Defrise, C. Comtat, P. Kinahan, and D. W. Townsend. Preserving poisson characteristics of PET data with weighted OSEM reconstruction. In *IEEE Nuclear Science Symposium and Medical Imaging Conference; Toronto*, pages 1323–1329, 1998.

S. C. Moore, S. Southekal, M. Park, S. J. Mcquaid, M. F. Kijewski, and S. P. Muller. Improved regional activity quantification in nuclear medicine using a new approach to correct for tissue partial volume and spillover effects. *IEEE Transactions on Medical Imaging*, 31(2):405–416, 2012.

J. K. Moran, H. B. Lee, and M. D. Blaufox. Optimization of urinary FDG excretion during PET imaging. *Journal of Nuclear Medicine*, 40(8):1352–1357, 1999.

H. W. Muller-Gartner, J. M. Links, R. N. Bryan J. L. Prince, E. McVeigh, J. P. Leal, C. Davatzikos, and J. J. Frost. Measurement of radiotracer concentration in brain gray matter using positron emission tomography: MRI-based correction for partial volume effects. *Journal of Cerebral Blood Flow & Metabolism*, 12(4):571–583, 1992.

O. L. Munk, L. P. Tolbod, S. B. Hansen, and T. V. Bogsrud. Point-spread function reconstructed PET images of sub-centimeter lesions are not quantitative. *European Journal of Nuclear Medicine and Molecular Imaging Physics*, 4:5, 2017.

S. Musafargani, K. K. Ghosh, S. Mishra, P. Mahalakshmi, P. Padmanabhan, and B. Guly. PET/MRI: a frontier in era of complementary hybrid imaging. *European Journal of Hybrid Imaging*, 2(1):12–39, 2018.

C. Nahmias and L. M. Wahl. Reproducibility of standardized uptake value measurements determined by 18F-FDG PET in malignant tumors. *Journal of Nuclear Medicine*, 49(11):1804–1808, 2008.

I. El Naqa, P. Gribsby, A. Apte, E. Kidd, S. Chaudhari, D. Yang, and J. Deasy. Beyond SUV: new methods for assessing treatment response in PET images. *Medical Physics*, 34:2333, 2007.

S. A. Nehmeh and Y. E. Erdi. Respiratory motion in positron emission tomography/computed tomography: A review. *Seminar in Nuclear Medicine*, 38(3): 167–176, 2008.

S. A. Nehmeh, Y. E. Erdi, T. Pan, A. Pevsner, K. E. Rosenzweig, E. Yorke, G. S. Mageras, H. Schoder, P. Vernon, O. Squire, H. Mostafavi, S. M. Larson, and

J. L. Humm. Four-dimensional (4D) PET/CT imaging of the thorax. *Medical Physics*, 31(12):3179–3186, 2004.

Y. Nishiyama, Y. Yamamoto, K. Kanenishi, Ohno M, Hata T, Kushida Y, Haba R, and Ohkawa M. Monitoring the neoadjuvant therapy response in gynecological cancer patients using FDG PET. *European Journal of Nuclear Medicine and Molecular Imaging*, 35(2):287–295, 2008.

J. Nuyts. Unconstrained image reconstruction with resolution modelling does not have a unique solution. *European Journal of Nuclear Medicine and Molecular Imaging Physics*, 1(1):98, 2015.

J. Nuyts, B. De Man, J. Fessler, W. Zbijewski, and F. Beekman. Modelling the physics in the iterative reconstruction for transmission computed tomography. *Physics in Medicine and Biology*, 58(12):R63–R96, 2013.

M. M. Osman, C. Cohade, Y. Nakamoto, L. T. Marshall, J. P. Leal, and R. L. Wahl. Clinically significant inaccurate localization of lesions with PET/CT: frequency in 300 patients. *Journal of Nuclear Medicine*, 44(2):240–243, 2003.

S. H. Park, M-J. Kim, J. H. Kim, A. E-H. Cho, M-S. Park, and K. W. Kim. FDG uptake in PET by bladder hernia simulating inguinal metastasis. *Yonsei Medical Journal*, 48(5):886–890, 2007.

T. A. Pawade, T. R. G. Cartlidge, W. S. A. Jenkins, P. D. Adamson, P. Robson, C. Lucatelli, and B. Prendergast E. Beek, and L. Forsyth A. R. Denison, J. H. F. Rudd, Z. A. Fayad, A. Fletcher, S. Tuck, D. E. Newby, and M. R. Dweck. Optimization and reproducibility of aortic valve 18F-fluoride positron

emission tomography in patients with aortic stenosis. *Circulation and Cardiovascular Imaging*, 9(10):e005131, 2016.

E. Pelosi, A. Skanjeti, and P. Scapoli. Improved diagnosis of pelvic lesions with dual-phase (18F)FDG-PET/CT. *Radiology Case Report*, 6(1):149, 2011.

D. L. Pham, C. Y. Xu, and J. L. Prince. Current methods in medical image segmentation. *Annual Review of Biomedical Engineering*, 2:315–337, 2000.

J. Pizzorno. Can we say "cure"? *Integrative Medicine*, 15(5):8–12, 2016.

I. Polycarpou, K. Thielemans, R. Manjeshwar, P. Aguiar, P. K. Marsden, and C. Tsoumpas. Comparative evaluation of scatter correction in 3D PET using different scatter-level approximations. *Annals of Nuclear Medicine*, 25(9):643–649, 2011.

J. Ptacek, L. Henzlova, and P. Koranda. Bone SPECT image reconstruction using deconvolution and wavelet transformation: Development, performance assessment and comparison in phantom and patient study with standard OSEM and resolution recovery algorithm. *Physica Medica*, 30(7):858–864, 2014.

T. Puri, T. A. Greenhalgh, J. M. Wilson, J. Franklin, L. M. Wang, V. Strauss, C. Cunningham, M. Partridge, and T. Maughan. [18F]Fluoromisonidazole PET in rectal cancer. *European Journal of Nuclear Medicine and Molecular Imaging Research*, 7(1):78, 2017.

H. H. Quick. Integrated PET/MR. *Journal of Magnetic Resonance Imaging*, 39 (2):243–258, 2014.

A. Rahmim and H. Zaidi. PET versus SPECT: strengths, limitations and challenges. *Nuclear Medicine Communications*, 29(3):193–207, 2008.

A. Rahmim, J. Qi, and V. Sossi. Resolution modeling in PET imaging: Theory, practice, benefits, and pitfalls. *Medical Physics*, 40(6):064301, 2013.

A. Rahmim, M. A. Lodge, N. A. Karakatsanis, V. Y. Panin, Y. Zhou, A. B. McMillan, S. Y. Cho, H. Zaidi, M. E. Casey, and R. L. Wahl. Dynamic whole-body PET imaging: principles, potentials and applications. *European Journal of Nuclear Medicine and Molecular Imaging*, 46(S1):501–518, 2018.

E. Rapisarda, V. Bettinardi, K. Thielemans, and M. C. Gilardi. Image-based point spread function implementation in a fully 3D OSEM reconstruction algorithm for PET. *Physics in Medicine and Biology*, 55(14):4131–51, 2010.

I. Rauscher, T. Maurer, W. P. Fendler, W. H. Sommer, M. Schwaiger, and M. Eiber. 68Ga-PSMA ligand PET/CT in patients with prostate cancer: How we review and report. *Cancer Imaging*, 16(1):14, 2016.

C. Reeps, M. Essler, J. Pelisek, S. Seidl, H-H. Eckstein, and B-J. Krause. Increased 18F-fluorodeoxyglucose uptake in abdominal aortic aneurysms in positron emission/computed tomography is associated with inflammation, aortic wall instability, and acute symptoms. *Journal of Vascular Surgery*, 48(2): 417–423, 2008.

J. M. Rogasch, F. Hofheinz, A. Lougovski, C. Furth, J. Ruf, O. S. Großer, K. Mohnike, P. Hass, M. Walke, H. Amthauer, and I. G. Steffen. The influence of different signal-to-background ratios on spatial resolution and F18-FDG-PET quantification using point spread function and time-of-flight re-

construction. *European Journal of Nuclear Medicine and Molecular Imaging Physics*, 1(1):12, 2014.

O. Rousset, A. Rahmim, A. Alavi, and H. Zaidi. Partial volume correction strategies in PET. *PET Clinics*, 2(2):235–249, 2007.

N. Sakalihasan, R. Limet, and O. D. Defawe. Abdominal aortic aneurysm. *Lancet*, 365(9470):1577–1589, 2005.

W. Schneider, T. Bortfeld, and W. Schlegel. Correlation between CT numbers and tissue parameters needed for Monte Carlo simulations of clinical dose distributions. *Physics in Medicine and Biology*, 45(2):459–478, 2000.

W. Segars, G. Sturgeon, S. Mendonca, J. Grimes, and B. Tsui. 4D XCAT phantom for multimodality imaging research. *Medical Physics*, 37(9):4902–4915, 2010.

L. K. Shankar, S. Bacharach J. M. Hoffman, M. M. Graham, J. Karp, A. A. Lammertsma, S. Larson, D. A. Mankoff, B. A. Siegel, A. Van den Abbeele, J. Yap, and D. Sullivan; National Cancer Institute. Consensus recommendations for the use of 18F-FDG PET as an indicator of therapeutic response in patients in national cancer institute trials. *Journal of Nuclear Medicine*, 47 (6):1059–1066, 2006.

L. Shepp and Y. Vardi. Maximum likehood reconstruction for emission tomography. *IEEE Transactions on Medical Imaging*, MI-1:113–122, 1982.

Q.-W Shi, Ligeng Li, Changhong Huo, Manli Zhang, and Y.-F Wang. Study on natural medicinal chemistry and new drug development. *Chinese Traditional and Herbal Drugs*, 41(10):1583–1589, 2010.

R. L. Siddon. Fast calculation of the exact radiological path for a three-dimensional CT array. *Medical Physics*, 12:252–255, 1985.

J. Silva-Rodriguez, C. Tsoumpas, I. Dominguez-Prado, J. Pardo-Montero, A. Ruibal, and P. Aguiar. Impact and correction of the bladder uptake on 18F-FCH PET quantification: a simulation study using the XCAT2 phantom. *Physics in Medicine and Biology*, 61(2):758–773, 2016.

A. R. Singh. Modern medicine: Towards prevention, cure, well-being and longevity. *Mens Sana Monographs*, 8(1):17–29, 2010.

M. Soret, S. L. Bacharach, and I. Buvat. Partial-volume effect in PET tumor imaging. *Journal of Nuclear Medicine*, 48(6):932–945, 2007.

P. Sprawls. *Magnetic Resonance Imaging: Principles, Methods, and Techniques*. Medical Physics Publishing Corporation, 2000.

C. W. Stearns and A. Lonn. Randoms from singles estimation for long PET scans. In *2011 IEEE Nuclear Science Symposium Conference Record*, pages 3739–3741, 2011.

Ch. Steiner, H. Vees, H. Zaidi, M. Wissmeyer, O. Berrebi, M. P. Kossovsky, H. G. Khan, R. Miralbell, O. Ratib, and F. Buchegger. Three-phase 18F-fluorocholine PET/CT in the evaluation of prostate cancer recurrence. *Nuklearmedizin*, 48(1):1–9, 2009.

S. A. Suttie, A. E. Welch, and K. G. Park. Positron emission tomography for monitoring response to neo-adjuvant therapy in patients with oesophageal and gastro-oesophageal junction carcinoma. *European Journal of Surgical Oncology*, 35(10):1019–1029, 2009.

Y. Tani, M. Nakajima, M. Kikuchi, K. Ihara, H. Muroi, M. Takahashi, Y. Domeki, K. Okamoto, S. Yamaguchi, K. Sasaki, T. Tsuchioka, S. Sakamoto, and H. Kato. F-18-fluorodeoxyglucose positron emission tomography for evaluating the response to neoadjuvant chemotherapy in advanced esophageal cancer. *Anticancer Research*, 36(1):367–373, 2016.

B. K. Teo, Y. Seo Y, S. L. Bacharach, J. A. Carrasquillo, S. K. Libutti, H. Shukla, B. Hasegawa, R. Hawkins, and B. Franc. Partial volume correction in PET: Validation of an iterative postreconstruction method with phantom and patient data. *Journal of Nuclear Medicine*, 48:802–810, 2007.

K. Thielemans, R. M. Manjeshwar, C. Tsoumpas, and F. P. Jansen. A new algorithm for scaling of PET scatter estimates using all coincidence events. In *IEEE Nuclear Science Symposium and Medical Imaging Conference Record*, volume 5, pages 3586–3590, 2007.

K. Thielemans, E. Asma, S. Ahn, R. M. Manjeshwar, T. Deller, S. G. Ross, C. W. Stearns, and A. Ganin. Impact of PSF modelling on the convergence rate and edge behaviour of EM images in PET. In *IEEE Nuclear Science Symposium Medical Imaging Conference*, pages 3267–3272, 2010.

K. Thielemans, C. Tsoumpas, S. Mustafovic, T. Beisel, P. Aguiar, N. Dikaios, and M. W. Jacobson. STIR: Software for tomographic image reconstruction release 2. *Physics in Medicine and Biology*, 57(4):867–883, 2012.

B. A. Thomas, V. Cuplov, A. Bousse, A. Mendes, K. Thielemans, B. F. Hutton, and K. Erlandsson. PETPVC: A toolbox for performing partial volume cor-

rection techniques in positron emission tomography. *Physics in Medicine and Biology*, 61(22):7975–7993, 2016.

D. W. Townsend. Multimodality imaging of structure and function. *Physics in Medicine and Biology*, 53(4):R1–R39, 2008.

M. Truijers, H. A. J. M. Kurvers, S. J. H. Bredie, W. J. G. Oyen, and J. D. Blankensteijn. In vivo imaging of abdominal aortic aneurysms: Increased FDG uptake suggests inflammation in the aneurysm wall. *Journal of Endovascular Therapy*, 15(4):462–467, 2008.

C. Tsoumpas and K. Thielemans. Direct parametric reconstruction from dynamic projection data in emission tomography including prior estimation of the blood volume component. *Nuclear Medicine Commununication*, 30(7):490–493, 2009.

C. Tsoumpas, P. Aguiar, K.S. Nikita, D. Ros, and K. Thielemans. Evaluation of the single scatter simulation algorithm implemented in the STIR library. In *IEEE Nuclear Science Symposium and Medical Imaging Conference Record*, volume 6, pages 3361–3365, 2004.

National Research Council (US) and Institute of Medicine (US) Committee on State of the Science of Nuclear Medicine. Advancing nuclear medicine through innovation. `https://www.ncbi.nlm.nih.gov/books/NBK11475/`, 2007. Accessed: 2019-09-13.

S. Vaidyanathan, C. N. Patel, A. F. Scarsbrook, and F. U. Chowdhury. FDG PET/CT in infection and inflammation–current and emerging clinical applications. *Clinical Radiology*, 70(7):787–800, 2015.

S. R. Vallabhaneni, G. L. Gilling-Smith, T. V. How, S. D. Carter, J. A. Brennan, and P. L. Harris. Heterogeneity of tensile strength and matrix metalloproteinase activity in the wall of abdominal aortic aneurysms. *Journal of Endovascular Therapy*, 11(4):494–502, 2004.

S. Vandenberghe, E. Mikhaylova, E. D'Hoe, P. Mollet, and J. Karp. Recent developments in time-of-flight PET. *European Journal of Nuclear Medicine and Molecular Imaging Physics*, 3(1):3, 2016.

J. J. Vaquero and P. Kinahan. Positron emission tomography: Current challenges and opportunities for technological advances in clinical and preclinical imaging systems. *Annual Review of Biomedical Engineering*, 17:385–414, 2015.

T. O. Videen, J. S. Permutter, M. A. Mintun, and M. E. Raichle. Regional correction of positron emission tomography data for the effects of cerebral atrophy. *Journal of Cerebral Blood Flow & Metabolism*, 8:662–670, 1988.

K. Vunckx, A. Atre, K. Baete, A. Reilhac, C. M. Deroose, K. Van Laere, and J. Nuyts. Evaluation of three MRI-based anatomical priors for quantitative PET brain imaging. *IEEE Transactions on Medical Imaging*, 31(3):599–612, 2012.

L. Wang, S. Suo, J. Li, Y. Hu, P. Li, Y. Wang, and H. Hu. An investigation into traditional chinese medicine hospitals in china: Development trend and medical service innovation. *International Journal of Health Policy and Management*, 6(1):19–25, 2016.

C. C. Watson, D. Newport, and M. E. Casey. A single scatter simulation technique for scatter correction in 3D PET. In *Three-Dimensional Image Re-*

construction in Radiology and Nuclear Medicine Computational Imaging and Vision, volume 4, pages 255–268. Springer, Dordrecht, 1996.

W. A. Weber. Chaperoning drug development with PET. *Journal of Nuclear Medicine*, 47:735–737, 2006.

D. Weishaupt, V. D. Kochli, and B. Marince. *How does MRI Work?: An Introduction to the Physics and Function of Magnetic Resonance Imaging*. Springer, Science Business Media, Berlin, 2008.

A. E. Welch and S. Pimlott. *PET and SPECT in Drug Development*, pages 737–748. American Cancer Society, 2010.

M. Westerterp, J. Pruim, W. Oyen, O. Hoekstra, A. Paans, E. Visser, G. Sloof J. Van Lanschot, and R. Boellaard. Quantification of FDG PET studies using standardised uptake values in multi-centre trials: Effects of image reconstruction, resolution and ROI definition parameters. *European Journal of Nuclear Medicine and Molecular Imaging*, 34(3):392–404, 2007.

T. Witney, I. Alam, and D. Turton. Evaluation of deuterated 18F- and 11C-labeled choline analogs for cancer detection by positron emission tomography. *Clinical Cancer Research*, 18(4):1063–1072, 2012.

B. Yang, L. Ying, and J. Tang. Artificial neural network enhanced bayesian PET image reconstruction. *IEEE Transactions on Medical Imaging*, 37(6): 1297–1309, 2018.

H. Yuan, Q. Ma, L. Ye, and G. Piao. The traditional medicine and modern medicine from natural products. *Molecules*, 21(5):559, 2016.

H. Zaidi, N. Ojha, M. Morich, J. Griesmer, Z. Hu, P. Maniawski, O. Ratib, D. Izquierdo-Garcia, Z. A. Fayad, and L. Shao. Design and performance evaluation of a whole-body ingenuity TF PET-MRI system. *Physics in Medicine and Biology*, 56(10):3091–3106, 2011.

S. Ziegler, H. Braun, P. Ritt, C. Hocke, T. Kuwert, and H. H. Quick. Systematic evaluation of phantom fluids for simultaneous PET/MR hybrid imaging. *Journal of Nuclear Medicine*, 54(8):1464–1471, 2013.

S. Ziegler, B. W. Jakoby, H. Braun, D. H. Paulus, and H. H. Quick. NEMA image quality phantom measurements and attenuation correction in integrated PET/MR hybrid imaging. *European Journal of Nuclear Medicine and Molecular Imaging Physics*, 2:18, 2015.